Pontifícia Universidade Católica
do Rio de Janeiro

Igor José Califrer

Low intensity light meets feedback cooled levitated nanoparticles

Dissertação de Mestrado

Dissertation presented to the Programa de Pós–Graduação em Física of PUC-Rio in partial fulfillment of the requirements for the degree of Mestre em Física.

Advisor: Prof. Dr. Thiago Barbosa dos Santos Guerreiro

Rio de Janeiro
October 2024

Pontifícia Universidade Católica
do Rio de Janeiro

Igor José Califrer

Low intensity light meets feedback cooled levitated nanoparticles

Dissertation presented to the Programa de Pós–Graduação em Física of PUC-Rio in partial fulfillment of the requirements for the degree of Mestre em Física. Approved by the Examination Committee:

Prof. Dr. Thiago Barbosa dos Santos Guerreiro
Advisor
Departamento de Física – PUC-Rio

Prof. Dr. Joanna Ada Zielińska
ITESM

Prof. Dr. Paulo Américo Maia Neto
UFRJ

Rio de Janeiro, October 3rd, 2024

Igor José Califrer

The author graduated in Physics and in Materials Engineering and Nanotechnology from PUC-Rio in 2022.

Bibliographic data

Califrer, Igor José

Low intensity light meets feedback cooled levitated nanoparticles / Igor José Califrer; advisor: Dr. Thiago Barbosa dos Santos Guerreiro. – Rio de Janeiro: PUC-Rio, Departamento de Física, 2024.

v., 99 f: il. color. ; 30 cm

Dissertação (mestrado) - Pontifícia Universidade Católica do Rio de Janeiro, Departamento de Física.

Inclui bibliografia

1. Física – Teses. 2. Física – Teses. 3. optomecânica;. 4. pinça óptica;. 5. teoria de controle;. 6. resfriamento por retroalimentação;. 7. simulações numéricas;. 8. método de Euler-Maruyama.. I. Guerreiro, Thiago Barbosa dos Santos. II. Pontifícia Universidade Católica do Rio de Janeiro. Departamento de Física. III. Título.

CDD: 530

Acknowledgments

To me, life is a sequence of opportunities offered to us, some of which we choose to grasp and others which we do not, influenced at each and every moment by our hopes, fears, aspirations and all things of the sort. I would not set myself on to enumerate everyone who has aided, counseled and influenced me to trail the path I've followed. With this having been said, I would like to generically (but wholeheartedly) thank my family and fellow friends, without whom I would've been unable to grasp the specific opportunities which compose who I am today. I hope that I have been deserving of your care and support, and that you know I am grateful despite the conciseness of this Acknowledgements section.

With respect to this dissertation, I am thankful for having been bestowed with the opportunity to take part on the huge project which this work is but a small portion of.

This study was financed in part by the Coordenação de Aperfeiçoamento de Pessoal de Nível Superior - Brasil (CAPES) - Finance Code 001, by Fundação Carlos Chagas Filho de Amparo à Pesquisa do Estado do Rio de Janeiro (FAPERJ), by Fundação de Amparo à Pesquisa do Estado de São Paulo (FAPESP), by Conselho Nacional de Desenvolvimento Científico e Tecnológico (CNPq) and by Instituto Serrapilheira.

Abstract

Califrer, Igor José; Guerreiro, Thiago Barbosa dos Santos (Advisor). **Low intensity light meets feedback cooled levitated nanoparticles**. Rio de Janeiro, 2024. 99p. Dissertação de Mestrado – Departamento de Física, Pontifícia Universidade Católica do Rio de Janeiro.

Cooling is the necessary first step for any optomechanical experiment aiming to unleash the full potential of optical tweezers, both in the context of improving force sensitivity in sensor applications and of studying fundamental quantum physics at the microscale. The purpose of the work described in this dissertation was to improve an optical tweezer setup for electrical feedback cooling of the translational motion of levitated nanoparticles. We implement collection of backscattered light from the particle for improved detection efficiency of motion along the optical axis. Using a numerical simulation environment in Python, we also explore the potential of optomechanical systems as sensors for light states with very low intensities.

Keywords

optomechanics; optical tweezer; control theory; feedback cooling; numerical simulations; Euler-Maruyama method.

Resumo

Califrer, Igor José; Guerreiro, Thiago Barbosa dos Santos. **Luz de baixa intensidade encontra nanopartículas resfriadas**. Rio de Janeiro, 2024. 99p. Dissertação de Mestrado – Departamento de Física, Pontifícia Universidade Católica do Rio de Janeiro.

Resfriamento é o passo inicial necessário a qualquer experimento optomecânico que tenha como objetivo desbloquear o potencial das pinças ópticas, tanto para a melhoria da sensiblidade a forças em aplicações de sensoreamento quanto para estudos de física quântica fundamental na microescala. O propósito do trabalho descrito nesta dissertação foi o de melhorar a montagem de uma pinça óptica para resfriamento por retroalimentação do movimento translacional de nanopartículas levitadas. Nós implementamos a coleta de luz retroespalhada pela partícula para melhorar a eficiência de detecção do movimento ao longo do eixo óptico. Usando um ambiente de simulação numérica em Python, nós também exploramos o potencial de sistemas optomecânicos como sensores para estados de luz com intensidades muito baixas.

Palavras-chave

optomecânica; pinça óptica; teoria de controle; resfriamento por retroalimentação; simulações numéricas; método de Euler-Maruyama.

Table of contents

List of figures

List of tables

List of Abbreviations

BPD – Balanced Photodetector

CoM - Center of Mass

CW – Continuous Wave

DAC – Digital-to-analog converter

DC – Direct Current

FPGA – Field-Programmable Gate Array

FSR – Free Spectral Range

LQG – Linear Quadratic Gaussian

LQR – Linear Quadratic Regulator

LO – Local Oscillator

NA – Numerical Aperture

NP – Nanoparticle

PBS – Polarizing Beamsplitter

PC – Polarization Controller

PCB – Printed Circuit Board

PID – Proportional-Integral-Derivative

PSD – Power Spectral Density

QPD – Quadrant Photodetector

RF – Radio Frequency

RMS – Root Mean Square

SNR – Signal-to-Noise Ratio

SNSPD – Superconducting Nanowire Single Photon Detectors

SPAD – Single Photon Avalanche Diode

1
Introduction

Optical tweezers are a versatile platform for studies both in experimental and in theoretical sciences. Applications have been proposed in research fields ranging from biology [1–5] and thermodynamics [6–10] to metrology [11–21] and fundamental physics [22–28]. In part, this versatility may be justified by the simplicity of the fundamental model implemented in many optomechanical experiments - that of a harmonic oscillator. In this dissertation, we opt to omit a thorough theoretical detailing of the physical models describing the mechanisms which underlie optical trapping. Such descriptions have been provided in several other dissertations from our group, we refer the reader to the extensive material in [29–33].

The research hereby reported is composed by two main endeavors, one relying on theory and on computational methods, and another which is experimental. The common point between these two research lines is that both revolve around center of mass (CoM) translational cooling of levitated nanoparticles, either as a prerequisite or as a main objective. On the theoretical side, the central idea is to investigate whether small forces associated with the optomechanical interaction between feeble amounts of light and levitated nanoparticles (NPs) can be detected. Our experiments, on the other hand, aimed to cool the CoM motion of levitated nanoparticles with the perspective of preparing our experimental setup for bearing ground state cooled oscillators. Let us dive a bit into an overview of what results are reported in this dissertation, while also discussing why these goals are relevant in a general sense and, specifically on the experimental side, why it is important for us to be able to reach the motional ground state in our optical tweezer setup.

The manipulation of single photons is crucial for many quantum communication applications, as well as for quantum cryptography protocols. Aside from quantum information, the necessity for such states has stimulated the development of single photon sources and detectors [34]. Applications require detectors with high detection efficiency, low dark count rates and low dead times [35]. A number of single photon detector architectures has been proposed, but the two main ones are superconducting nanowire single photon detectors (SNSPDs) and single photon avalanche diodes (SPADs) [36], both of which

generally require cryogenic conditions for functional operation. In particular, the work in [37] reports the development of an SNSPD with detection efficiencies higher than 90% and photon detection rates higher than 150 MHz. In the context of levitated optomechanics, we propose an ambient temperature, optical tweezer-based detector of light states of very low intensity, which perhaps could serve as a prototypical system with potential for eventually breaking into the single photon regime. A numerical simulation environment has been developed in Python, with the purpose of quantitatively analyzing whether optomechanical systems can be used to sense very feeble optical impulses. A linearized optomechanical coherent scattering interaction is considered between a mechanical mode of a tweezed oscillator and a cavity mode, and we take advantage of the gaussianity of the system to describe its evolution only via first and second cumulants of the quantum state of the system. We carry out a Kalman filter implementation for optimal estimation of the system's state based on a complete description of its dynamics and on the outcomes of noisy measurements taken at a predefined sampling rate. The information provided by the Kalman filter is used to cool the oscillator using an optimal control protocol, the linear quadratic regulator (LQR), which in conjuction with the Kalman filter composes the linear quadratic gaussian (LQG) controller - see, for instance, [38]. Then, a coherent state with known phase and amplitude is introduced as an optical input, and we study whether state estimation of the system can be used to infer about the presence of this optical input.

Ground state preparation is a starting point for quantum experiments and for unlocking the full potential of optical tweezers in the context of sensing applications. To bring the motion of the levitated oscillator from a thermal state at room temperature down to the ground state, a few schemes have been proposed. Cavity-assisted "passive" strategies can be designed. Such techniques rely on favoring anti-Stokes scattering processes, such that removal of energy from the mechanical mode takes place naturally due to the optomechanical interaction [39–41]. "Active" schemes are also possible – in this case, a feedback signal is generated from a continuous measurement of the oscillator's state. This signal is transduced into force by some kind of actuator system which implements the control. There is a number of possible pathways for active feedback schemes, including parametric control, cold damping schemes and the LQR. In parametric control, the trap stiffness is modulated at twice the oscillator's natural frequency with an appropriate phase shift such that energy is removed from its motion. In cold damping experiments, one implements a control law proportional to the oscillator's velocity at each time, such that an artificial increase of the damping rate is generated. Another option is to use

optimal control schemes, such as the LQR for gaussian systems, for defining an appropriate control law. For more information, we refer the reader to the works in [42–48]. Furthermore, feedback actuation can be either optical or electrical [49, 50]. Electrical actuation avoids the potential complications entailed by optical feedback with regards to the alignment and implementation of the optical elements involved. On the other hand, it naturally introduces the difficulty of adapting the tweezer for the assembly of electrodes in a system which is required to be functional in low pressure conditions.

In general terms, measurement of the position of an optically trapped nanoparticle can be performed using either the forward-scattered or the backscattered light from the particle, which acts as a dipolar scatterer [51]. The idea is that the phase of the scattered fields carry information regarding the displacement of the scattered from the optical focus [52, 53]. Interference between the signal beam, which carries the position information, and a phase reference beam – often termed the local oscillator (LO) – yields an intensity profile which can be transformed into an electrical signal using a photodiode and readout by an oscilloscope. Now, it is worth noticing that the interference between signal and phase reference beams is asymmetric in the forward and backward directions due to the Gouy phase shift, see [52]. This asymmetry leads to a detection efficiency which is potentially much higher in the backward direction.

The experiments described in this work were performed in multiple steps. First, we learned how to apply an electrical feedback control to an optically levitated oscillator by subjecting it to a feedback-induced non-harmonic potential, and measuring its response as a function of the feedback control intensity. Having performed this experiment, we moved on to the implementation of electrical feedback cooling using forward scattered light to obtain information about the motion of the tweezed nanoparticle along the three orthogonal directions. Using an electrically actuated LQR controller, this information was used to achieve cooling of the transversal degrees of freedom down to about 0.5 K, and of motion along the longitudinal axis down to 3.6 K. In the last step of our experiment, we have taken the experimental setup and upgraded it. Through many modifications which are to be properly detailed in appropriate sections of the text, we have managed to implement detection of longitudinal motion of the particle using backward scattered light. The implementation of this detection scheme is very relevant to our experiments, because the higher detection efficiencies associated with it potentially allows us to achieve quantum limited detection, see [54], which is a primary requirement for investigating quantum behaviors of nano- to microscale objects.

This dissertation is organized as follows. Chapter 2 reports our first implementations of an electrical feedback system in an optical tweezer setup at medium vacuum (up to $\sim 10^{-2}$ mbar) [55]. Our purpose was to generate a nonlinear perturbation to the force experienced by the tweezed nanoparticle (NP) and measure its dynamics in such a controllably nonharmonic potential, thereby validating path integral methods previously developed by our group in [56]. These results represent the first contact of our group with electrical feedback systems, and the know-how stemming from their development was advantageous for the works which have followed.

We begin Chapter 3 by reporting another of our experimental works [55], where an all electrical feedback cooling system for our vacuum tweezer (working at pressures down to $\sim 10^{-5}$ mbar). As previously mentioned, we have been able to cool the center of mass (CoM) motion of silica NPs in three dimensions, down to ~ 0.5 K for the transversal directions and to ~ 3.6 K for motion along the longitudinal axis. This work and the expertise we developed while putting it forth were cornerstones for the remaining experimental results presented in this dissertation.

In the second part of Chapter 3, we go on to describe how the setup was improved and adapted for compatibility with a backward detection scheme for measuring motion along the optical axis. We comment on the experimental details regarding the assembly of this detection scheme and present further cooling results in the longitudinal direction, enhanced by the backward detection method and by the other upgrades we've implemented upon the experimental setup.

Chapter 4 describes the numerical simulation developed in Python with the purpose of analyzing whether an optically levitated feedback cooled system can be used to detect very feeble optical impulses, in an effective attempt at proposing an optomechanical detector for few or for single photons. Our discussion is oriented towards characterization of this metaphorical detector and optimization of the system's parameters for detection of the lowest possible optical input amplitudes.

We wrap up the dissertation by discussing possible pathways to follow and improvements to be made in the near future in Chapter 5.

2
Perturbative nonlinear feedback forces for optical levitation experiments

This chapter describes the experimental verification of the perturbative path integral theory used to describe the dynamics of optically tweezed NPs in nonlinear potentials, which was developed in [56]. The implementation of the nonlinear perturbation was carried out using electrical feedback, and we have validated the theory by matching the predicted particle frequency shift due to the presence of the perturbation with the observed one. This chapter reports the results presented in [55].

2.1
Introduction

Optical levitation of NPs provides a robust setup for both fundamental and applied physics [57,58], from classical stochastic thermodynamics [6,59–61] to mesoscopic quantum science [9,62,63]. In the typical levitated optomechanics experiment, a dielectric particle is trapped in a tightly focused Gaussian beam providing, to leading order approximation, a confining harmonic potential [64,65]. The particle undergoes Brownian motion due to interaction with its surrounding medium and measurements of its position correlation functions, notably the auto-correlation and the associated power spectrum, allows for the characterization of the trap's parameters [65,66].

While the harmonic approximation is commonly employed in optical trapping, the ability to engineer potential landscapes beyond the quadratic approximation is central to optomechanics. Nonlinear force landscapes are a valuable resource to nonequilibrium Brownian machines [67,68], the preparation of non-classical and non-Gaussian quantum states [69] and matter wave interference experiments [70], to mention just a few examples. Nonlinear potential landscapes also appear in structured light optical tweezers [71], as in double-well landscapes [8,72–74], structured light beams with pattern revivals [75], cylindrical vector beams [76] and dark focus traps [77,78].

In these nonlinear potential landscapes, to which we refer here as *nonlinear optical tweezers*, quantitative statistical description of the stochastic particle motion is significantly more complicated as it involves nonlinear

stochastic differential equations. To make quantitative predictions regarding the statistical correlators of the trapped particle's motion we can, however, resort to perturbation theory [79].

A perturbative method for nonlinear optical tweezers has been developed in [56], wherein it is possible to compute corrections to the statistical moments of particle motion, in particular the position power spectrum. The purpose of the present work is to experimentally validate these methods. In standard Gaussian optical tweezers, the ratio between linear and nonlinear spring constants cannot be varied independently, given that both scale linearly with the trapping power [80, 81]. Thus, we turn to effective feedback potential landscapes to implement nonlinear position-dependent forces upon a levitated nanosphere. We implement the nonlinearity via electric feedback and characterize its effects on the particle motion.

This paper is organized as follows. In the next section, we briefly review the perturbation theory for computing corrections to the correlation functions of a trapped particle under the influence of a nonlinear force, and generalize it to include the effect of delayed forces. Since we deal with artificial electric feedback potentials relying on measurements and processing of the trapped particle's position, they imply an inherent delay to the nonlinear force and therefore accounting for the effects of this delay is essential to validating the methods of [56]. We then describe the experimental setup used to generate nonlinear potential landscapes through electric feedback on the particle and numerically compute the effects of delay, showing that within the range of parameters employed in our experiment they are negligible. We implement a cubic force (quartic potential) on the particle and finally verify the perturbation theory by comparing the predicted center frequency of the position power spectral density with experimental results. We conclude with a brief discussion on the applications of artificial nonlinear forces to levitated optomechanics experiments.

2.2 Theory

2.2.1 Formulation of the perturbation theory

We model the stochastic motion of a particle in a fluid at thermal equilibrium at temperature T_{eff} and under a force field $\mathbf{F}(\mathbf{r})$ using the Langevin equation,

$$\ddot{\mathbf{r}}(t) = -\gamma_m \dot{\mathbf{r}}(t) + \mathbf{F}(\mathbf{r}(t))/m + \sqrt{C}\eta(t), \tag{2-1}$$

where m is the particle's mass, $\gamma_m = \gamma/m$, $C = 2\gamma k_B T_{\text{eff}}/m^2$ with γ the drag coefficient and $\eta(t)$ is isotropic Gaussian white noise, whose components satisfy

$$\mathbb{E}[\eta_i(t)\eta_j(t')] = \delta_{ij}\delta(t-t'). \tag{2-2}$$

Concentrating in the motion along the longitudinal z-direction, Eq. (2-1) reduces to a one dimensional Langevin equation

$$\ddot{z}(t) = -\gamma_m \dot{z}(t) + F_z(z(t))/m + \sqrt{C}\eta(t). \tag{2-3}$$

For an approximately linear trapping force perturbed by nonlinear corrections, the steady state position auto-correlation $A(t) \equiv \mathbb{E}[z(t)z(0)]$ can be perturbatively approximated. We next summarize the perturbation theory outlined in [56] and used throughout this work.

Consider the force acting on the particle,

$$F_z(z) = -m\omega_0^2 z - G_{fb}z^3, \tag{2-4}$$

where the first term accounts for an optical trap with resonance frequency ω_0 and the second term is a small nonlinear correction, which in the experiment originates from a feedback force on the particle proportional to the *feedback gain* G_{fb} times a nonlinear function of the particle's position. We define the Green's function

$$G(t) = \frac{\sin(\Omega\, t)}{\Omega}\ \exp\!\left(-\frac{\gamma_m t}{2}\right) H(t), \tag{2-5}$$

where $\Omega = \sqrt{\omega_0^2 - \gamma_m^2/4}$ and $H(t)$ is the Heaviside step function with $H(t) = 1$ for $t > 0$ and $H(t) = 0$ for $t \leq 0$. We introduce the auxiliary variable (also referred to as the response paths) $\tilde{z}(s)$ and define the Wick sum bracket $\langle(\cdots)\rangle_0$:

$$\langle z(t_1)\cdots z(t_n)\tilde{z}(s_1)\cdots\tilde{z}(s_m)\rangle_0 = \delta_{nm}\sum_{\sigma}\prod_{j=1}^{n} G(t_j - s_{\sigma(j)}) \tag{2-6}$$

where the sum goes over all permutations σ of indexes $\{1,\ldots,n\}$. The response variables $\tilde{z}(s)$ can be understood as auxiliary integration variables in a stochastic path integral defining the perturbation theory expansion; we refer to [56, 79] for details on stochastic perturbation methods. Note that the second order correlator is given by the Green function, $\langle z(t)\tilde{z}(s)\rangle_0 = G(t-s)$. The perturbation theory is summarized by the expression for the position auto-correlation function,

$$A(t) \equiv \mathbb{E}[z(t)z(0)] = \langle z(t)z(0)e^{\frac{C}{2}\int \tilde{z}^2(s)ds} e^{\frac{G_{fb}}{m}\int \tilde{z}^3(t')z(t')dt'} \rangle_0, \tag{2-7}$$

where the right-hand side is defined by expanding both exponentials inside the brackets as a power series in C and in G_{fb}/m and interchanging summations and integrations by applying the Wick bracket $\langle(\cdots)\rangle_0$. Note that only brackets with an equal number of z and $\tilde{z}$ variables are non-vanishing [56, 79].

The first non-vanishing term in the expansion of Eq. (2-7) is

$$\frac{C}{2}\int \langle z(t)z(0)\tilde{z}^2(s)\rangle_0 \, ds = C\int G(t-s)G(-s)ds \ , \tag{2-8}$$

which gives the auto-correlation for the case of a linear force $F_z(x) = -m\omega_0^2 z$,

$$A(t)_{(G_{fb}=0)} = \frac{Ce^{-\gamma_m|t|/2}(2\Omega\cos\Omega|t| + \gamma_m \sin\Omega|t|)}{\gamma_m\Omega(\gamma_m^2 + 4\Omega^2)}. \tag{2-9}$$

The leading order correction in the feedback gain reads,

$$\Delta A(t) \equiv \frac{C^2 G_{fb}}{8m}\int \langle \tilde{z}^2(s_1)\tilde{z}^2(s_2)\tilde{z}(t_1)z^3(t_1)z(t)z(0)\rangle_0 \, ds_1 ds_2 dt_1. \tag{2-10}$$

Expanding the brackets using (2-6) would produce a sum with $5! = 120$ terms, but many of these vanish since $\langle \tilde{z}(t_1)z(t_1)\rangle = G(0) = 0$. Moreover, by symmetry of the integration variables s_1 and s_2, the contribution to the integral of the non-vanishing terms is equal to the contribution of $G(t-t_1)G(-s_1)G(t_1-s_1)G^2(t_1-s_2)$ or $G(-t_1)G(t-s_1)G(t_1-s_1)G^2(t_1-s_2)$. Therefore, the integral in (2-10) is computed by integrating these two terms over t_1, s_1, s_2 and multiplying both integrals by a multiplicity factor $2^3(3!) = 48$. We note that a diagrammatic expansion can be employed to organize non-vanishing terms in the Wick sum; for more details we refer to [56].

From the auto-correlation function perturbation ΔA we can obtain the correction in the power spectral density (PSD) of the particle motion by taking the Fourier transform [56],

$$\Delta S = \frac{3G_{fb}C^2}{\gamma_m\omega_0^2}\frac{\omega^2 - \omega_0^2}{[\gamma_m^2\omega^2 + (\omega^2-\omega_0^2)^2]^2}. \tag{2-11}$$

The PSD of the motion of a particle with unperturbed resonance frequency ω_0 subject to a frequency shift $\Delta\Omega$ can be expanded to first order as:

$$\frac{C}{\gamma_m^2\omega^2 + [\omega^2 - (\omega_0+\Delta\Omega)^2]^2} \approx \frac{C}{\gamma_m^2\omega^2 + (\omega^2-\omega_0^2)^2} +$$

$$+ 4C\omega_0\Delta\Omega\frac{\omega^2-\omega_0^2}{[\gamma_m^2\omega^2+(\omega^2-\omega_0^2)^2]^2}, \quad (2\text{-}12)$$

Comparing the first order correction in Eq. (2-12) with the correction in Eq. (2-11), we conclude that the nonlinearity causes a frequency shift given by:

$$\frac{\Delta\Omega}{2\pi} = \frac{3k_bT_{\text{eff}}}{4\pi m^2\omega_0^3}G_{fb} \equiv \kappa G_{fb}. \quad (2\text{-}13)$$

We see that effectively, the nonlinear perturbation manifests as a shift in the PSD central frequency scaling linearly with the feedback gain G_{fb} and with a slope given by the constant κ. This is valid for small G_{fb},

$$G_{fb} \ll \frac{m^2\omega_0^4}{2k_bT_{\text{eff}}}. \quad (2\text{-}14)$$

The right-hand side of (2-14) can be used to delimit the validity region of perturbation theory. The shift $\Delta\Omega$ in the central frequency of the PSD is the experimental signature which we use as an indicator of the effect of nonlinear perturbations. It is worth noticing that the shift described by (2-13) also includes intrinsic nonlinearities of the tweezer, which arise due to anharmonicities of the trapping potential [80]. Note, however, that only relative shifts to the original resonance frequency (with the cubic feedback off but in presence of the intrinsic nonlinearities) are measured. Thus, our experiment is not sensitive to the intrinsic anharmonicities of the trap, but only to those effected by the cubic feedback.

2.2.2 Delayed nonlinearities

Besides nonlinear force perturbations, we will be interested in delayed forces. Artificially produced feedback forces will naturally be subject to electronic delay. Accounting for the effects of such delays in perturbation theory allows us to understand the limits of validity of Eq. (2-7) for modelling the artificial feedback forces. More broadly, understanding the role of delays might also enable the study of perturbative nonlinear non-Markovian stochastic dynamics [82].

We consider the generalized Langevin equation,

$$\ddot{z}(t) = -\gamma_m\dot{z}(t) - \omega_0^2 z(t) - \frac{G_{fb}}{m}\, z^3(t-\tau) + \sqrt{C}\,\eta(t), \quad (2\text{-}15)$$

where $\tau > 0$ is a fixed (constant) time delay. Note the delayed position can be

written in terms of a memory kernel,

$$z(t-\tau) = \int z(s)K(t-s)\,ds \tag{2-16}$$

where,

$$K(t-s) = \delta(t-\tau-s) \tag{2-17}$$

The perturbation expansion for $\tau = 0$ (Eq. (2-7)) can then be generalized to

$$A(t,\tau) \equiv \mathbb{E}[z(t)z(0)] = \langle z(t)z(0)e^{\frac{C}{2}\int \tilde{z}^2(s)ds} e^{\frac{G_{fb}}{m}\int \tilde{z}(t')z^3(t'-\tau)dt'}\rangle_0. \tag{2-18}$$

Expanding the exponentials in power series and using the Wick sum as defined in (2-6), the leading correction to the auto-correlation function (2-9) is given by the following integrals,

$$\begin{aligned}\Delta A(t,\tau) \propto & \int G(t-t_1)G(-s_1)G(t_1-s_1-\tau)G^2(t_1-s_2-\tau)dt_1ds_1ds_2 \\ & + \int G(-t_1)G(t-s_1)G(t_1-s_1-\tau)G^2(t_1-s_2-\tau)dt_1ds_1ds_2\ .\end{aligned} \tag{2-19}$$

We note both integrals are multiplied by the constant $3G_{fb}C^2/m$, which we omit to avoid cluttering the notation. Evaluating the integrals leads to the corrected auto-correlation function to first order in the perturbation,

$$\begin{aligned}A(t,\tau) = & \frac{Ce^{-\gamma_m|t|/2}(2\Omega\cos\Omega|t| + \gamma_m\sin\Omega|t|)}{\gamma_m\Omega(\gamma_m^2+4\Omega^2)} + \frac{3C^2G_{fb}e^{-\gamma_m|t|/2}}{64m\gamma_m^3\Omega^4\omega_0^6}\Bigg\{ \\ & e^{\gamma_m\tau/2}[8\gamma_m\Omega^4 - 4\omega_0^2\gamma_m^2\Omega^2(|t|-\tau)]\cos(\Omega(|t|-\tau)) \\ & + e^{\gamma_m\tau/2}[8\gamma_m\Omega^3\omega_0^2(|t|-\tau) + 8\Omega^5 + 4\gamma_m^2\omega_0^2\Omega + 6\gamma_m^2\Omega^3]\sin(\Omega(|t|-\tau)) \\ & + e^{-\gamma_m\tau/2}[\Omega^2(2\gamma_m^2\Omega - 8\Omega^3)\sin(\Omega(|t|+\tau)) \\ & + 8\gamma_m\Omega^4\cos(\Omega(|t|+\tau))]\Bigg\} + \mathcal{O}\Big(G_{fb}^2, C^3\Big),\end{aligned} \tag{2-20}$$

The quantity $A(0,\tau)$ can be experimentally obtained from the area under the PSD of the particle's motion, which in turn can be related to the mean occupation number of the mechanical modes. In what follows, we use these expressions to account for the effects of delay in the artificially generated nonlinear forces, and to show that perturbation theory in the absence of delay provides a good approximation to current experiments.

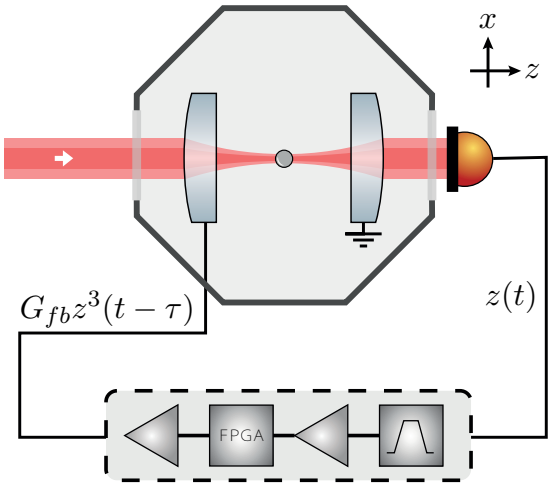

Figure 2.1: Experimental setup. A silica NP is trapped by an optical tweezer in vacuum. The forward scattered light is collected and sent to a photodiode, producing a signal proportional to the particle's axial coordinate, $z(t)$. An FPGA processes the signal to produce a voltage that induces a force on the trapped particle proportional to $z^3(t-\tau)$. Amplification prior to and after the FPGA enhance the maximum resolution of its analog-to-digital converter, enabling the exploration of a broader range of values for the applied electrical force. The x-direction pictured in the scheme is parallel to the optical table.

2.3 Experiment

A simplified schematic of the experimental setup is shown in Figure 2.1. A (continuous wave) laser at 780 nm (Toptica DL-Pro) is amplified using a tapered amplifier (Toptica BoosTa) producing up to 1.5 W at the output of a single mode fiber, yielding a high quality Gaussian beam. The beam is expanded to overfill an aspheric lens of numerical aperture (NA) = 0.77 (LightPath 355330) mounted inside a vacuum chamber, which provides a tightly focused Gaussian beam to form the optical trap. A solution of silica spheres of diameter $2R = 143$ nm (MicroParticles GmbH) is mono-dispersed in ethanol and delivered into the optical trap using a nebulizer. Once a single particle is trapped, the pressure in the chamber is reduced to 10 mbar. The trapped particle's axial center-of-mass (COM) motion, $z(t)$, is recorded by collecting forward scattered light with an aspheric lens of numerical aperture NA = 0.50, and directing it to a photodiode (Thorlabs PDA100A2), generating an electric signal proportional to $z(t)$.

The signal from the detector is sent to a wide band-pass filter, amplified and then input into an FPGA (field-programmable gate array). The FPGA

introduces a tunable delay, raises the signal to the third power and multiplies it by a tunable gain. The output signal is then amplified once again and applied to the mount of the trapping lens, producing a voltage difference with respect to the mount of the collection lens, which is grounded. This generates an electric force at the particle position given by $G_{fb}z^3(t-\tau)$, where τ is the total delay introduced by the electronics and G_{fb} is the overall feedback gain. For more details on the generated electric field and electronics, see Appendices A.1 and A.2.

The electronics naturally introduce a delay to the applied position-dependent electric forces, which could lead to deviations from the predictions of the perturbation theory discussed in Sec. 2.2.1. To qualitatively understand the effects of a delayed feedback nonlinear force, we have exaggerated the electronic delay τ applying a cubic force of the form $G_{fb}x^3(t-\tau)$ for $\tau = (2\pi/4\omega_0) = T/4$ and $\tau = 6\pi/4\omega_0 = 3T/4$, and subsequently measured the PSDs of the particle motion along the longitudinal direction. The results can be seen in Figure 2.2a), in comparison to the PSD of the trapped particle in the absence of nonlinear feedback. We see that depending on the delay, the particle undergoes cooling ($\tau = T/4$) or heating ($\tau = 3T/4$). This can be understood as the nonlinear analogue of cold damping, where the delayed feedback signal acquires a force component proportional to the velocity [45, 83, 84].

We can quantify the effect of delay for the case of our experiment using the theory described in Sec. 2.2.2. To do that, we have simulated the particle dynamics under the influence of a delayed feedback cubic force for two different values of the feedback gain G_{fb} within the regime of perturbation theory. For each simulation, we extract the particle motion traces and compute the position variance, from which the effective temperature T_{eff} of the mechanical oscillator can be obtained. The results are plotted in Figure 2.2b) as a function of τ, in comparison to the theoretical prediction given by Eq. (2-20). The simulations confirm the qualitative cooling/heating results shown in Figure 2.2 and are in good agreement to the perturbation theory with the inclusion of delay. Notably, for the electronic delay in our experiment, characterized to be $\tau = (0.518 \pm 0.074) \times 10^{-6}\,\text{s}$, we verify that the expected cooling/heating effects due to a delayed nonlinear feedback provide a correction to the auto-correlation at the level of 1.10% and are buried within experimental uncertainties. With this analysis we conclude that any effect associated to electronic delay in our experiment is negligible and the perturbation theory in the absence of delay can be used to model the effect of nonlinear perturbations.

We next proceed to verify the perturbation theory as described in Sec. 2.2.1 (without delay, $\tau = 0$). We apply an effective quartic perturbation to

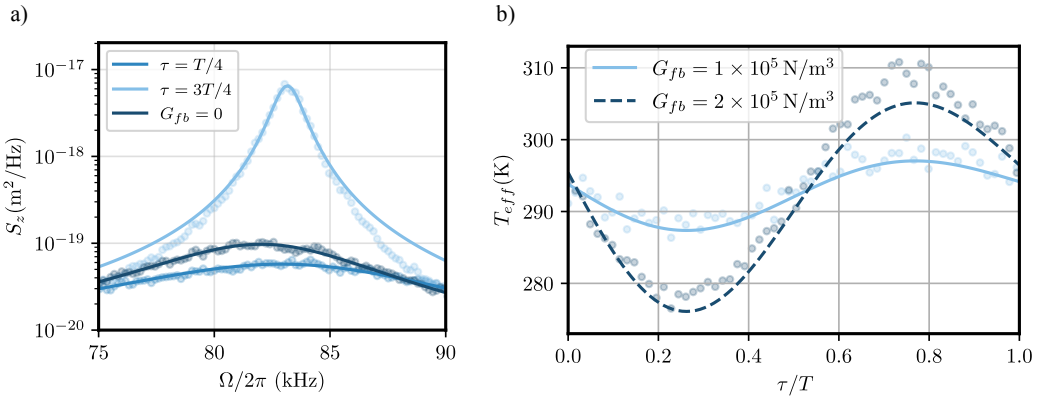

Figure 2.2: Effect of a delayed nonlinearity. a) Longitudinal position PSDs for the reference measurement (—) in comparison to cubic feedback forces at a gain of $G_{fb} = 5.31 \times 10^6\,\mathrm{N/m}^3$ and delays of $\tau = T/4$ (—) and $\tau = 3T/4$ (—). Here, T represents the period of the particle motion along the longitudinal direction. These comparisons reveal how the introduction of a delayed cubic force can either cool or heat the particle motion. b) Numerically simulated effective temperature T_{eff} of particle motion as a function of the delay in the cubic feedback force, displaying cooling and heating in accordance to the predictions of nonlinear delayed perturbation theory described in Sec. 2.2.2. With this analysis, we conclude that the electronic delay present in our experiment, measured to be $\tau/T = 0.042 \pm 0.006$, can be safely neglected.

the optical potential by acting on the trapped particle with a cubic force which was generated, as previously described, from the position measurement feedback. PSDs of particle motion under the influence of the cubic feedback force with positive and negative feedback gains can be seen in Figure 2.3a). These measurements qualitatively confirm the effect of the cubic force predicted by perturbation theory as a shift in the PSD central frequency. Note the shift depends on the sign of the feedback gain, in accordance to Eq. (2-13), indicating an effective hardening or softening of the optical trap due to the cubic actuation.

To quantitatively compare the frequency shifts with the predictions from perturbation theory, we acquired the longitudinal motion PSD for different values of feedback gain G_{fb}. Note that all parameters going into κ (see Eq. (2-13)) are obtained from additional setup characterizations, leaving no free parameters for adjusting the theory to the data. For instance, the trap central frequency ω_0 and mechanical damping γ_m are obtained from Lorentzian fits of the unperturbed PSD, the NP mass m is calculated from the diameter provided by the manufacturer and from the density of silica, and the applied feedback gain G_{fb} is obtained after the calibration of the detector, electrode and other intermediate electronic elements as described in more detail in Appendix A.2.

The particle is taken to be at ambient temperature $T_{\text{eff}} = 293\,\text{K}$; note that a 5 K variation in temperature yields a 2 % variation in theoretical prediction.

Once these characterizations have been performed, the central frequencies of the perturbed PSDs – and consequently the associated shifts – can be obtained by a Lorentzian fit as a function of feedback gain and compared to the theoretical predictions. The result of these measurements is shown in Figure 2.3b), in comparison to the theoretical prediction given in Eq. (2-13) for our experimental parameters.

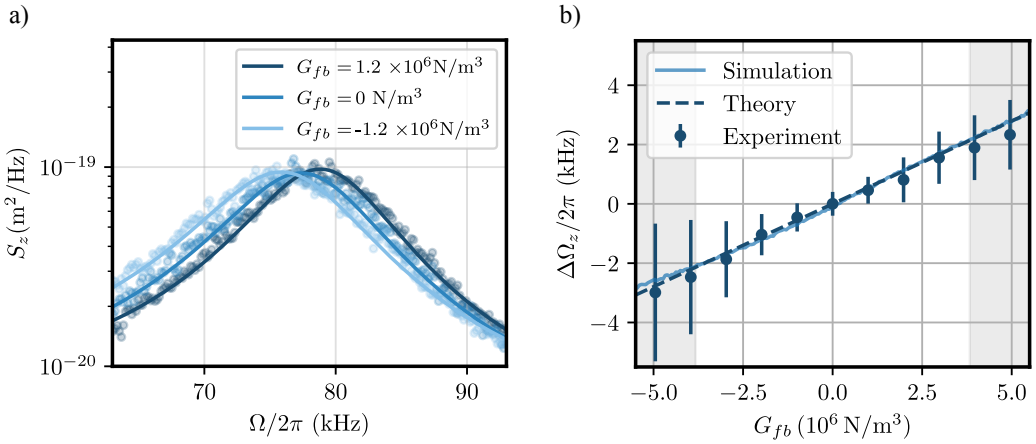

Figure 2.3: Verifying the predictions of perturbation theory: a) PSDs of the trapped particle's longitudinal motion under cubic force, displaying central frequency shifts. The data was taken at 293 K and a pressure of 10 mbar. The reference PSD (—) has a central frequency of 77.8 kHz and a shift of ±1.4 kHz was measured for $G_{fb} = \pm 1.2 \times 10^6\,\text{N/m}^3$. b) Frequency shifts as a function of G_{fb}, verifying the prediction of perturbation theory given by Eq. (2-13) (dashed line). The grey shaded region marks the regime of validity for perturbation theory described in Eq. (2-14). Each point corresponds to 250 seconds of data acquisition at 500 kHz divided into 1000 traces and organized into batches of 5 traces each. All data points were collected using the same NP.

Good agreement between the data and the theoretical prediction was observed within the perturbation regime, indicated by the non-shaded region of the plot. Note also that outside the regime of perturbation theory (grey shaded regions in Figure 2.3b)), the measured shifts fall systematically slightly bellow the predicted first order correction, consistent with the second-order correction scaling of $\mathcal{O}(G_{fb}^2)$ [56]. Note the error bars in Fig. 3b) are larger for negative feedback in comparison to positive feedback gains. We attribute this to the fact that the intrinsic nonlinearity of the optical trap introduces an effective negative feedback gain ($G_{\text{optical}} \approx 10^6\,\text{N/m}^3$), shifting the regime of validity of perturbation to the right, towards positive gains [80]. Finally, the

experimentally obtained angular coefficient κ_e was measured to be

$$\kappa_e = (5.46 \pm 0.10) \times 10^{-4}\,\mathrm{Hz\,m^3\,N^{-1}} \tag{2-21}$$

which compares to the theoretical prediction given the parameters for our experiment,

$$\kappa_t = 5.69 \times 10^{-4}\,\mathrm{Hz\,m^3\,N^{-1}}\ . \tag{2-22}$$

2.4 Conclusions

In conclusion, we have implemented a cubic nonlinear force based on position measurement feedback acting on an underdamped levitated NP. Effects of the cubic force on the particle's stochastic dynamics have been experimentally studied. In particular, shifts introduced in the particle motion power spectrum due to the presence of the cubic feedback force have been measured. We have verified that these shifts are in accordance to the predictions of the stochastic path integral perturbation theory for nonlinear optical tweezers introduced in [56]. To account for the experimental imperfections due to electronic delay in the feedback, we have also extended the perturbation theory and showed that for feedback schemes currently available in levitated optomechanics experiments the effects of electronic delay can be made negligible.

We anticipate that nonlinear electric feedback potentials will find a number of applications in levitated optomechanics experiments, both in the classical stochastic and quantum regimes. For instance, delayed nonlinear feedback can be used to engineer a non-conservative system with nonlinear damping of the Van der Pol type [85]. Finally, weak measurements of a levitated optomechanical system in a cavity might allow for feedback-induced nonlinear dynamics in the quantum regime [86] – the non-classical version of feedback-induced nonlinear forces. In combination with recent advances in levitated quantum control experiments [45,48], weak nonlinear feedback could then enable the preparation of non-Gaussian states beyond the nonlinearities naturally present in optical potentials [70,87].

3
Cooling

As mentioned in Chapter 1, given a position measurement of the optically levitated nanoparticle, one way to achieve cooling is to implement active feedback control of the levitated nanoparticle. Once we have mastered the implementation of electrical feedbacks in optical tweezers, as demonstrated in the previous chapter, we move on to cooling experiments. We shall first present the results previously obtained with our setup in the context of feedback cooling of optically levitated NPs as reported in [88]. Information about the particle's position was obtained by detecting forward-scattered light from the tweezer, and this is input to an LQR feedback control system which actuates upon the nanoparticle. Using this feedback cooling scheme, we have managed to achieve effective temperatures down to 0.5 K for the transversal mechanical modes and 3.6 K for the longitudinal one.

As previously argued, longitudinal detection efficiency is much higher in the backward than in the forward direction [51]. In the second part of this chapter, we detail how our experimental setup was modified with the final goal of implementing detection of longitudinal motion using backscattered light from the optical tweezer. The main modifications to the setup included entirely remodelling the mechanical mount of the optical tweezer, replacing the knife-edge detection in the forward direction by a quadrant photodetector (QPD), implementing a libration detector for proper distinction between differently shaped nanoparticles and stabilizing the interference between a phase reference and the collected beam using a fiber stretcher. We document and detail these changes in the following sections, and present the 1D cooling results obtained using information from the backward detection to electrically feedback control our levitated nanoparticle along the optical axis.

3.1
All electrical cooling of an optically levitated nanoparticle

3.1.1 Introduction

Optical tweezers [89] have emerged as a valuable tool for isolating and controlling the motion of micro- and nano-objects [57, 58, 65]. By clever combinations with electric and magnetic traps and actuators [28, 46, 90–92], optical traps can be used to design highly sensitive sensors for force, acceleration, and torque [16, 93–96], with a high degree of control enabling cooling of the center-of-mass motion of a levitated NP to the ground state [41, 45, 48, 97]. Moreover, tweezers provide a versatile platform for many-body [47, 98–101] and fundamental physics experiments, with applications in diverse areas such as stochastic thermodynamics [59, 102–105], nonlinear dynamics [8, 55, 80, 104, 106], the search for new particles and forces of nature [107–112], and unprecedented tests of quantum mechanics [70, 113–116]. All these applications require the levitated object to be well isolated from its surrounding environment, which is mainly limited by the vacuum quality of the experiment, photon recoil heating [117], and black body radiation [118]. Regarding the vacuum quality, since the nano-object is initially trapped at atmospheric pressure, it is thermalized at room temperature, preventing stable trapping at low pressures and rendering the trapping potential nonlinear due to large thermal fluctuations [80]. Therefore, cooling the object's motion is often a prerequisite for levitation experiments.

Active feedback cooling [83, 84], in particular parametric cooling, has emerged as the standard technique for achieving 3D cooling of the levitated NP's motion [119], enabling temperatures as low as sub-mK [117]. In practice, parametric control techniques are often used as a precooling mechanism. The performance of parametric feedback, however, comes at the cost of employing a nonlinear control protocol which modulates a portion of the optical trapping power according to the resonance frequencies of the NP. In addition, expensive electro- (EOM) or acousto-optic (AOM) modulators must be used in combination with lock-in devices capable of modulating a signal locked to the particle's motion. Alongside the parametric control, once the thermal occupation number has been reduced to around 10^3, the levitated object's charge can be exploited to further control its motion along one direction to even lower temperatures all the way into the quantum ground state [45, 48].

In this letter we explore an all electrical approach to pre-cool the motion of a levitated NP from room temperature to a point where the trap's nonlinear features are significantly reduced and stable trapping can be achieved in high-vacuum ($p < e{-}3\,\mathrm{mbar}$). To do so, we design a simple electric actuator based on a custom made printed circuit board (PCB), capable of influencing the particle's motion via Coulomb forces. Fine alignment of the PCB with the

levitated NP is not required. After a careful calibration of the electrical forces, we employ a delayed feedback scheme to 3D cool the CoM motion of the particle. We experimentally measure the effect of the delay in the feedback force and show excellent agreement with theoretical predictions [120]. Finally, we successfully demonstrate 3D cooling down to sub-Kelvin temperatures while completely avoiding modulation of the trap's power, in a first step towards the larger effort of simplifying optomechanical cooling experiments. With numerical simulations based on our electrical actuator we argue that, in combination with a stiffer optical trap, quantum-limited detection for all three axes [51] and optimal quantum state estimation [121–123], an all electrical optimal control approach can be employed to reach, in the three axes, a few phonons regime.

We highlight that 3D electrical feedback cooling of levitated NPs has been recently implemented in levitated optomechanics experiments – see [21,124,125] for examples using integrated chip photonics, hybrid optical Paul trap and finely aligned electrode tips. Our setup adds a simplified solution to that list, while still offering the possibility of 3D quantum control of a levitated NP. This paper is organized as follows. In Sec. 3.1.2 we briefly describe the equations of motion and the LQR, used to evaluate the optimal proportional and derivative gains used in the control feedback. Next, Sec. 3.1.3 describes the experimental setup, while 3.1.4 shows the results on all electrical feedback cooling and the prospects for 3D ground state cooling. We conclude in Sec. 3.1.5 with a brief discussion.

3.1.2 Theory

The CoM motion along the x, y and z-axes of an optically levitated NP trapped by a strongly focused Gaussian beam can be effectively modeled through a set of second-order Langevin equations,

$$\ddot{x}(t) + \gamma_m \dot{x}(t) + \Omega_x^2 x(t) = \frac{1}{m} F_{\mathrm{th},x}(t) + b_x u_x, \tag{3-1a}$$

$$\ddot{y}(t) + \gamma_m \dot{y}(t) + \Omega_y^2 y(t) = \frac{1}{m} F_{\mathrm{th},y}(t) + b_y u_y, \tag{3-1b}$$

$$\ddot{z}(t) + \gamma_m \dot{z}(t) + \Omega_z^2 z(t) = \frac{1}{m} F_{\mathrm{th},z}(t) + b_z u_z, \tag{3-1c}$$

where m is the particle's mass, γ_m the drag coefficient, Ω_i the angular frequency along the i-axis and $F_{\mathrm{th},i}$ represents the (white-noise) stochastic force on each axis due to residual gas pressure in the vacuum chamber, satisfying

$$\langle F_{\mathrm{th},i}(t) \rangle = 0, \tag{3-2a}$$

$$\langle F_{\mathrm{th},i}(t) F_{\mathrm{th},j}(t+\tau) \rangle = 2m\gamma_m k_B T \delta_{ij} \delta(\tau), \tag{3-2b}$$

where k_B is the Boltzmann constant, T the residual gas temperature, δ_{ij} is the Kronecker delta and $i, j \in \{x, y, z\}$. The $b_i u_i$ terms in Eqs. (3-1) account for external forces that may influence the particle's motion, with u_i representing the control signals defining feedback forces acting on the trapped particle.

By defining the state vector

$$\mathbf{x}(t) \equiv \begin{bmatrix} x(t) & y(t) & z(t) & \dot{x}(t) & \dot{y}(t) & \dot{z}(t) \end{bmatrix}^T, \tag{3-3}$$

one can then write Eqs. (3-1) in the state-variable representation [126], resulting in the Multiple-Input-Multiple-Output (MIMO) system

$$\dot{\mathbf{x}}(t) = \mathcal{A}\mathbf{x}(t) + \mathbf{B}\mathbf{u}(t) + \mathbf{w}(t), \tag{3-4}$$

where

$$\mathcal{A} = \begin{bmatrix} \mathbf{0}_{3\times3} & \mathbf{I}_3 \\ -\mathrm{diag}(\mathbf{\Omega}^2) & -\gamma_m \mathbf{I}_3 \end{bmatrix}, \ \mathbf{w}(t) = \frac{1}{m}\begin{bmatrix} \mathbf{0}_{3\times1} \\ \mathbf{F}_{\mathrm{th}}(t) \end{bmatrix}, \tag{3-5}$$

and

$$\mathbf{B} = \begin{bmatrix} \mathbf{0}_{3\times3} \\ \mathrm{diag}(b_x, b_y, b_z) \end{bmatrix}, \ \mathbf{u} = \begin{bmatrix} u_x \\ u_y \\ u_z \end{bmatrix}, \tag{3-6}$$

with $\mathbf{\Omega}^2 = \begin{bmatrix} \Omega_x^2 & \Omega_y^2 & \Omega_z^2 \end{bmatrix}^T$ and $\mathbf{F}_{\mathrm{th}}(t) = \begin{bmatrix} F_{\mathrm{th,x}}(t) & F_{\mathrm{th,y}}(t) & F_{\mathrm{th,z}}(t) \end{bmatrix}^T$. Note that due to the geometry of the feedback actuators in our experiment, the submatrix in $\mathbf{B}$ is not block diagonal, but assumes a more complicated form; see Sec. 3.1.3 for more details.

Optimal control theory provides tools to find a control policy $\mathbf{u}(t)$ capable of minimizing the energy of a physical system. For linear systems, such as the one described by Eq. (3-4), this is achieved by the LQR, a controller where the optimization task targets the minimization of a quadratic cost criterion J of the form

$$J = \frac{1}{2}\int_0^\infty \left[\mathbf{x}^T(t)\mathcal{Q}\mathbf{x}(t) + \mathbf{u}^T(t)\mathbf{R}\mathbf{u}(t)\right] dt, \tag{3-7}$$

where $\mathcal{Q}$ is the weighting matrix and $\mathbf{R}$ is the control effort matrix. The optimal control policy which minimizes Eq.(3-7) is [127]

$$\mathbf{u} = -\mathbf{K}\mathbf{x}, \tag{3-8}$$

where $\mathbf{K} = \mathbf{R}^{-1}\mathbf{B}\mathbf{S}$ is the controller's gain matrix and $\mathbf{S}$ is the solution of the algebraic Riccati equation

$$\mathbf{S}\mathcal{A} + \mathcal{A}^T\mathbf{S} + \mathcal{Q} - \mathbf{S}\mathbf{B}\mathbf{R}^{-1}\mathbf{B}^T\mathbf{S} = \mathbf{0}. \tag{3-9}$$

Practical application of the LQR poses the significant challenge of obtaining the complete state vector $\mathbf{x}$. Experimentally, access is not granted to $\mathbf{x}$ but rather to a measurement vector $\mathbf{y}$, which is related to the states according to

$$\mathbf{y}(t) = \mathcal{C}\mathbf{x}(t) + \mathbf{m}(t), \tag{3-10}$$

where $\mathcal{C}$ is a 3×6 matrix, known as the output matrix (for more details about

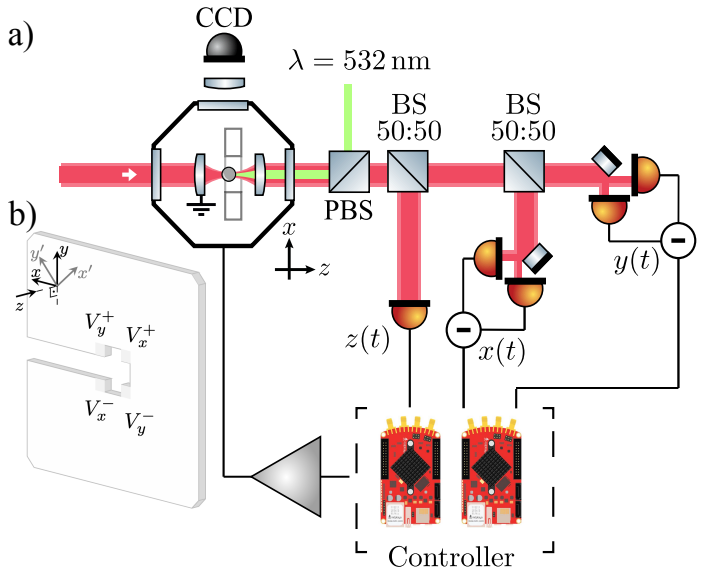

Figure 3.1: Experimental setup. a) Simplified scheme of the setup. An optical tweezer is assembled within a vacuum chamber, and a CCD is used for imaging of the tweezed particle upon illumination with a 532 nm laser beam. The trapping lens is grounded, and detection of forward-scattered light is used to generate the electrical feedback signal sent to the electrodes. The collection lens works as the z-electrode, whilst the board shown in b) is placed close to the trap's focus and contains the x- and y-electrodes. The axes at the top left indicate the orientation between the electrodes' axes (x', y') and the coordinate system of the detection. We note that, along with an appropriate choice of design parameters, sufficient proximity between the center of the PCB and the tweezer focus ensure that the beam is not cropped by the board.

its structure we refer to Appendix B.3). The term $\mathbf{m}$ is the measurement noise vector and can be expressed as $\mathbf{m} = \begin{bmatrix}\zeta_x(t) & \zeta_y(t) & \zeta_z(t)\end{bmatrix}^T$. Here $\zeta_i(t)$ are zero-mean white-noise processes with variance σ_i^2, satisfying

$$\langle \zeta_i(t) \rangle = 0, \tag{3-11a}$$

$$\langle \zeta_i(t)\zeta_j(t+\tau) \rangle = \sigma_i^2 \delta_{ij} \delta(\tau). \tag{3-11b}$$

On the one hand, measurements of $x(t)$, $y(t)$ and $z(t)$ can be implemented by collecting forward or backward-scattered light from the NP [51]. On the other hand, the velocities are not accessible experimentally. An optimal estimation $\hat{\mathbf{x}}$ can be computed by applying real-time filtering techniques to estimate $\mathbf{x}$. For linear dynamics where the disturbances and measurement noises adhere to Eq. (3-2) and (3-11), $\mathbf{x}$ is best estimated using the Kalman filter [128, 129].

Implementing the Kalman filter significantly increases the complexity of the feedback loop. As a simplification, it is possible to estimate the velocity as being proportional to a delayed position measurement. This approach has proven successful for cooling one of the spatial degrees of freedom of the levitated NP [84], albeit increasing the minimal effective temperature achievable. The effective temperature for each axis can be computed by using the integral [45]

$$T_{\text{eff}}^{i} = \frac{m\Omega_i^2}{k_B} \int_0^\infty \left(1 + \frac{\Omega^2}{\Omega_i^2}\right) S_{ii}(\Omega)\, d\Omega - \frac{1}{2}, \tag{3-12}$$

where S_{ii} is the double-sided Power Spectral Density (PSD) for the particle's motion along the i-axis, expressed as

$$S_{ii} = \frac{2\gamma_m k_B T}{m[(\Omega^2 - \Omega_i^2)^2 + \gamma_m^2 \Omega_i^2]}, \tag{3-13}$$

Note the PSD is computed directly from measurements of the particle's position.

3.1.3 Experiment

The experimental setup is schematically illustrated in Fig. 3.1a. A CW laser at 1550 nm (RIO Orion) amplified by an Erbium-doped fiber amplifier (Keopsys CEFA-C-BO-HP-SM) is used to produce a high-quality Gaussian beam linearly polarized along the x direction with a power of $P_t \approx 2\,\text{W}$, at the output of a single-mode fiber. The beam is focused by an aspheric lens (Thorlabs C330TM-C, NA = 0.68) assembled inside a vacuum chamber, allowing for stable optical trapping. The light scattered by the particle along the forward direction is collimated by a collecting lens (Thorlabs C110TM-C, NA = 0.40). Silica NPs (diameter 143 nm, MicroParticles GmbH) are loaded into the vacuum chamber by a nebulizer and trapped at atmospheric pressure. The trapped particle oscillates with resonance frequencies along the three axes given by $\Omega_x/2\pi = 96.24\,\text{kHz}$, $\Omega_y/2\pi = 101.49\,\text{kHz}$ and $\Omega_z/2\pi = 31.52\,\text{kHz}$.

Detection of transversal motion, $x(t)$ and $y(t)$, is carried out using balanced photodiodes (Newport 2117-FC), while information about the longitudinal $z(t)$ direction is obtained by direct intensity photodetection. The optical trap is characterized through measurements of the particle's position PSDs for each direction. Information on the occupation numbers and effective temperatures of each direction can also be obtained from the PSDs by using Eq. (3-12).

A PCB containing two orthogonal pairs of electrodes, illustrated in Fig. 3.1b), is placed in the vicinity of the optical trap's focus, allowing for two-dimensional electrical feedback control of the NP's CoM motion. The PCB has a thickness of 1.5 mm and is designed to be compatible with cage plate optical systems (Thorlabs SP02). The four square-shaped contacts ($2 \times 2\ \text{mm}^2$) around

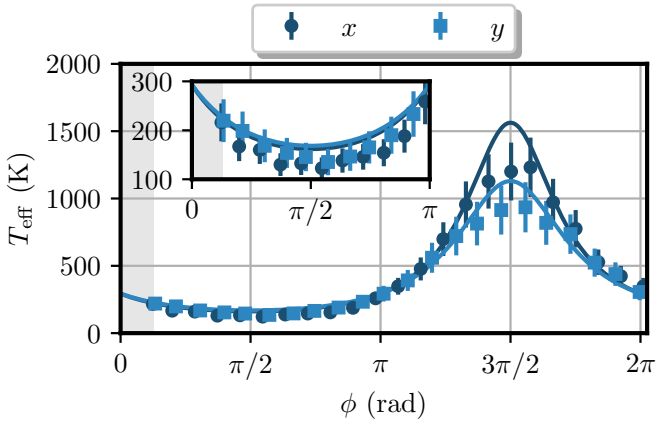

Figure 3.2: Effect of delayed feedback forces. Comparison between experimental results and theory (solid lines) is presented. Measurements were conducted at room temperature (293 K) and a pressure of 1.2 mbar. Each data point corresponds to 10,000 50 ms-traces. The used gains were $G_x = (9.17 \pm 0.98) \times 10^{-9}$ N/m and $G_y = (8.97 \pm 0.97) \times 10^{-9}$ N/m. The gray shaded area marks the region that could not be measured due to the minimal delay imposed by the electronics. The horizontal axis, ϕ, represents the phase $\Omega_i \tau_i$ introduced by the delay. In the inset, the interval where the delay induces cooling is presented with more detail.

its center are arranged symmetrically, with a separation of 2.5 mm between adjacent contacts. Note also that only coarse alignment of the PCB with respect to the levitated NP is required, and this can be achieved by placing the PCB near the optical focus. Due to the employed control method, coupling between degrees of freedom in the transverse plane is compensated by the calibration process.

A third pair of electrodes is implemented by applying an electric signal to the mount of the collection lens, producing a voltage difference with respect to the grounded trapping lens. Simulations conducted using the finite-elements method have numerically demonstrated that this voltage difference establishes a uniform electric field near the particle's position [55]. The signal from the detection is digitally processed by two FPGAs (STEMlab 125-14, Red Pitaya) and analogically amplified before being fed back to the electrodes. We remove any cross-talk between z and xy electrodes by digital filtering, which is facilitated by the difference in characteristic frequencies between the longitudinal and transversal degrees of freedom. Taking this and the geometry of the actuators into consideration, the gain matrix assumes a block diagonal form,

$$\mathbf{K} = \begin{bmatrix} \mathbf{K}_{p,xy} & 0 & \mathbf{K}_{d,xy} & 0 \\ \mathbf{0}_{1\times 2} & k_{p,z} & \mathbf{0}_{1\times 2} & k_{d,z} \end{bmatrix}. \tag{3-14}$$

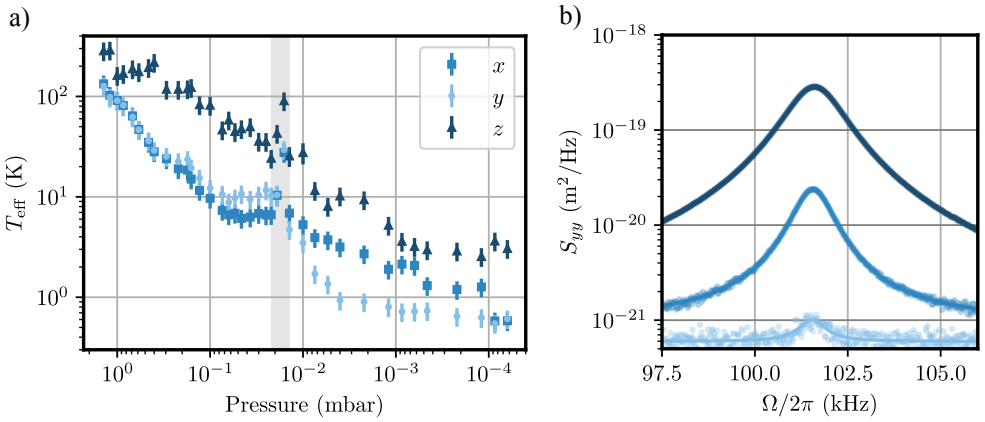

Figure 3.3: All electrical cooling. a) Dependence of x, y and z effective temperatures on pressure, calculated using (3-12). The grey shaded region shows a region of instability, as discussed in the main text. b) PSD of the y motion. Measurements were made at 1.0 mbar(—), 5.4×10^{-2} mbar (—) and 1.2×10^{-4} mbar (—).

A detailed description of the analogical amplification and the digital processing of the detection signal can be found in Appendix B.2. Digital processing includes frequency filtering, delaying and application of derivative/proportional gains to the signal. The choice of optimal gains was based on control theory, as presented in Appendix B.1. Since the theory predicts only a weak dependence of optimal gain on pressure, we consider a single gain to be optimal throughout the experiment.

Appropriate calibration of the electrodes accounts for misalignment between the electrodes' axes and the mechanical modes, allowing for a partial reconstruction of the **B** matrix, which assumes a 45° rotated form with respect to the diagonal matrix given by Eqs. (3-1). During calibration, the effect of the z-electrode was observed to be too weak, such that only the x- and y-electrodes could be calibrated. This has led to applying the control LQR only to the x and y motion and a cold damping protocol [45, 83] along the z direction ($k_{p,z} = 0$). We refer to Appendix B.3 for more information on the calibration procedure.

3.1.4 Results

Proper implementation of the control method as previously described requires precisely delaying each detection signal. The delay characterization process involves applying a force proportional to the delayed position independently in the x and y directions. For instance, referring to Eq. (3-1), this translates to $u_x = G_x x(t - \tau_x)$ for the x coordinate (and similarly for y and z). Each delay τ_i consists of two components, the intrinsic electronic delay

$\tau_{e,i}$, and an adjustable delay $\tau_{c,i}$. Fig. 3.2 shows measures of T^x_{eff} and T^y_{eff} while subjecting the particle to the delayed force. The controllable delay $\tau_{c,i}$ was varied to span the range of τ_i from $\tau_{e,i}$ to one period of oscillation ($\phi = 2\pi$). The experimental results show excellent agreement with the theoretical predictions from [120]. Furthermore, this measurement allowed for the characterization of the electronic delays, $\tau_{e,x}$ and $\tau_{e,y}$, both of which were determined to be $0.639\,\mu$s. We assume $\tau_{e,z}$ has the same value.

Figure 3.3a) shows the results of 3D feedback cooling. The minimal effective temperatures achieved in the experiment are $T^x_{\text{eff}} = (0.58 \pm 0.12)\,\text{K}$, $T^y_{\text{eff}} = (0.55 \pm 0.11)\,\text{K}$ and $T^z_{\text{eff}} = (3.63 \pm 0.77)\,\text{K}$, for each of the three axes. The gray shaded area in Fig. 3.3a) depicts an instability region observed near $10^{-2}\,\text{mbar}$, characterized by a sudden increase in T^i_{eff}. We attribute this phenomenon to variations on the net charge of the NP [17]. The net charge acts as a linear parameter affecting the input matrix, thus linearly impacting the control gain. As electrode calibration was performed at high pressure ($> 1\,\text{mbar}$), for pressures smaller than 0.01 mbar, it cannot be assumed that the applied gain was optimal. Nonetheless, stable cooling has been implemented by using only electrical actuators and the application of LQR returned a gain matrix capable of handling any coupling between degrees of freedom in the dynamics. The PSD of the CoM motion for the y direction under three distinct pressures is shown in Fig. 3.3b). Feedback cooling not only reduces the area of the PSD, from which the effective temperatures are estimated, but also introduces a term which increases its linewidth, as expected due to the presence of derivative terms in the NP's motion.

For pressures smaller than 0.01 mbar, no instability has been encountered, agreeing with results previously shown [130]. Therefore, the control protocol employed should be capable of successfully controlling the NP until the stochastic thermal force becomes negligible and the dynamics starts to be dominated by measurement back-action and photon recoil heating. When compared to parametric cooling, an all electrical approach is advantageous since it avoids contamination of the signal by spurious modulation signals, which are rendered unnecessary. Additionally, in contrast to parametric cooling, the LQR employs a linear control law, thus not affecting the overall linearity of the system.

Since the LQR has been successfully employed in combination with Kalman filter for ground-state cooling along the longitudinal axis [48], extending its application as a 3D quantum control policy should be experimentally achievable. By considering the electrode parameters presented in Appendix B.3, an implementation of a Kalman filter for state estimation and the trapping and

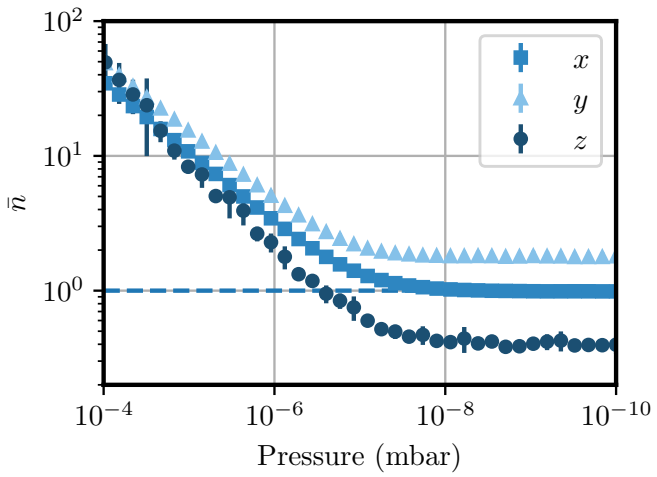

Figure 3.4: Simulation of optimal all electrical 3D cooling with improved trapping lens and detection scheme: expected thermal occupation numbers $\bar{n}$, obtained from the estimation of the particle's covariance matrix, as a function of pressure for the x, y and z directions. Dashed line marks a single phonon. Error bars correspond to one standard deviation over 30 simulation runs.

detection efficiency parameters reported in [48], we numerically simulated 3D all electrical cooling of a trapped NP. Figure 3.4 presents the expected final mean occupation numbers with our all electrical controller. To account for quantum effects, the same parameters of measurement uncertainty, detection efficiency η_z and backaction provided in [48] were taken into account in the simulation. Note that the simulation considers a backward detection scheme, resulting in a higher detection efficiency for the longitudinal axis compared to the transversal axes, thereby leading to a smaller thermal occupancy for z. In contrast, the experiment employed a forward detection scheme, therefore yielding the opposite effect due to limited detection efficiency [51]. The detection efficiency along the transverse axes, η_x and η_y, were computed by considering the expected proportion between the efficiency along x and y and the longitudinal directions for the corresponding trap's NA [51]. Such efficiencies led to detection imprecisions of $1.561 \times 10^{-20}\,\mathrm{m}^2/\mathrm{Hz}$, $3.122 \times 10^{-20}\,\mathrm{m}^2/\mathrm{Hz}$ and $5.204 \times 10^{-21}\,\mathrm{m}^2/\mathrm{Hz}$ for x, y and z, respectively. For pressures on the order of $1e{-}10\,\mathrm{mbar}$, the simulation results agree with the experimental findings in [48]. It must be noted that, for higher pressures, we expect that experimental imperfections increase the minimum number of phonons . Moreover, while it is evident that in simulation the thermal occupancy for y exceeds that of x, the experimental results in Fig. 3.3.a) shows the opposite. This most likely arises from experimental imperfections due to detection efficiency in the x-axis. Note that systematic errors in the experiment,

such as errors in the NP's mass, density, and charge, or imperfections in the calibration processes, alter the calculation of optimal gain and, consequently, the performance of the cooling protocol.

3.1.5 Conclusions

In conclusion, we have demonstrated an all electrical feedback cooling scheme for reducing the CoM temperature of a levitated NP in high vacuum. Through a simple custom-designed electrical actuator, we have shown sub-Kelvin temperatures for the transverse directions of motion, avoiding the use of nonlinear feedback cooling schemes such as parametric feedback cooling. This greatly simplifies levitated optomechanics experiments by avoiding the need for modulation of the trapping power. Numerical simulations point that future improvements over our setup, in particular implementation of a higher NA trapping lens and of the optimal backward detection scheme reported in [48], should enable all electrical 3D cooling near the ground state.

3.2 Backward detection

A few modifications have been applied to our previous setup (illustrated by Fig. 3.1). The updates consisted of i) removing the 532 nm beam, ii) exchanging the knife-edge forward detection scheme with a QPD, iii) increasing the NA of the tweezing lens, iv) implementing a polarization-based detector for librational motion and, finally, v) assembling a scheme for collection of backscattered light from the tweezer. The updated setup is illustrated in Fig. 3.5. About 800 mW of optical power from a CW 1550 nm laser beam is split between input to an EDFA (99%) and generation of a local oscillator (LO, 1%). The polarization controller (PC) denoted by PC2 defines the polarization of the beam which is directly coupled to free-space after the EDFA. PC2 aligns the polarization for maximal transmission through the first free-space polarizing beamsplitter (PBS). Forward scattered light from the tweezer is split into transversal detection (denoted by x, y-detection in the Figure) and libration detection. Transversal detection is carried out using a PDQ30C quadrant photodetector (QPD) from Thorlabs. Libration detection is implemented by splitting the polarization components of the forward scattered beam into two arms of a balanced photodetector (BPD), which yields a signal containing information about the particle's angular degrees of freedom. Before the vacuum chamber, the faraday rotator (FR) and the half-waveplate ensure collection of backscattered light from the tweezed nanoparticle, which is coupled to the

z-detection system. Each transmission of the beam through the FR rotates its polarization by 45°, such that after being transmitted twice it is directed to the reflecting arm of the first PBS, and led into the backward detection scheme. The function of the half-waveplate is to realign the polarization to the transversal detection axes, in the context of splitting the detection along the CoM modes between the QPD channels - an operation which is effectively undone in the backwards transmission through the waveplate. PC1 and the PBS split the optical power of the LO between heterodyne measurement, which is to be implemented in the future and will yield absolute effective temperature measurements, and the homodyne detection of the particle's position using backscattered light, previously described. The LO polarization is aligned with that from the backwards collected beam. Phase-stabilized interference using a 50:50 beamsplitter and PID control of a phase shifter acting upon the LO yield the backward detected signal. Before moving on to the cooling results, we detail on some aspects regarding the preparation, optical alignment and verification of these modifications.

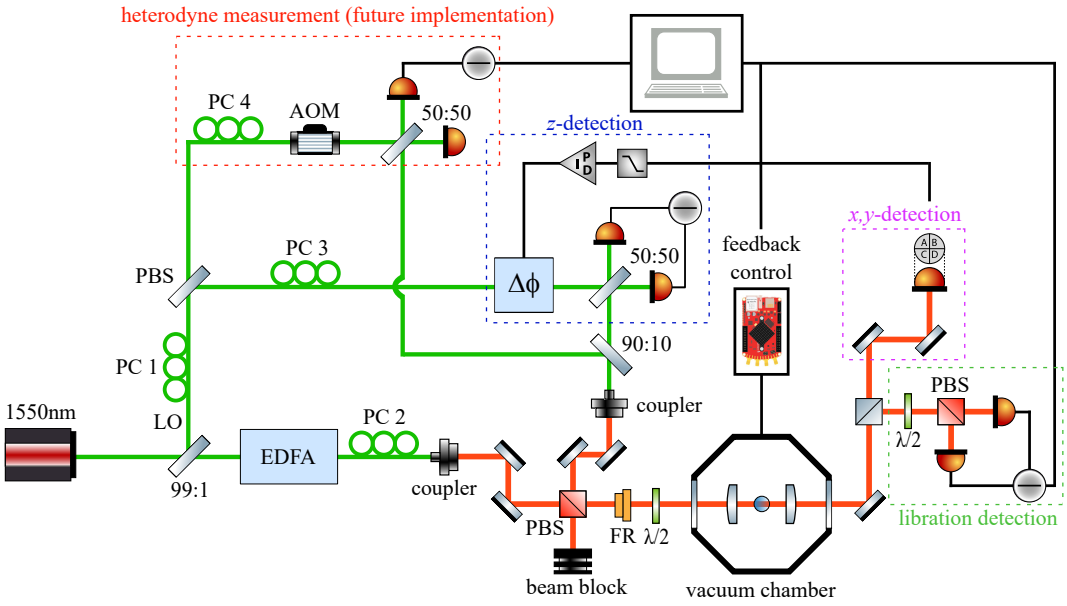

Figure 3.5: Uptaded optical tweezer setup. Polarization controllers are denoted by PC, and $\Delta\phi$ represents the phase shifter which stabilizes the interference for backward detection. The detection system is composed of four blocks: libration detection, which gives information regarding the angular degrees of freedom of the tweezed nanoparticle, x, y-detection, which yields transversal motion measurement, z-detection, which represents the backward detection system in the figure, and a yet to be implemented heterodyne measurement, which will provide absolute temperature measurements for motion along. These detection subsystems are better detailed in the main text.

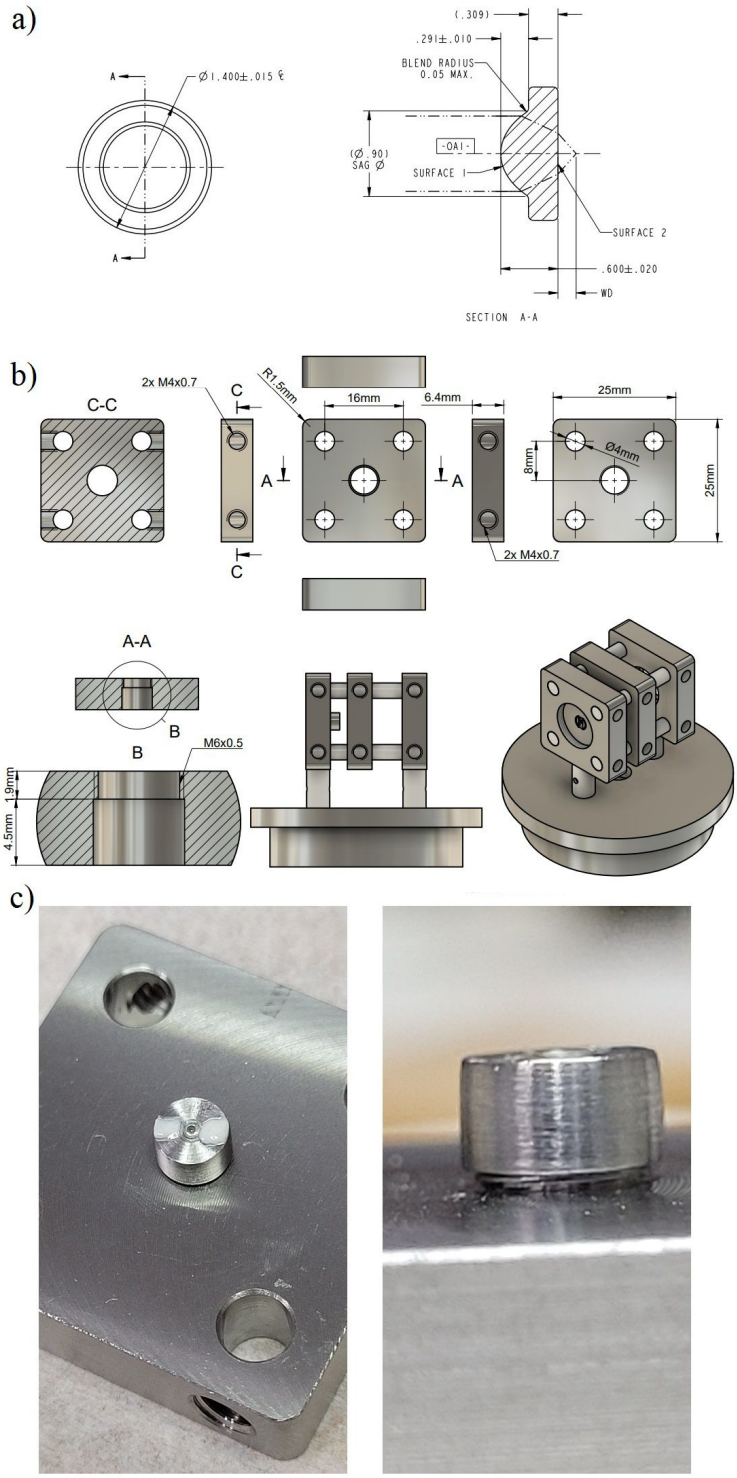

Figure 3.6: Tweezer mount and trapping lens. The Lightpath 355617 aspheric lens, dimensions given by the technical drawing in panel (a), was glued into the custom made cage plate system illustrated in the technical drawings from panel (b) using vacuum epoxy, as described by the main text. In (c) we show a picture of the lens glued into its respective supporting piece, which in its turn is held by an appropriately threaded plate.

The QPD used is the PDQ30C model from Thorlabs, which has a responsivity of 1.05 A/W @ 1550 nm. In order not to damage or saturate the QPD, we input up to roughly 760 μW optical power to the detector, using appropriate filters so as to attenuate the collected light from the tweezer in the forward direction.

The trapping NA was enhanced from 0.68 to 0.75 by using a new aspheric lens from Lightpath, model 355617, kindly provided to us by Prof. Joanna Zielińska (Tecnológico de Monterrey) and Prof. Lukas Novotny (ETH Zurich). Its dimensions are introduced by panel (a) of Fig. 3.6. In particular, the 1.4 mm total diameter of the new aspheric lens has prompted us to design a new mount for the tweezer, illustrated in its turn by the technical drawings from panel (b) of Fig. 3.6. Lastly, panel (c) of the same Figure shows pictures of the trapping lens after it was glued into its custom made cage plate using vacuum-compatible epoxy. The cage plates are connected by four Teflon rods, and the system is held onto the bottom of the vacuum chamber using a base which is compatible with the utilization of vacuum designed screws.

The 900 μm clear aperture of the trapping lens required us to modify the collimation system which transfers the beam from fiber optics to free space. The last polarization controller (denoted by PC2 in Fig. 3.5) prior to free space has a fiber specification given by the code CCC1310-J9, which corresponds to a mean field diameter of 9.7(5) μm. Given a focal distance f, a wavelength λ and a collimated beam waist w_0, the waist at the focus w is given by

$$w = \frac{\lambda f}{\pi w_0}. \tag{3-15}$$

Equating w to half the fiber's mean field diameter and w_0 to the trapping lens' effective diameter, we get $f \approx 4.42$ mm. We have used the C230TM-C aspheric from Thorlabs, which has a focal distance of 4.50 mm, as the collimating lens. The corresponding beam diameter at the focus is 916 μm.

Given the non-monotonic dependence of forward detection efficiency of particle motion along the optical axis (z) as a function of collection NA [51], the introduction of the 355617 aspheric induced also a modification of the collection lens. We have chosen the N414TM-C model from Thorlabs, which has an NA of 0.47 and a theoretical resulting forward detection efficiency for motion along the z-direction of 6.57×10^{-4}, close to the limit of about 6.63×10^{-4} for our system. Given our goal of implementing backward detection of motion along the z-axis, it may seem contradictory to base our choice of collection lens upon the efficiency of forward detection along this direction. It should be kept in mind that the assembly of the tweezer was made prior to the transition from

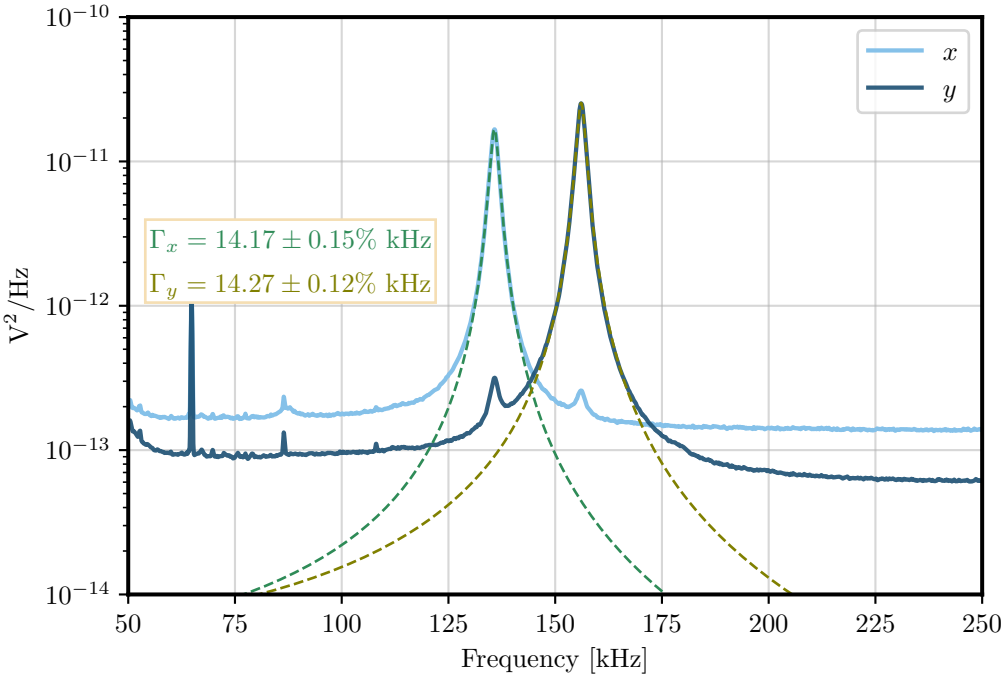

Figure 3.7: Transversal power spectral densities. Calculated curves are obtained from the mean of a thousand PSDs of 50 ms-long individual traces taken at a pressure of 3.0 mbar from the QPD channels. They are displayed in the same window and fitted by relativistic Breit-Wigner models. From these fits we extract the damping coefficients of $\Gamma_x = 14.17 \pm 0.15\%$ kHz and $\Gamma_y = 14.27 \pm 0.12\%$ kHz.

forward to backward detection in our setup, at a stage where we were still strongly reliant upon forward detection for measurement of longitudinal motion. Now, this stands out as a direction of improvement for the setup in the near future, considering that transversal detection efficiency increases monotonically with collection NA, saturating at the value of the trapping NA [51].

The increase in trapping NA has led to an increase also in the optical trapping frequencies. In comparison with the previously reported transversal frequencies of $\Omega_x/2\pi = 96.24$ kHz and $\Omega_y/2\pi = 101.49$ kHz, we now have the values of $\Omega_x/2\pi = 135.77$ kHz and $\Omega_y/2\pi = 156.08$ kHz. The power spectral densities of the signal derived from the x and y QPD channels at a pressure of 3.0 mbar are displayed in Fig. 3.7. The obtained curves are obtained from an average of a thousand PSDs of 50 ms-long individual traces. Overlayed upon these spectral densities are the respective model fits, from which we extract the damping coefficients of $\Gamma_x = 14.17$ kHz $\pm 0.15\%$ and $\Gamma_y = 14.27$ kHz $\pm 0.12\%$.

As reported in [131], dumbbell particles can be identified from the ratio between measured damping coefficients for motion along each of the transversal directions. From the damping coefficients highlighted in Fig. 3.7, we obtain a

ratio given by $\Gamma_y/\Gamma_x = 1.007 \pm 0.002$, indicating that the tweezed particle for which the corresponding data is acquired is indeed a single particle.

Along the lines of characterizing the optically trapped nanoparticles in our system, one significant drawback of our previous experiment was the lack of other objective criteria for estimating their shape. We have enhanced our system in this direction by implementing a detector for librational motion of the silica NPs, consisting of a simple combination between a half-waveplate, a polarizing beamsplitter PBS and a BPD in the forward direction. Due to silica's birefringence, rotational degrees of freedom of the oscillator become enconded into the polarization of the forward scattered light. The half-waveplate aligns the polarization orientation to the PBS axes, and each component is introduced into one arm of a BPD, allowing us to perform an indirect measurement of these degrees of freedom. The references in [132, 133] show the librational PSDs for a halter-like (or dumbbell) particle, composed of two bound spherical NPs, and for a cluster of particles. While the former is composed of a central peak with two symmetrical side bands, the latter has an asymmetrical profile with two shoulders. In contrast, a spherical nanoparticle does not exhibit any spectral information regarding librational degrees of freedom, due to the symmetry of its inertia tensor. Fig. 3.8 shows our libration measurements, which help us infer what kind of particle is trapped at each run of the experiment. Characteristic librational PSDs of halters and of nanoparticle clusters are shown, and a clear distinction between them can be drawn. In Fig. 3.9, we cross-validate our shape measurement in the dumbbell case by verifying that the transversal damping coefficients for the dumbbell are not the same. We measure the damping coefficients of $\Gamma_x = 18.86 \pm 0.18\%\,\mathrm{kHz}$ and $\Gamma_y = 18.38 \pm 0.10\%\,\mathrm{kHz}$, amounting to a damping coefficient ratio of $\Gamma_x/\Gamma_y = 1.026 \pm 0.002$.

Backscattered light is collected from the tweezer by introducing a PBS, a faraday rotator (FR) and a half-waveplate prior to the vacuum chamber. The polarization of light output from the PBS is rotated by 45° in-plane each time it passes through the FR. In this way, when the backward detected beam reaches the PBS again, its polarization is orthogonal to that of the incident beam, thus getting reflected by the element. The half-waveplate is inserted to make the polarization orientation compatible with that of the QPD axes before introducing it into the tweezer, an operation which is compensated for by the same waveplate in the back propagating beam. We then couple the collected light to the fiber system where detection actually takes place. Another detail regarding collection of backscattered light is that we tilt the vacuum chamber, since spurious reflections of the incident light have been observed to be generated by its viewports. These reflections mix with the signal beam at

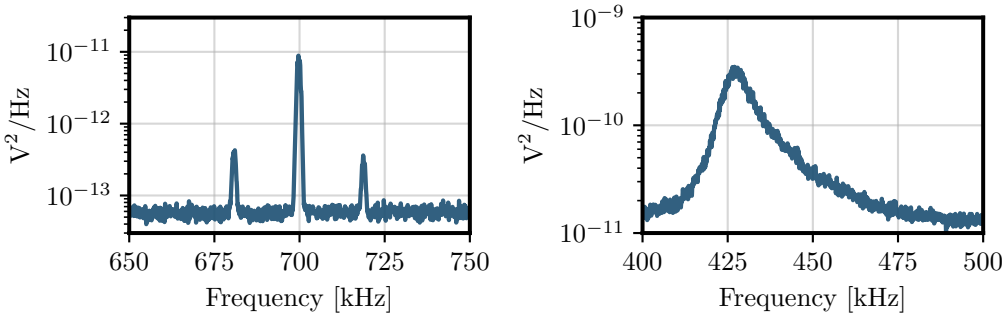

Figure 3.8: Libration detection. We show the characteristic librational peaks observed when the tweezed object is a nanodumbbell (left) or a cluster of nanoparticles (right). Even though the spectral peaks were observed at different frequencies, their shapes have allowed us to swiftly determine what kind of particle was trapped each time we ran the experiment.

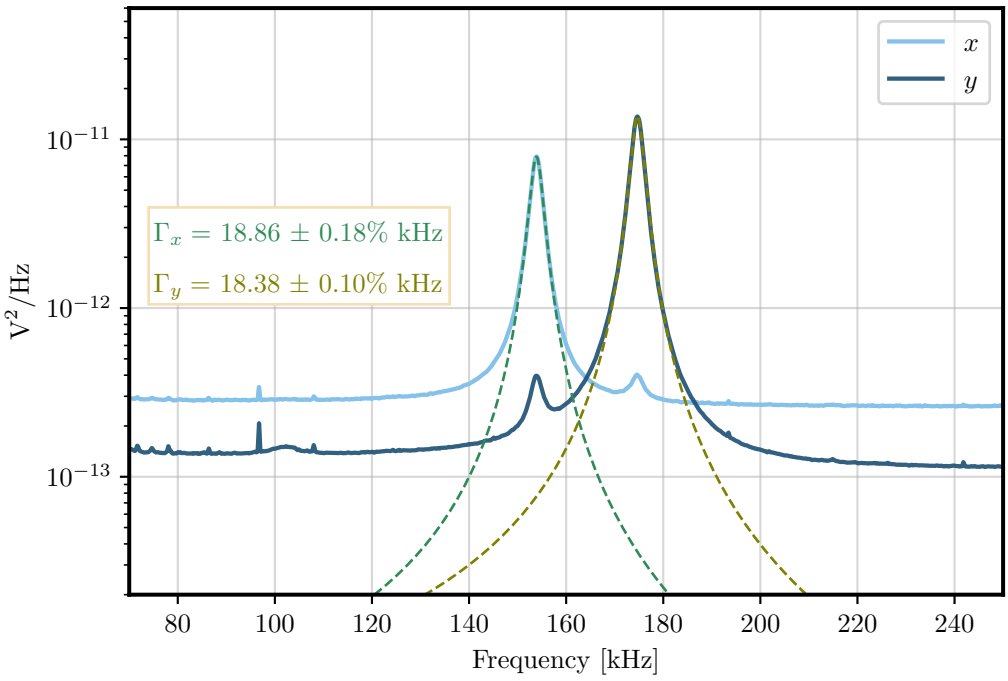

Figure 3.9: Nanodumbbell transversal PSDs. Calculated curves are obtained from the mean of five thousand PSDs of 50 ms-long individual traces taken from the QPD channels. They are displayed in the same window and fitted by Breit-Wigner models. From these fits we extract the damping coefficients of $\Gamma_x = 18.86 \pm 0.18\%\,\mathrm{kHz}$ and $\Gamma_y = 18.38 \pm 0.10\%\,\mathrm{kHz}$. As expected for a nanodumbbell, the transversal damping coefficients are different, we obtain a ratio of $\Gamma_x/\Gamma_y = 1.026 \pm 0.002$

normal incidence, compromising the backward detection scheme.

Linear detection of motion in the forward scheme requires simply focusing the collected light on a photodetector. Interference between light scattered by the nanoparticle and portions of the beam not scattered by the tweezer allows for direct measurement of the phase of the forward scattered beam [52]. In this sense, the portions of the beam which did not interact with the particle provide a phase reference for the measurement of its motion. By design, the backward detection scheme does not come with intrinsic phase referencing, such that we are required to generate an LO. This is carried out by passing the non amplified beam through a 99:1 beamsplitter and selecting the least intense arm, while the remaining optical power is sent to the EDFA. A polarization controller allows for polarization alignment between the LO and the signal beam. A phase shifter (PZ2 Fiber Stretcher from Optiphase) is introduced in the path of the LO, the beams are combined in a 50:50 beamsplitter and input to a BPD, yielding the measurement. The phase shifter is controlled by an FPGA-implemented PID-loop using the BPD output. Here, we aim to stabilize the low-frequency components of the interference, such that the BPD signal oscillates around zero voltage. Due to mechanical vibrations and to polarization drifts associated with temperature variations, the near-DC component of the phase between LO and signal fluctuates. Resonances from the fiber stretcher circuit at 18 kHz and at 110 kHz prompted us to low-pass the control signal using a fifth-order analogical filter. The FPGA's DAC (digital-to-analog converter) output range is limited to ± 1 V, such that we also include an analogical gain in order to bring the control signal up to the 15 V range. The simulated Bode diagram of the filter is presented by Fig. 3.10, and the corresponding cut frequency, where there is an amplitude loss of 3 dB with respect to the DC load, is of about 192 Hz.

By compensating for the low frequency oscillations in the interferometer, we manage to improve the SNR of the backward z-detection. Fig. 3.11 shows PSDs of 500 ms-long traces taken at different times, showing how the interference at the BPD drifts on the time scale of a few seconds when the stabilization loop is turned off, an effect which we associate with room temperature oscillations – see Appendix C for a discussion on this point. A measurement with the control system enabled is also shown in the background. Within the corresponding PSD, one can notice how phase stabilization leads to strong attenuation of the second harmonic of the z-detection at about 105 kHz, while the first harmonic at $\Omega_z = 52.61$ kHz is enhanced.

Next, we comment on our detector and electrode calibrations. We follow a protocol similar to the one described in [95]. Let us briefly recall these results;

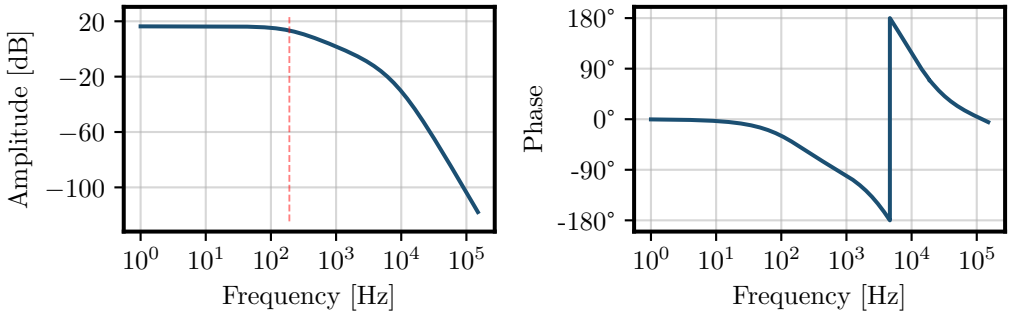

Figure 3.10: Low-pass filter for phase stabilization signal. The left and right panels show, respectively, amplitude and phase responses of the analogical low-pass filter which we apply on our phase stabilization control signal before directing it to the fiber stretcher. Inclusion of this element was necessary due to observed resonances from the stretcher circuit at 18 kHz and 110 kHz. The fifth-order filter has a cut frequency of about 192 Hz, as highlighted in the left panel. The cut frequency is defined as the frequency for which there is a 3 dB-loss with respect to the DC-response. Design and assembly of the filter were carried out by courtesy of Daniel Tandeitnik.

the one-sided power spectral density of the particle's motion along the j-th axis is approximately given by,

$$S_{x_j}^{\mathrm{th}}(\omega) = \frac{4\Gamma k_B T}{m\left[(\omega^2 - \Omega_j^2)^2 + \Gamma^2\omega^2\right]}. \tag{3-16}$$

By fitting the PSD of the output voltage to this model we can obtain a detector calibration coefficient C_{VM}^j, which characterizes the voltage response per unit displacement of the particle along the j direction,

$$S_{V_j}(\omega) = (C_{VM}^j)^2 S_{x_j}^{\mathrm{th}}(\omega). \tag{3-17}$$

Once we have calibrated our detectors, it is also relevant to quantify how much force is generated by our electrodes per unit applied voltage upon the particle. When a sinusoidal driving force is applied at a frequency ω_{dr} with an amplitude F_0, the position PSD measured over a time interval 2τ changes from $S_{x_j}^{\mathrm{th}}(\omega)$ in Eq. (3-16) to

$$S_{x_j}(\omega) = S_{x_j}^{\mathrm{th}}(\omega) + \frac{F_0^2\ \tau\ \mathrm{sinc}^2[(\omega - \omega_{dr})\tau]}{m^2\left[(\omega^2 - \Omega_j^2)^2 + \Gamma^2\omega^2\right]}. \tag{3-18}$$

In this way, after calibrating the detector, it is possible to isolate the particle's

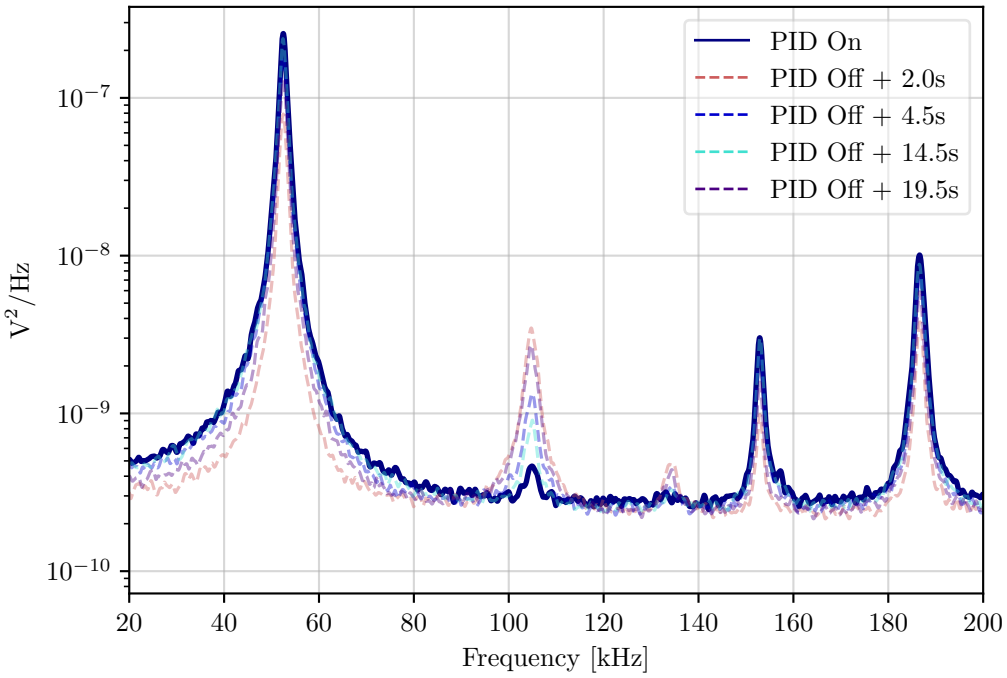

Figure 3.11: Phase stabilization demonstration. PSDs for 500 ms-long traces are shown with phase stabilization turned on (solid curve) and off (dashed curves). We measure the unstabilized signal over an interval of a few seconds and verify that, when the phase control loop is disabled, a strongly variable behavior in the measured spectra can be observed. We attribute these variations to room temperature drifts which cause the fiber optics to expand and contract at long time scales. Measurements were taken at a pressure of 0.86 mbar.

response to this drive and obtain a sequence of measured forces for different applied voltages, from which we can finally calibrate our electrodes.

To summarize what is done in practice, a sinusoidally varying voltage drive is applied to the electrodes placed in the vicinity of the particle. A "base line" PSD corresponding to the $S_{x_j}^{\mathrm{th}}(\omega)$ term is obtained by digitally notch-filtering the signal at the driving frequency, as suggested by the same reference in [95]. The value of the unfiltered position PSD at the driving frequency is compared with the base line, and using Eq. (3-18) we obtain the applied force F_0.

In the z-direction, this protocol was carried out for the two driving frequencies of 41 and 45 kHz, and for six voltage values between 0.2 and 1.0 V. Fig. 3.12 shows an example calibration fit for a voltage of 1.0 V and a frequency of 45 kHz. The calibrations for each frequency and voltage were performed in two steps. In the first step we obtain the damping coefficient, central frequency and detector calibration factor using the notch-filtered PSD as input data. Then the unfiltered data is modelled using Eq. (3-18), and from the difference

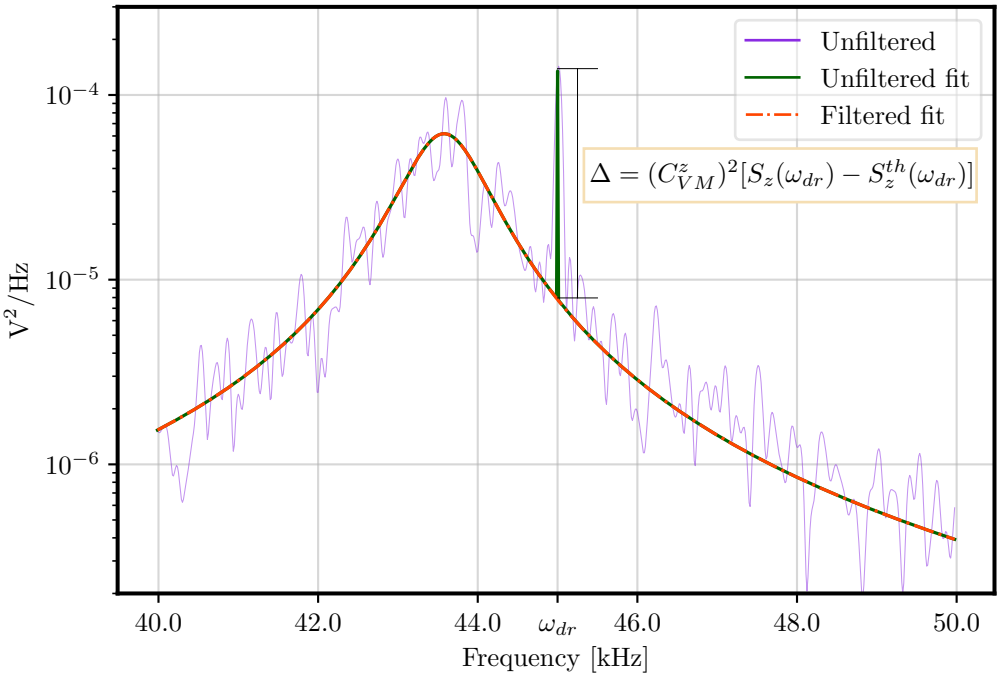

Figure 3.12: Calibration illustration. A digital notch filter at the driving frequency is applied to our measurement, and we fit this filtered data in order to obtain the central frequency, the damping coefficient and the detector calibration factor. Along with the particle's mass and the measurement time, these parameters are used to fit the drive peak and extract the applied force.

between filtered and unfiltered models at the driving frequency we obtain the applied force. By measuring the force for different voltages and frequencies, we obtain the electrode calibration factor C_{NV}^j, which is given by the best fit for the ratio between measured forces and applied biases. For the longitudinal direction, we have measured an electrode calibration factor of $C_{NV}^z = 1.556 \pm 0.038\,\mathrm{fN/V}$, whilst the best detector calibration obtained was of $C_{VM}^z = 3.16 \pm 0.002\,\mathrm{MV/m}$. It is worth noticing that the detector calibration was observed to vary over the time span of a few hours, a fact which we attributed to temperature and/or polarization instabilities in the interferometer. As it will be described shortly, this has prompted us to perform the cooling experiment as swiftly as possible, within a time interval where detector calibration was seen to remain stable, and an effective temperature could be appropriately obtained from the measured PSDs.

Another unexpected aspect of the experiment was related to the calibrations associated with the transversal directions, a problem which we report here before finally describing our cooling results. For reasons not yet understood, the sensitivity of the detectors to motion along the x- and y-directions was

very low in comparison to our results prior to the introduction of the QPD (see Appendix B.3 for the earlier results). We attribute this weak sensitivity to the unexpectedly low observed swing of the detector (a few mV), which the DACs of our oscilloscope and of the FPGA were not properly optimized to deal with. The detector calibration factors we observed in the transversal forward detection were of the order of $8 \times 10^3\,\mathrm{V/m}$, which is a factor from two to four hundred times smaller than the ones we had in the previous run of the experiment and in the presently implemented longitudinal backward detection. Aside from this poor transversal detector calibration, our transversal electrodes were also observed to actuate more weakly upon the particle than expected, with a force per unit of applied voltage about ten times smaller than what was previously obtained, an issue which might be related to the positioning between the tweezer focus and the plane where the electrodes were placed. Both of these problems are strong candidates for immediate improvement in the setup. They are to be addressed shortly with an exchange of the PCB containing the electrodes used for control, and by appropriately adapting our signal readout scheme for the forward direction. Despite the momentary inability to proper control the motion along transversal directions, we shall see that it was possible to improve the lowest effective temperatures achievable in our experiment, even if only for motion along the optical axis. Nevertheless, cooling along a single direction led to unstable dynamics at the lowest pressure ranges in which we aimed to achieve cooling. This has ultimately led to a loss of the particle in the pressure range of $10^{-4}\,\mathrm{mbar}$.

The experiment was carried out as follows. For each pressure value, we verified stabilization of the z-detection and of the feedback cooling using a scheme for live visualization of the PSD. Each time that the system was verified to be stable, we took a measurement, then lowered the pressure and waited for it to stabilize again, and repeated.

Given the lack of a reliable calibration, we replace the effective temperature calculation in Eq. (3-12) from [45] by an approximation using the ratio between a reference PSD taken at 0.86 mbar and the PSDs of the detected motion under feedback cooling. We roughly approximate the potential to be harmonic such that, by application of the Virial theorem, we have equal values for the mean kinetic and potential energies. An implicit application of the Parseval's theorem then leads us to the conclusion that there is a proportionality between the area under the PSD and the particle's energy. Then, we assume the reference PSD to be associated with thermalized dynamics at room temperature, and the effective temperature for each measurement is given by 293 K times the ratio between areas under the spectral curves of the data and of the reference.

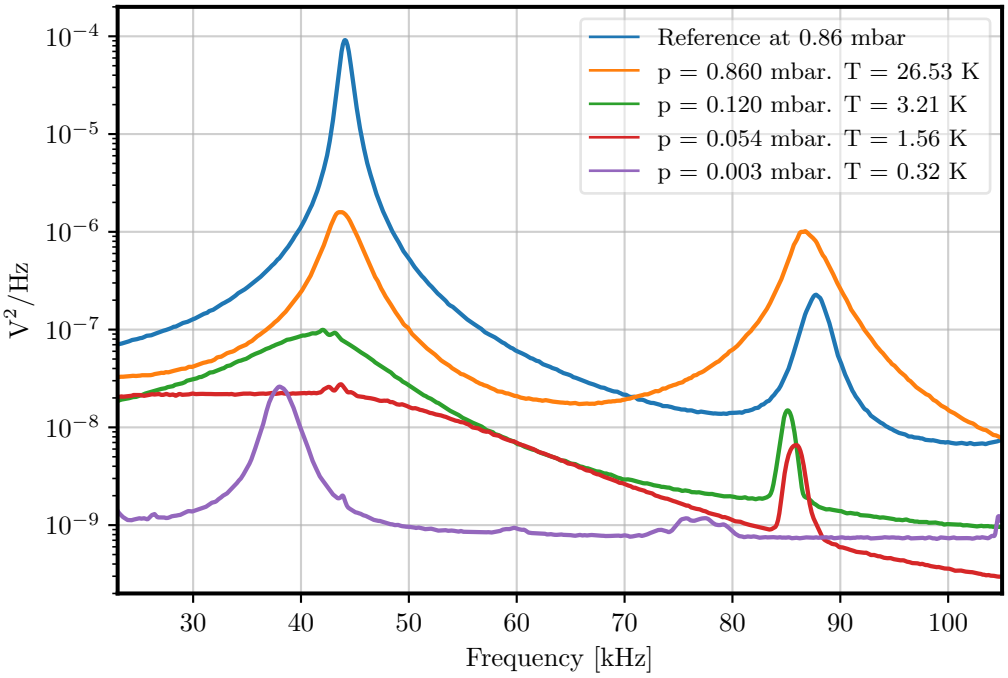

Figure 3.13: Backward cooling results. PSDs of the backward detected signal are shown for feedback cooling under different pressures. A reference PSD at 0.86 mbar is used as a replacement for the calibration factor which we noticed to be presently unstable. Temperature is calculated by assuming the reference PSD to be associated to motion at an effective temperature of 293 K, and the feedback-cooled PSD temperatures are obtained considering the area ratio between each of them and the reference.

We are also working under the assumption that the average potential energy is much larger than the zero-point energy of the oscillator, which is generally true when we are far away from the ground state.

All this being said, Fig. 3.13 displays PSDs in the backward direction for different pressures. The labels also indicate the effective temperature calculated as previously described. In this calculation, we also include the second harmonic of the longitudinal motion, which is visible in the spectra. The lowest pressure where we were able to perform stable measurements on was of 3×10^{-3} mbar. Towards the 10^{-4} mbar range, the uncontrolled motion along the transversal directions has caused us to lose the tweezed nanoparticle. Nevertheless, we have managed to attain a temperature of about 0.32 K, roughly 11 times smaller than our previous best result along the longitudinal direction, and slightly better than the previous transversal results in our setup. Notice that this mild improvement was obtained at a higher pressure than before, and under 1D feedback cooling. With a central frequency of $\Omega_z \approx 44$ kHz, our lowest

temperature is associated with a number of phonons given by,

$$\bar{n}_z^{\mathrm{bw}} = \frac{k_B T_{\mathrm{eff}}}{\hbar \Omega_z} = 1.5 \times 10^5 \text{ phonons.} \tag{3-19}$$

We compare this result with the calculated number of phonons for the z-motion previously obtained in the forward cooling experiment,

$$\bar{n}_z^{\mathrm{fw}} = 2.4 \times 10^6 \text{ phonons,} \tag{3-20}$$

which indicates an improvement by an approximate factor of 16. The result illustrated by Eq. (3-19) gives an indication of how many orders of magnitude our cooling must be enhanced in order to achieve the ground state (by convention, $\bar{n} < 1$), a goal which was already carried out by other groups, see [41,45,97,134].

4
Feedback cooled levitated nanoparticles for few photon detectors

The previous chapters detail how, in our experiments, we've learned how to electrically control an optically levitated nanoparticle using measurements of its position, and how this knowledge can be used to reduce the effective temperature of its center of mass translational dynamics. In this chapter, we describe simulation efforts which aimed to address the following question: "can such a feedback cooled levitated nanoparticle be used to detect individual photons?" We have developed a Python environment to implement numerical simulations of the dynamics of an optically trapped oscillator under feedback cooling inside a cavity resonator, as depicted in Fig. 4.1.

By inputting a low intensity coherent optical pulse into the optomechanical dynamics, we mimic the effects of a few-photon state interacting with our system. Noisy position measurements are passed through a Kalman filter algorithm, and from the resulting state estimates we attempt to infer the input pulse intensity. Within the next sections, we outline the dynamics which we've simulated using an Euler-Mayurama approach. The Kalman filter implementation is also detailed, and we follow up with an attempt at characterizing this system in regards to its capability of distinguishing states of light with very low intensity.

The code used to obtain our results is available in [135].

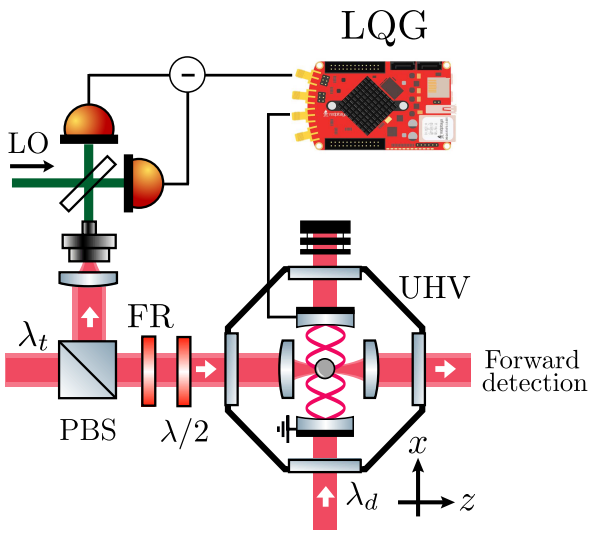

Figure 4.1: Detector schematics. A particle is levitated using a trapping beam of wavelength λ_t. Homodyne detection of the trap's backscattered light reveals information on the particle motion, which is used to feedback cool the particle to the ground state. Around the particle, a low finesse cavity tuned to wavelength λ_d enables either the coherent scattering or dispersive interaction between the mechanical motion and the field we wish to detect. Signature of the detected photon appears in the feedback error signal.

4.1 Dynamics: parameters and general framework

We simulate the linear optomechanical dynamics describing the mechanical mode of an oscillator coupled by coherent scattering to an optical mode inside a cavity with resonance frequency ω_c, and whose position can be readout by homodyne detection with efficiency η. Let Δ, κ, g, ω_m and γ_m denote the detuning, cavity linewidth, linearized optomechanical coupling rate, mechanical mode frequency and damping coefficient, respectively. We also denote by T and k_B the temperature and the Boltzmann constant. In a frame rotating at the frequency of the laser driving the cavity, $\omega_L = \omega_c + \Delta$, the dynamics of the first moments of the dimensionless optical (X, Y) and mechanical (Q, P) mode quadratures read (see, for instance, [136]),

$$\dot{X} = -(\kappa/2)X + \Delta Y + \sqrt{\kappa}X_{in} + \sqrt{\kappa/2}\xi_X(t), \tag{4-1a}$$

$$\dot{Y} = -\Delta X - (\kappa/2)Y - 2gZ + \sqrt{\kappa}Y_{in} + \sqrt{\kappa/2}\xi_Y(t), \tag{4-1b}$$

$$\dot{Z} = \omega_m P, \tag{4-1c}$$

$$\begin{aligned}\dot{P} = &-2gX - \omega_m Z - \gamma_m P + \frac{\sqrt{4\gamma_m m k_B T}}{P_{zpm}}\xi_{th} \\ &+ \frac{\sqrt{4\pi K}}{P_{zpm}}\left(\sqrt{\eta}\xi_{ba}^{(1)} + \sqrt{1-\eta}\xi_{ba}^{(2)}\right) + u(t).\end{aligned} \tag{4-1d}$$

By the dimensionless mechanical quadratures Z and P, we denote dimensionless position and momentum means. They are represented in units of their respective zero-point values, that is, $Z_{zpm} = \sqrt{\hbar/(2m\omega_m)}$ and $P_{zpm} = \sqrt{\hbar m\omega_m/2}$, with m representing the oscillator's mass. For the sake of clarity, we also emphasize that the dimensionless momentum P is not to be confused with the tweezer beam power P_{tw}, which is to be introduced shortly. We denote by u(t) an arbitrary external force associated with a control law applied upon the system. ξ_i are white noise terms with the following properties,

$$\langle \xi_i(t) \rangle = 0, \tag{4-2a}$$

$$\langle \xi_i(t)\xi_j(t') \rangle = \delta_{ij}\delta(t-t'), \tag{4-2b}$$

used to describe optical shot noise, thermal and measurement backaction fluctuations. Following the quantum Langevin description in [48] we introduce K. This is a constant which specifies the intensity of measurement backaction, and it is related to the coupling between the mechanical oscillator's motion and the measured electromagnetic field. The input terms X_{in} and Y_{in} come from an input-output formalism and account for the open cavity dynamics considered ([136, 137]). By generating time traces for these input terms, we artificially include an optical excitation on the dynamics and study the simulated system's response.

For pressures lower than 10 mbar, the damping coefficient γ_m has a linear dependence on pressure p [117, 138],

$$\gamma_m \approx \left(\frac{11.85}{\pi r_p \rho v_{gas}}\right) p, \tag{4-3}$$

where we assume a spherical silica nanoparticle with radius r_p, density ρ and refractive index n. The mass of the gas particles is denoted by $m_{gas} \approx 28.96\,\mathrm{amu} = 4.81 \times 10^{-26}\,\mathrm{kg}$, and v_{gas} is their root mean square velocity, drawn from a Maxwell-Boltzmann distribution.

Next, we describe how the cavity parameters are set for our simulation. The theory regarding optical resonators can be seen, for instance, in [139]. Given the beam's central wavelength λ and a cavity length L, the driving frequency at zero detuning is resonant with the cavity only if it is an integer multiple of the free spectral range (FSR) ν_f,

$$\frac{c}{\lambda} = n\nu_f(L) = n\frac{c}{2L}. \tag{4-4}$$

In Eq. (4-4), c is the speed of light in the medium inside the cavity, which we assume to be vacuum. In order to satisfy the resonance condition at zero detuning, given λ and L, the length used in our simulations is rounded down to the closest multiple of $\lambda/2$. The beam frequency is given by

$$\nu = \frac{c}{\lambda} + \frac{\Delta}{2\pi}, \tag{4-5}$$

and the cavity's finesse $\mathcal{F}$ can be related to its linewidth by

$$\mathcal{F} = \frac{\nu_f}{\kappa}. \tag{4-6}$$

$\mathcal{F}$ can also be obtained from the reflectances of the cavity mirrors, which we assume to be the same for both and denote as r,

$$\mathcal{F} = \frac{\pi\sqrt{r}}{1-|r|}. \tag{4-7}$$

Given an intensity I_0 externally incident to the cavity, the steady state intensity inside it is given by

$$I = \frac{I_0(1-|r|)^{-2}}{1+(2\mathcal{F}/\pi)^2\sin^2(\pi\nu/\nu_f(L))}. \tag{4-8}$$

In practice, we use Eq. (4-8) to describe the (steady state) field amplification effect which takes place inside the cavity. Assuming the cavity field buildup to happen in timescales which are negligible with respect to the period of the oscillator's motion, we simplify its treatment by including an effective amplification of the incident intensity.

The dynamics in Eq.s (4-1) assume a coherent scattering interaction between the mechanical and the cavity modes. By also introducing c, $\hbar$ ϵ_0 and the tweezer's waist and power w_0 and P_{tw}, we can obtain the cavity waist, volume and electric field amplitude w_c, V_c and E_c, as well as the particle's polarizability α, the tweezer's field E_0 and the optomechanical coupling rate g [140],

$$w_c = \sqrt{\frac{Lc}{\nu}}, \tag{4-9}$$

$$V_c = \left(\frac{\pi}{4}\right) w_c^2 L, \tag{4-10}$$

$$E_c = \sqrt{\frac{\hbar\omega_c}{2\epsilon_0 V_c}}, \tag{4-11}$$

$$\alpha = 4\pi\epsilon_0 R^3 \left(\frac{n^2-1}{n^2+2}\right), \tag{4-12}$$

$$E_0 = \sqrt{\frac{4P_{\mathrm{tw}}}{\pi w_0^2 \epsilon_0 c}}, \tag{4-13}$$

$$g = \left(\frac{2\pi}{\hbar\lambda}\right) \alpha E_0 E_c Z_{zpm}. \tag{4-14}$$

Values of g/ω_m up to about 55% have already been achieved in optomechanical experiments [138]. It has been proposed that even higher values for g could be achieved, perhaps by reduction of the cavity mode volume, and the investigation of such systems may be relevant in the context of squeezed states - see, for instance, [141].

Aside from the shot noise terms in the dynamics for the X and Y optical quadratures, there are two white noise processes in the dynamics modeled by Eq.s (4-1). The first is associated with thermalization of the oscillator's motion with the surrounding gas, while the second describes the effect of measurement backaction. As previously mentioned, we follow [48] for the introduction of the coupling constant K and of an effective detection efficiency η. We skip a thorough derivation of these results and indicate the equations which tie some of our parameters to the measurement backaction force standard deviation σ_{ba} and to the position uncertainty σ_{z} [51]. From the latter we can also extract the (discrete) measurement noise standard deviation σ_{det},

$$\sigma_{\mathrm{ba}} = \sqrt{\frac{2\hbar P_{\mathrm{scatt}}}{5c\lambda}} \tag{4-15}$$

$$\sigma_{\mathrm{z}} = \sqrt{5\frac{\hbar c\lambda}{16\pi P_{\mathrm{scatt}}}} = \sqrt{2\eta T_s}\sigma_{\mathrm{det}} \tag{4-16}$$

Where T_s is the interval between measurements and P_{scatt} is the power scattered by the dipole, given by the product between the tweezer beam intensity I_0 and the particle's scattering cross section σ_0,

$$\begin{aligned} P_{\mathrm{scatt}} &= I_0\sigma_0, \\ P_{\mathrm{scatt}} &= \left(\frac{2P_0}{\pi w_0}\right)\left(\frac{8\pi^2 m_{\mathrm{SiO2}}(n^2-1)}{\rho\epsilon_0\lambda^2(n^2+2)}\right), \end{aligned} \tag{4-17}$$

where the molecular mass of silica is denoted by m_{SiO2}.

All this being considered, we may take a minimal set of parameters which fully characterize our system in the context of simulating the optomechanical dynamics. This was the set chosen: i) for the particle, r_p, ρ and n; ii) for the

environment, p and T; iii) for the tweezer, ω_m, P_{tw}, w_0, λ and η; and, lastly, iv) for the cavity, κ, Δ and L.

Numerical simulation of this system is carried out by time discretization using an Euler-Maruyama scheme, given the presence of stochastic terms in the dynamics. A comprehensive and well detailed explanation of the transition from a continuous to a discretized time description of the dynamics is given in the MSc thesis [32] from our group, and also in [48]. Let us denote by δt the time step separating adjacent timestamps of our simulation. We write the continuum dynamics in Eq.s (4-1) as a vector equation, with $\mathbf{x}(t)$ representing the four-component state at a time t,

$$\dot{\mathbf{x}}(t) = \mathcal{A}\mathbf{x}(t) + \mathbf{B}u(t) + \mathbf{w}(t) + \mathbf{u}_{opt}(t), \tag{4-18}$$

where $\mathbf{w}(t)$ contains the noise terms previously defined and we introduce the following definitions,

$$\mathcal{A} = \begin{bmatrix} -\kappa/2 & \Delta & 0 & 0 \\ -\Delta & -\kappa/2 & -2g & 0 \\ 0 & 0 & 0 & \omega_m \\ -2g & 0 & -\omega_m & -\gamma_m \end{bmatrix}, \quad \mathbf{B} = \begin{bmatrix} 0 \\ 0 \\ 0 \\ 1 \end{bmatrix}, \quad \mathbf{u}_{\text{opt}} = \begin{bmatrix} \sqrt{\kappa}X_{in} \\ \sqrt{\kappa}Y_{in} \\ 0 \\ 0 \end{bmatrix}. \tag{4-19}$$

Time discretization is carried out by integrating the equation of motion in Eq. (4-18) from t to $t + \delta t$. Let $\mathbf{x}(t_n)$ be denoted by $\mathbf{x}_n$, $\mathbf{x}(t_n + \delta t)$ by $\mathbf{x}_{n+1}$ and analogously so for $u(t_n)$, $\mathbf{w}(t_n)$ and $\mathbf{u}_{\text{opt}}(t_n)$. Then,

$$\begin{aligned} \mathbf{x}_{n+1} &= \mathrm{e}^{\mathcal{A}\delta t}\mathbf{x}_n + \int_0^{\delta t} \mathrm{e}^{\mathcal{A}(\delta t - \tau)}(\mathbf{B}u_{\mathrm{k}} + \mathbf{w}_{\mathrm{k}} + \mathbf{u}_{\text{opt,k}})d\tau, \\ \mathbf{x}_{n+1} &= \mathcal{A}_d\mathbf{x}_n + \mathbf{B}_d u_{\mathrm{k}} + \bar{\mathbf{w}}_{\mathrm{k}} + \bar{\mathbf{u}}_{\text{opt,k}}, \end{aligned} \tag{4-20}$$

Where the integral may be performed to yield ($\mathcal{I}$ is the identity matrix),

$$\mathcal{A}_d = \mathrm{e}^{\mathcal{A}\delta t}, \quad \mathbf{B}_d = (\mathcal{A}_d - \mathcal{I})\mathcal{A}^{-1}\mathbf{B} \quad \text{and} \quad \bar{\mathbf{u}}_{\text{opt,k}} = (\mathcal{A}_d - \mathcal{I})\mathcal{A}^{-1}\mathbf{u}_{\text{opt,k}}, \tag{4-21}$$

and the white noise processes are implemented by sampling from a zero-mean gaussian distribution whose variance is given by the product between the noise autocorrelation and the simulation time step δt.

Gaussian states evolving under dynamics governed by hamiltonians no higher than second-order on bosonic creation and annihilation operators remain gaussian [142]. Given this preservation of gaussianity and the fact that to fully describe a gaussian state we only need its mean and covariance matrix, the toolkit outlined so far can be extended for simulating the quantum dynamics

of our system, as long as our initial states are gaussian. In the next section, we address how the covariance matrix evolves both in the presence and in the absence of measurements. We also introduce the manner in which those measurements are taken into account within our system. In particular, we sample the system at a decimated rate with respect to the simulation time step, and optimal estimates of the mean and of the covariance are obtained after each sampling by using a Kalman filter. With this estimation procedure in hands, we move on to detailing how the u_{k} is specified, which also depends on an optimal control method.

4.2 Measurements, optimal estimation and control

For clarity and completeness of this chapter, we state the results which were necessary for implementing the simulation framework described so far, including some which are also outlined in Sec. 3.1 and in Appendix B.1.

Based on the theory previously outlined, we can define a protocol for simulating the dynamics, given an assumed initial state. We also consider that the position of the oscillator is sampled every few simulation steps N_s, yielding a measurement y_{k} associated with a discrete white noise v_{k} whose variance is R. It is customary to define a measurement matrix $\mathcal{C}$, such that the dynamics of the simulated state and of the measurement reads,

$$\mathbf{x}_{\mathrm{k}} = \mathcal{A}_d \mathbf{x}_{\mathrm{k\text{-}1}} + \mathbf{B}_d u_{\mathrm{k\text{-}1}} + \bar{\mathbf{w}}_{\mathrm{k\text{-}1}} + \bar{\mathbf{u}}_{\mathrm{opt,k\text{-}1}}, \tag{4-22}$$

$$y_{\mathrm{k}} = \mathcal{C}\mathbf{x}_{\mathrm{k}} + v_{\mathrm{k}}. \tag{4-23}$$

Given that we measure the position and our measurement at each step results in a scalar, $\mathcal{C}$ is a 1×4 matrix with its third component being the only non-zero element. We pass the measurements y_{k} into an estimator, namely an algorithmic implementation of a Kalman filter, which is widely known for optimality in the context of state estimation and control in linear gaussian systems [143]. The book in [123] has most of the relevant information about optimal control and estimation to complement the results indicated in this section.

Before describing our Kalman filter implementation, let us first introduce some other definitions. We denote by $\hat{\mathbf{x}}_{\mathrm{k}}$ the estimate of our system's first moments at the time step k resulting from our algorithm, and by $\mathbf{\Sigma}_k^j$ the covariance matrix estimate at time step k conditioned upon the measurements up to step j. Given the iterative structure to be described shortly, it the step j is either the present step, k, or the previous one, k-1. These two "states of knowledge" are henceforth referred to as, respectively, *a posteriori* and *a*

priori, with respect to the measurement, and this notation is extended also to the estimates of the averages. This separation is introduced both for ease of interpretation and for clarity of the numerical implementation. We also denote by $\mathcal{N}$ the diffusion matrix of our system, whose diagonal terms are proportional to the noise variances and the off-diagonal terms describe their covariances.

In the continuous case, given $\mathcal{A}$ and $\mathcal{N}$, the covariance matrix of a state $\mathbf{\Sigma}$ evolves according to a Lyapunov equation,

$$\dot{\mathbf{\Sigma}} = \mathcal{A}\mathbf{\Sigma} + \mathbf{\Sigma}\mathcal{A} + \mathcal{N}, \tag{4-24}$$

which prescribes an *a priori* update of the covariance matrix estimate in the discrete case,

$$\mathbf{\Sigma}_{\mathrm{k}}^{\mathrm{k\text{-}1}} = \mathcal{A}_d \mathbf{\Sigma}_{\mathrm{k\text{-}1}}^{\mathrm{k\text{-}1}} \mathcal{A}_d^{\mathrm{T}} + \mathcal{N}_d, \tag{4-25}$$

with $\mathcal{N}_d$ being the product between half the sampling rate $N_s \delta t/2$ and the noise variance matrix. Notice that the *a priori* updates for the averages are already implictly defined by Eq. (4-22). The only adaptation we need to include in the aforementioned equation is to regard $\mathbf{x}_{\mathrm{k\text{-}1}}$ as the *a posteriori* estimate from the previous simulation step k-1, while $\mathbf{x}_{\mathrm{k}}$ is to be read as the *a priori* estimate of the current step k.

On the other hand, the *a posteriori* updates of the mean and covariance estimates are prescribed by the Kalman filter as follows. Define the Kalman gain matrix $\mathcal{K}_{\mathrm{k}}$ by,

$$\mathcal{K}_{\mathrm{k}} = \mathbf{\Sigma}_{\mathrm{k}}^{\mathrm{k\text{-}1}} \mathcal{C}^{\mathrm{T}} \left(R + \mathcal{C} \mathbf{\Sigma}_{\mathrm{k}}^{\mathrm{k\text{-}1}} \mathcal{C}^{\mathrm{T}} \right)^{-1}. \tag{4-26}$$

The estimate update for the averages is computed using $\mathcal{K}_k$ and the Kalman error ζ_k between the measurement y_k and the current *a priori* estimate,

$$\zeta_{\mathrm{k}} = y_{\mathrm{k}} - \mathcal{C}\hat{\mathbf{x}}_{\mathrm{k}}^{\mathrm{k\text{-}1}}, \tag{4-27}$$

$$\hat{\mathbf{x}}_{\mathrm{k}}^{\mathrm{k}} = \hat{\mathbf{x}}_{\mathrm{k}}^{\mathrm{k\text{-}1}} + \mathcal{K}_{\mathrm{k}} \zeta_{\mathrm{k}}. \tag{4-28}$$

While the estimate update for the covariance matrix reads,

$$\mathbf{\Sigma}_{\mathrm{k}}^{\mathrm{k}} = \left(\mathcal{I} - \mathcal{K}_{\mathrm{k}} C\right) \mathbf{\Sigma}_{\mathrm{k}}^{\mathrm{k\text{-}1}} \left(\mathcal{I} - \mathcal{K}_{\mathrm{k}} C\right)^{\mathrm{T}} + \mathcal{K}_{\mathrm{k}} R \mathcal{K}_{\mathrm{k}}^{\mathrm{T}}. \tag{4-29}$$

If we make $\mathbf{\Sigma}_{\mathrm{k}}^{\mathrm{k}} = \mathbf{\Sigma}_{\mathrm{k\text{-}1}}^{\mathrm{k\text{-}1}}$ using the relations for the *a priori* and *a posteriori* updates in Eq.s (4-25) and (4-29), we get the Riccatti equation satisfied by the steady-state covariance matrix $\mathbf{\Sigma}^{\mathrm{ss}}$,

$$\mathbf{\Sigma}^{\mathrm{ss}} = \mathcal{A}_d \mathbf{\Sigma}^{\mathrm{ss}} \mathcal{A}_d^{\mathrm{T}} + \mathcal{N}_d - \mathcal{A}_d \mathbf{\Sigma}^{\mathrm{ss}} \mathcal{C} \left(\mathcal{C}^{\mathrm{T}} \mathbf{\Sigma}^{\mathrm{ss}} \mathcal{C} + R \right)^{-1} \left(\mathcal{A}_d \mathbf{\Sigma}^{\mathrm{ss}} \mathcal{C} \right)^{\mathrm{T}} \tag{4-30}$$

The control law $u(t)$ is obtained from LQR theory, see, for instance, [144]. The idea is to minimize an objective function J, defined based on a user-defined cost matrix $\mathcal{Q}$ and a control effort which we parametrize using a feedback gain g_{fb},

$$J(u) = \lim_{N \to \infty} \left\langle \frac{1}{N} \sum_{k=0}^{N-1} (\mathbf{x}_k^T \mathcal{Q} \mathbf{x}_k + \left(\frac{\omega_m}{g_{fb}^2} \right) u_k^2) \right\rangle, \tag{4-31}$$

where in our examples we use an identity cost matrix, $\mathcal{Q} = (\omega_m/2)\mathcal{I}$. The control law that minimizes J given an estimate $\hat{\mathbf{x}}_k$ is [48],

$$u_k = -\mathbf{k}^{\mathrm{T}} \hat{\mathbf{x}}_k \tag{4-32}$$

Where the LQR gain $\mathbf{k}^{\mathrm{T}}$ is given by,

$$\mathbf{k}^{\mathrm{T}} = \left(\frac{\omega_m}{g_{fb}^2} + \mathbf{B}_d^{\mathrm{T}} \mathbf{\Omega}^{\mathrm{ss}} \mathbf{B}_d \right)^{-1} \mathbf{B}_d^{\mathrm{T}}, \tag{4-33}$$

and $\mathbf{\Omega}^{\mathrm{ss}}$ is obtained by solving the discrete algebraic Riccatti equation,

$$\mathbf{\Omega}^{\mathrm{ss}} = \mathcal{Q} + \mathcal{A}_d^{\mathrm{T}} \mathbf{\Omega}^{\mathrm{ss}} \mathcal{A}_d - \mathcal{A}_d^{\mathrm{T}} \mathbf{\Omega}^{\mathrm{ss}} \mathbf{B}_d \mathbf{k}^{\mathrm{T}}. \tag{4-34}$$

As customary, we denote the mechanical vibrational quanta from the estimated states as 'phonons', even though this may be regarded as an abuse of notation from solid state physics. In the case where the cavity is absent, we estimate the number of phonons $\langle \hat{n}_m \rangle$ as follows,

$$\begin{aligned} \langle \hat{n}_m \rangle + \frac{1}{2} \sim \frac{E_m}{\hbar \omega_m} &= \left\langle \frac{m \omega_m^2 Z^2}{2 \hbar \omega_m} + \frac{P^2}{2 \hbar m \omega_m} \right\rangle \\ \langle \hat{n}_m \rangle &\sim \frac{1}{4} \left\langle \frac{Z^2}{Z_{zpm}^2} + \frac{P^2}{P_{zpm}^2} \right\rangle - \frac{1}{2} \\ \langle \hat{n}_m \rangle &\sim \frac{1}{4} \left(\Delta \hat{Z}^2 + \hat{Z}^2 + \Delta \hat{P}^2 + \hat{P}^2 \right) - \frac{1}{2}, \end{aligned} \tag{4-35}$$

such that $\langle \hat{n}_m \rangle$ can be obtained from the estimates of the means $\mathbf{x}_k^k$ and from the trace of the estimated covariance matrix Σ_k^k. For the case where the cavity is present, an analogous definition can be performed for the vibrational quanta (photons, with an estimated number $\langle \hat{n}_\gamma \rangle$) in the optical quadrature components of the state estimates. In the results that follow, $\langle \hat{n} \rangle$ denotes $\langle \hat{n}_m \rangle$ in the mechanical-only case, and $\langle \hat{n}_m \rangle + \langle \hat{n}_\gamma \rangle$ in the cavity optomechanical case. In practice, we perform the computation of $\langle \hat{n} \rangle$ using moving window statistics.

The estimated variables are further decimated according to a controllable step, and we assume the resulting moving window means and variances to be representative of each timestamp window.

A final detail that needs to be mentioned is related to the initialization of the Kalman filter. One possible approach is to set the means to zero and the initial covariance matrix as large as possible [145], $\Sigma_0 = \epsilon\mathcal{I}$, with $\epsilon \to \infty$, representing complete distrust upon the initial mean estimate. We choose to initialize the Kalman algorithm with zero mean, but with Σ_0 given by $\sigma^2_{det}\mathcal{I}$. We have observed that this choice does not affect the performance of the estimator at long time scales.

Having laid out most of the ingredients for the numerical simulation, we dedicate the last section of this chapter to describing the results obtained when exploring this implementation. Weak optical impulses are input into the system and we use the Kalman estimates to analyze whether it is possible to characterize the system's response to those optical inputs.

4.3 Results

We begin this results section by benchmarking the Python environment we developed via the simulation of a cooling experiment in the absence of a cavity. We use parameters akin to those reported within [48] and verify whether we observe similar results. Fig. 4.2 shows a section of a simulation run, containing the simulated, measured and Kalman-estimated ($\hat{Z}$) position traces. p is set to 9.2×10^{-9} mbar, ω_m to $2\pi \times 104$ kHz, η to 34% and we use a feedback gain of $g_{fb} = 2\pi \times 110$ kHz, where the control step is set to 32 ns. We see that, given full knowledge of the dynamics and of the noise processes involved, the Kalman filter algorithm is able to output very precise state estimates from measurements which may appear, at a first glance, completely degenerated by noise.

In the left panel of Fig. 4.3 we show another short simulation trace containing the estimated position, with a shaded gray region representing the estimated position variance. The parameters used to generate Fig. 4.2 are maintained. Dashed lines indicate one of the moving windows used to calculate the estimated number of phonons of the state, with a length set to one period of the oscillator. In the right panel we plot the estimated number of phonons for each time window in this short simulation.

Next, in Fig. 4.4 we show simulated phase space trajectories for runs using the feedback gain values of $g_{fb} = 2\pi \times 110$ kHz and $g_{fb} = 2\pi \times 8.0$ kHz. The data is band passed at appropriate frequencies for smoothness. Histograms for

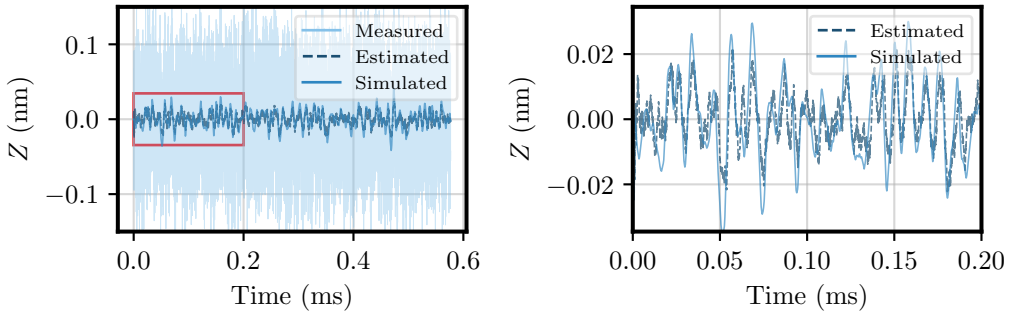

Figure 4.2: Simulation trace samples in the absence of a cavity. A simulation time of about 577 ms is displayed in the left panel, which contains the measured position in light blue, simulated and estimated traces. The right panel is a zoom-in within the region highlighted by the red rectangle. In it, the measured trace was left out for better visualization of how the simulated trace is followed by the Kalman estimate. A detection efficiency of 0.34 is considered, the oscillator's frequency is $\omega_m/2\pi = 104\,\text{kHz}$ and it is maintained under feedback cooling with a gain of $g_{fb} = 2\pi \times 110\,\text{kHz}$.

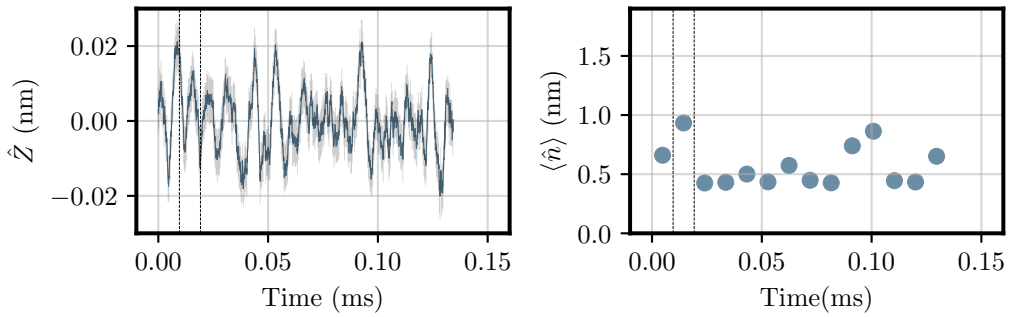

Figure 4.3: Estimated phonons in the absence of a cavity. In the left panel, a simulation trace containing the estimated position and a shaded gray region with the estimated position uncertainty. The dashed lines mark one of the time windows used to estimate the phonon numbers shown in the right panel as a function of time. We use the same parameters as those used for Fig. 4.2, and the time window width corresponds to one period of the oscillator's motion.

position and momentum are shown at each of the axes, and a circle representing zero point fluctuations is inserted in the figure, as well as the final number of phonons for each simulation run. Good qualitative compatibility with a similar analysis in [48] might indicate that the simulation is physical and that it behaves as expected. One of the only incompatibilities is with regards to the covariances of the phonon number estimates, which are hard to reproduce within our simulations. The numerical simulation's sensitivity to the value of

the feedback gain is also weak, provided that it is high enough to keep the oscillator under stable cooling. Nevertheless, if its value is too large or too low, we observe numerical overflow and the simulated traces diverge.

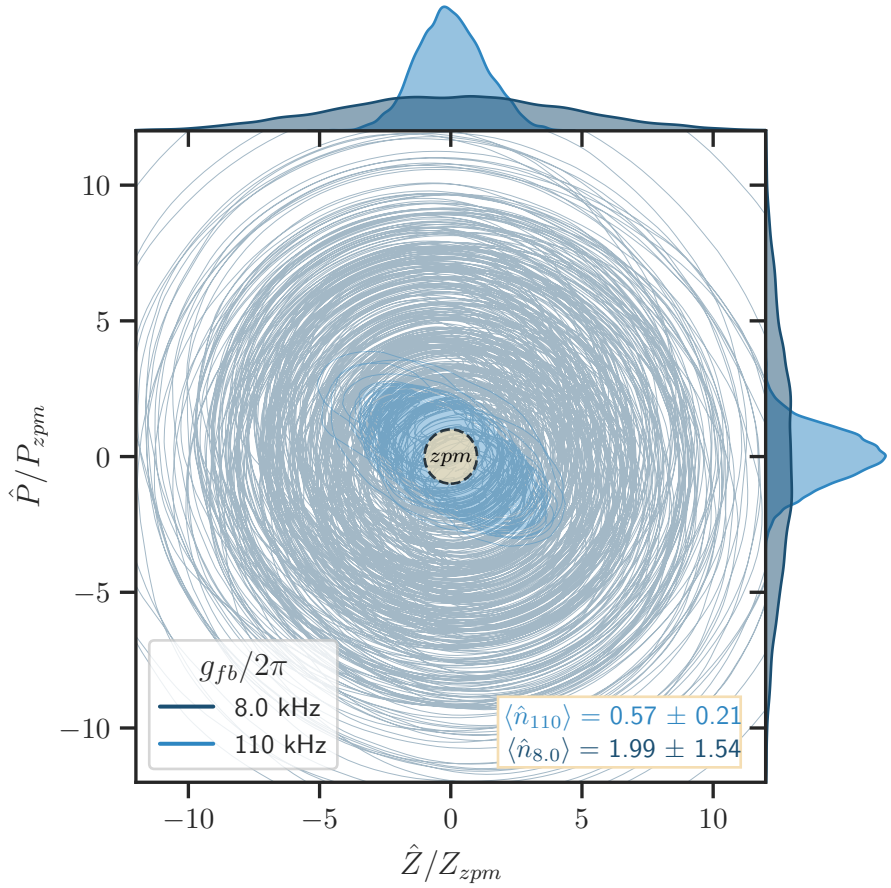

Figure 4.4: Simulated phase space trajectory. Estimated position and momentum are shown for two separate simulation traces, one where the feedback gain is given by $2\pi \times 8.0\,\text{kHz}$, corresponding to the trace with larger amplitude, and another with a feedback gain equal to $2\pi \times 110\,\text{kHz}$, closer to the center. A circle indicating the zero-point uncertainties is shown at the center of the figure, and the phonon number estimates are shown for each trace at the bottom right. Compare with the experimental result in [48].

Moving on to the introduction of a cavity around the oscillator, the simulation involves some new parameters, as indicated in the first section of this chapter. Namely, we introduce the cavity's detuning $\Delta = \omega_L - \omega_c$, linewidth κ and length L. Last but not least, we must also pick an optical pulse to be used as an input and to respect to which the system's response is evaluated. Maintaining the preservation of gaussianity presented by our system's dynamics requires the optical input states to also be gaussian. Thus, instead of using (non-gaussian) Fock states, which are associated with well defined numbers of

photons, all of our simulations are carried out using coherent optical states. A coherent state described by a complex eigenvalue α containing both its amplitude and phase satisfies,

$$X_{in} = \alpha^* + \alpha, \tag{4-36}$$

$$Y_{in} = i\left(\alpha^* - \alpha\right), \tag{4-37}$$

$$\langle n_{\gamma,\mathrm{in}} \rangle = \alpha^* \alpha, \tag{4-38}$$

where * represents complex conjugation. In what follows, we deal with zero-phase coherent states, and the following values for the newly introduced parameters have been picked: $\kappa = 1\,\mathrm{MHz}$, $\Delta = 0.3\omega_m$. The cavity length is set around 3 cm and corrected to the closest resonance at zero detuning.

We must also pick a temporal envelope shape for our optical input pulse. We have chosen a simple step-like optical pulse with start and end times denoted by t_{start} and t_{end}, respectively. The pulse is set to start at the timestamp at half the total simulation time (300 oscillator periods $\sim 2.88\,\mathrm{ms}$ are simulated) and to last $50\,\mu\mathrm{s}$.

Fig. 4.5 shows traces corresponding to such a simulation. The left panel presents a crop of the estimated state around the time where the step-like pulse is present, while the right panel shows the Kalman error δ_K corresponding to the difference between the estimated and the measured positions after each measurement step. The coherent input contains an average $\langle n_\gamma \rangle = 5$ photons. We see that, during the time window of the pulse, the Kalman error increases slightly. This can be interpreted as the internal model used for estimation not possessing knowledge about the input optical state, being thus unable to predict its interaction with the system. This enhancement of the Kalman error, associated with a discrepancy between expected and observed position averages, drives not only updates of the first moments, but also of the estimated covariances.

Given these covariance updates associated with an enhanced Kalman error, we suggest that perhaps the estimated number of quanta $\langle \hat{n} \rangle$ as a function of time can be used to evaluate the system's response to the optical input. Fig. 4.6 shows a crop of the simulation in the same window as the one shown before, but the quantity plotted is the estimated number of quanta $\langle \hat{n} \rangle$. We quantify this response to the optical input by defining an SNR: given a chosen metric ($\hat{Z}$ or $\langle \hat{n} \rangle$), a reference window prior to the introduction of the pulse is defined and used to compute a background root mean square (RMS) of the signal. The SNR is then calculated as the ratio between the signal RMS within the pulse time window (shaded in green in the Figure) and the calculated reference

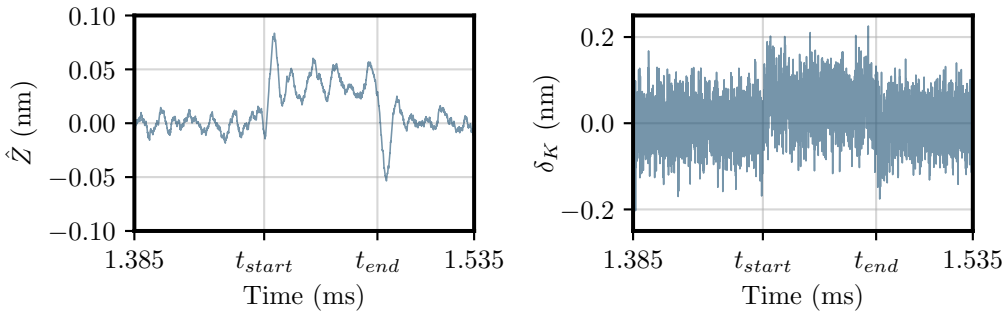

Figure 4.5: Simulation trace samples in the presence of a cavity. The left panel shows the estimated position for visualization of the system's response to a step-like coherent pulse containing $\langle n_\gamma \rangle = 5$ photons and with a duration of 60 μs. The right panel shows the associated Kalman error δ_K, which is calculated using the difference between estimated and measured position at each timestamp. The increase of δ_K around the time of the pulse, associated with the lack of knowledge with respect to the optical input, drives updates not only of the mean estimates, but also of the covariance estimates.

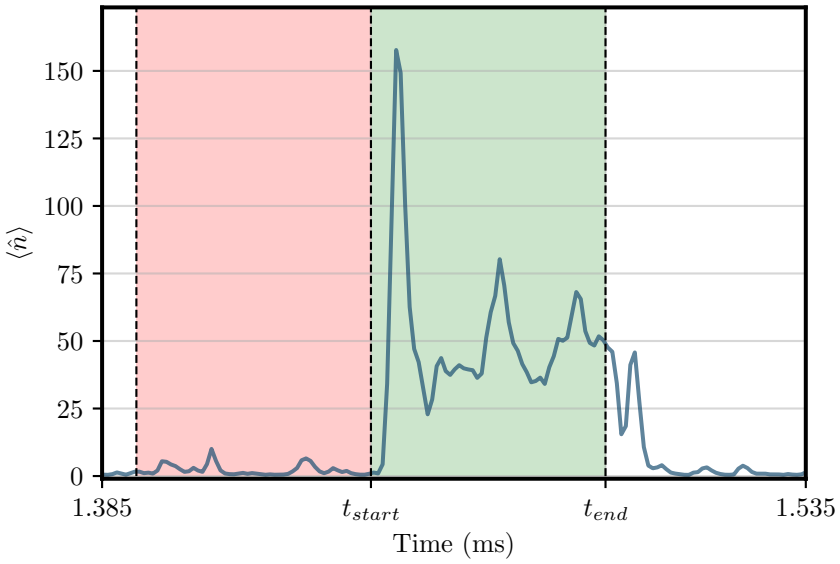

Figure 4.6: Estimated number of quanta and SNR illustration. We show the response of the system to a pulse containing $\langle n_\gamma \rangle = 5$ photons between t_{start} and t_{end}. The green-shaded area represents the window where we measure our signal, whilst the red-shaded area indicates the reference for calculating the signal-to-noise ratio. The SNR is given by the squared ratio between the RMS of the signal and of the reference. We have set the width of the moving average for phonon computation to a tenth of the oscillator's period, for improvement of visualization.

(shaded in red). We choose to crop a reference window having the same width as the pulse, although this is not strictly necessary. For this trace in particular, the SNR obtained from $\langle\hat{n}\rangle$ is of about $\mathrm{SNR}_{\langle\hat{n}\rangle} \approx 26\,\mathrm{dB}$, while a correspondent calculation yields $\mathrm{SNR}_{\hat{Z}} \approx 14\,\mathrm{dB}$ if we use the position as a metric. The higher SNR of the system's response to the pulse when we inspect $\langle\hat{n}\rangle$ instead of $\hat{Z}$ may be interpreted as being due to the usage of information not only from the averages, but also from the covariance estimates.

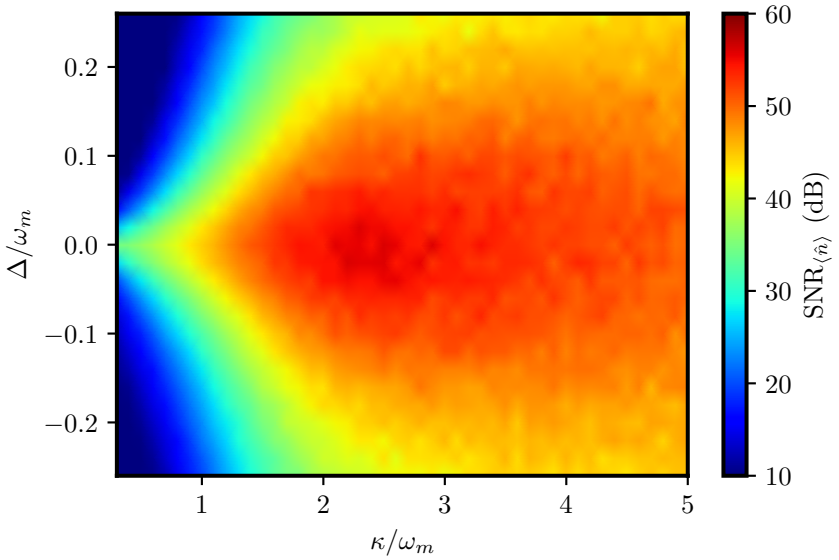

Figure 4.7: SNR as a function of cavity linewidth and detuning. Each (κ, Δ) pair is associated with ten simulation runs. We quantify the system's response to the optical input using the SNR of the estimated number of quanta within the pulse window, and each point on the colormap shows the average result over all runs.

The colormap presented by Fig. 4.7 shows the computed $\mathrm{SNR}_{\langle\hat{n}\rangle}$ for different simulation parameters. Aside from Δ and κ, evaluation of the system's response is made using the same parameters as previously, including the pulse duration of $50\,\mu$s and an average optical input photon number of five. For improved smoothness of the data, each point is an average of ten simulation runs. Due to the cavity resonance, the expected signal enhancement around zero detuning is observed. A nonmonotonic behavior of the system's response to the pulse as a function of cavity linewidth is observed. $\mathrm{SNR}_{\langle\hat{n}\rangle}$ increases steadily with κ until about $\kappa \approx 2.3\omega_m$, and decreases for higher values. This nonmonotonic behavior can be intuitively justified after inspection of Eq.s (4-1) and (4-6): the dynamics of the quadratures are influenced by the optical input amplitude proportionally to $\sqrt{\kappa}$, whilst the cavity's finesse decreases with the inverse of the linewidth. The cavity's finesse, in its turn, affects the

system's response nontrivially via the effective amplification factor, which at zero detuning increases with $\mathcal{F}$. From these opposite influences we could expect the appearance of a local maximum in parameter space.

Fig. 4.8 shows the computed $\mathrm{SNR}_{\langle\hat{n}\rangle}$ as a function of mean photon number within the optical pulse, with $\kappa = 2\omega_m$ and for the detuning values of $\Delta = \omega_m/5$ and $\Delta = \omega_m$ for the left and right columns, respectively. The bottom panels show zoomed-in data within the region up to $\langle n_\gamma \rangle = 10$ photons. For the almost optimal conditions associated with the left column, we observe that the presence of optical input pulses containing average photon numbers down to $\langle n_\gamma \rangle = 0.1$ can be inferred from the estimated states. This indicates that the system has potential applications as a detector for single photons, at least in terms of its sensitivity to external optical inputs.

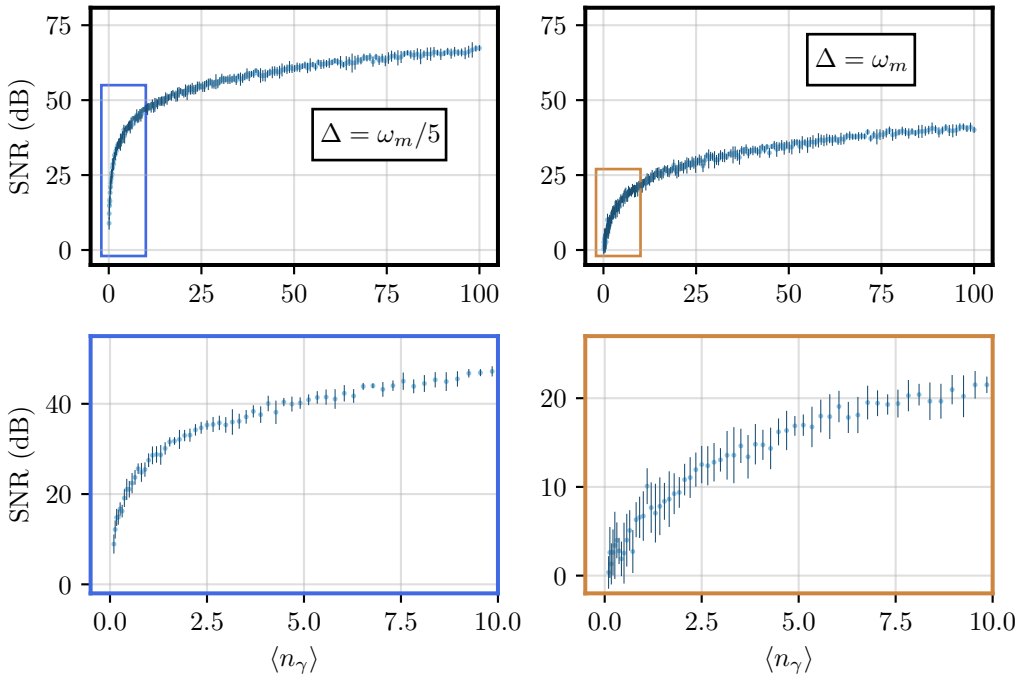

Figure 4.8: SNR as a function of input photon number. Setting a linewidth of $\kappa = 2\omega_m$, we inspect the system's response to optical pulses with different intensities. The left and right panels consider a detuning of $\Delta = \omega_m/5$ and $\Delta = \omega_m$, respectively. The bottom panels zoom into the regions highlighted by the blue and orange rectangles in the top panels. We see that optical pulses with intensities corresponding to average photon numbers down to $\langle n_\gamma \rangle = 0.1$ can be sensed by the system in the (almost) best case scenario.

Let us wrap this chapter up with a qualitative sanity check of our simulation efforts. As already described, the coherent scattering hamiltonian is of the form,

$$H/\hbar = gZX, \tag{4-39}$$

and let us denote position by $Q = Z_{zpm}Z$, in consistency with the definitions at the beginning of the chapter. An estimate of the force caused by a cavity electromagnetic state upon the particle can be obtained by,

$$e^{\frac{-i}{\hbar}H\delta t} \sim e^{-igZX\delta t} \sim e^{-i\frac{g\hbar}{Z_{zpm}}X\delta t\frac{Q}{\hbar}} \sim e^{-i\delta p\, Q/\hbar}. \tag{4-40}$$

From the last two expressions we get an estimate of the force,

$$F \sim \frac{\delta p}{\delta t} \sim \frac{g\hbar}{Z_{zpm}}X. \tag{4-41}$$

Considering a short pulse containing an average 2000 photons, we could estimate an associated displacement ΔQ in the harmonic approximation,

$$\Delta Q = \frac{F}{m\omega_m^2} = 1.46\,\text{nm} \sim \mathcal{O}(1\,\text{nm}). \tag{4-42}$$

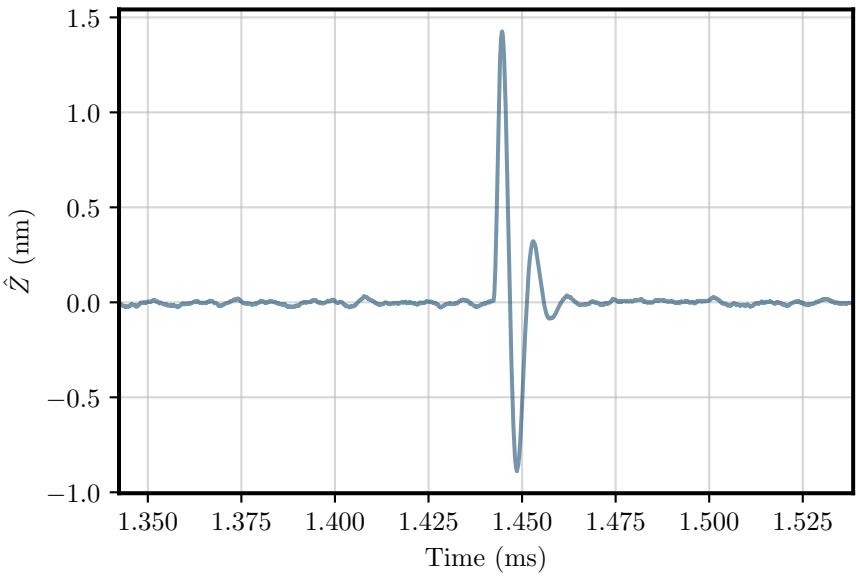

Figure 4.9: Verification of amplitude estimate. We introduce a short pulse with a duration of $1.0\,\mu$s and an average 2000 photons to our system and plot the estimated position trace in a time window around the center of the pulse. A detuning of $\Delta = \omega_m/5$ and a cavity linewidth of $\kappa = 2\omega_m$ were used in this example.

We test this estimate within our simulation using a short pulse lasting $1.0\,\mu$s and verify the observed amplitude. The pulse is defined as "short" with respect to the other relevant time scales in our problem. Were the pulse too

long, the approximations previously introduced would likely start to fail. A detuning of $\Delta = \omega_m/5$ and a cavity linewidth of $\kappa = 2\omega_m$ were used, and the estimated position trace is shown in Fig. 4.9. We see that the estimate obtained in Eq. (4-42) is very well followed, which reinforces the thought that our simulation lies on physical grounds.

5
Outlook

In this work, we have implemented the collection of backscattered light from an optical tweezer for improved cooling of CoM motion along the optical axis. This enhanced efficiency was used to improve previous cooling results along the longitudinal direction. A demand for two immediate improvements can be formulated. The investigation of the low calibration factors along the transversal directions is a natural next step, as well as the improvement of the interferometer's stability for backward detection. Solving the issue regarding the transversal directions will allow us to perform 3D-cooling in an improved way, making the trap more stable at lower pressures. Improving the stability of the interferometer might not necessarily lead to much higher detection efficiencies in the longitudinal direction. Nevertheless, it will allow us to reliably perform experiments during time spans longer than a few hours without having to constantly rerun the calibration protocol for both the detector and the z-electrodes. This is relevant since high vacuum environments demand pump-down times ranging from many hours to a few days. Thus, performing experiments at these conditions is a goal which naturally requires troubleshooting drifts with magnitudes such as those presently observed in our setup. Some other directions for experimental implementation can be envisioned for the near future as well. First, higher detection efficiencies along the transversal directions can be achieved by using a collection lens with the same NA as the trapping lens [51]. Second, implementation of heterodyne detection will provide us with absolute measurements of effective temperatures of the motion along each degree of freedom [45]. Independence between this absolute temperature measurement and the calibration of the detectors will improve precision and reliability of effective temperature estimates. Third, state estimation using an FPGA-implemented Kalman filter algorithm will yield optimal estimation of both position and velocity of the particle along each axis. This might enhance our system's robustness to measurement noise and possibly the outcomes of our cooling endeavors [48]. Lastly, we are working on implementing an ionic pumping system in order to lower the minimal vacuum pressures down to $\sim 10^{-11}$ mbar, consequently improving the lowest temperatures which can be potentially achieved in our cooling experiments, opening the way to ground

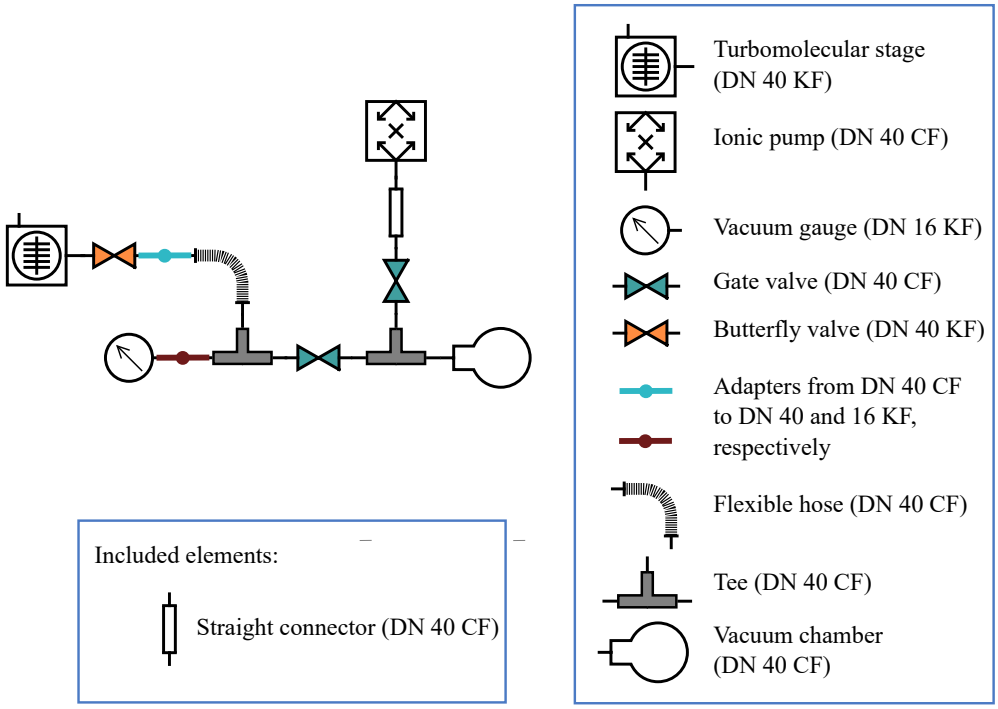

Figure 5.1: Future vacuum system. In the near future, an ionic pumping system will be appended to the system. Flanges will be replaced by their knife-edge sealed counterparts wherever possible, and gate valves will control restriction of the pumped volume when the turbomolecular stage reaches its final pressure levels. A rough schematic of the planned scheme is shown, with a symbol caption to the right, including flange standards wherever applicable. The straight connector was included because we have verified the possibility of a bulge from the design of the ionic pump being incompatible with the gate valve chosen.

state cooling and to the marvelous possibilities thereby attainable [23, 54]. A schematic of the vacuum system we plan on assembling is displayed in Fig. 5.1.

Our simulation efforts can also be further refined, for instance, via inclusion of phase and amplitude noises of both the "calibration" and tweezing beams. One possible line of further investigation is phase measurement of the input coherent state, in a state tomography fashion. Other directions include looking for better definitions of what does it mean to detect an optical input in the context of the optomechanical simulations. This could naturally lead to analyzing dead times, dark counts and the system's response to the introduction of multiple pulses.

Bibliography

[1] K. Svoboda, C. F. Schmidt, B. J. Schnapp, and S. M. Block, "Direct observation of kinesin stepping by optical trapping interferometry," *Nature*, vol. 365, pp. 721–727, 1993.

[2] J. Finer and J. A. Spudich, "Single myosin molecule mechanics: piconewton forces and nanometre steps," *Nature*, vol. 368, 1994.

[3] J. Jiao, A. A. Rebane, L. Ma, and Y. Zhang, "Single-molecule protein folding experiments using high precision optical tweezers," *Methods in Molecular Biology*, vol. 1486, pp. 357–390, 2017.

[4] C. J. Bustamante, Y. R. Chemla, S. Liu, and M. D. Wang, "Optical tweezers in single-molecule biophysics," *Nature Reviews Methods Primers*, vol. 1, no. 25, pp. 1–29, 2021.

[5] C. Bustamante and S. Yan, "The development of single molecule force spectroscopy: from polymer biophysics to molecular machines," *Quarterly Reviews of Biophysics*, vol. 55, pp. 1–42, 2022.

[6] J. Gieseler, R. Quidant, C. Dellago, and L. Novotny, "Dynamic relaxation of a levitated nanoparticle from a non-equilibrium steady state," *Nature Nanotechnology*, vol. 9, pp. 358–364, 2014.

[7] J. Millen, T. Deesuwan, P. Barker, and J. Anders, "Nanoscale temperature measurements using non-equilibrium brownian dynamics of a levitated nanosphere," *Nature nanotechnology*, vol. 9, no. 6, pp. 425–429, 2014.

[8] F. Ricci, R. A. Rica, M. Spasenović, J. Gieseler, L. Rondin, L. Novotny, and R. Quidant, "Optically levitated nanoparticle as a model system for stochastic bistable dynamics," *Nature communications*, vol. 8, no. 1, p. 15141, 2017.

[9] R. M. Pettit, W. Ge, P. Kumar, D. R. Luntz-Martin, J. T. Schultz, L. P. Neukirch, M. Bhattacharya, and A. N. Vamivakas, "An optical tweezer phonon laser," *Nature Photonics*, vol. 13, pp. 402–405, 2019.

[10] L. Ornigotti and R. Filip, "Stroboscopic thermally-driven mechanical motion," *Scientific Reports*, vol. 12, no. 20091, 2022.

[11] L. P. Ghislain and W. W. Webb, "Scanning-force microscope based on an optical trap," *Optics Letters*, vol. 18, no. 19, pp. 1678–1680, 1993.

[12] J. H. G. Huisstede, K. O. van der Werf, M. L. Bennink, and V. Subramaniam, "Force detection in optical tweezers using backscattered light," *Optics Express*, vol. 13, no. 4, pp. 1113–1123, 2005.

[13] F. Monteiro, S. Ghosh, A. G. Fine, and D. C. Moore, "Optical levitation of 10-ng spheres with nano-g acceleration sensitivity," *Physical Review A*, vol. 96, no. 6, p. 063841, 2017.

[14] G. Winstone, R. Bennett, M. Rademacher, M. Rashid, S. Buhmann, and H. Ulbricht, "Direct measurement of the electrostatic image force of a levitated charged nanoparticle close to a surface," *Physical Review A*, no. 98, p. 053831, 2018.

[15] C. P. Blakemore, A. D. Rider, S. Roy, Q. Wang, A. Kawasaki, and G. Gratta, "Three-dimensional force-field microscopy with optically levitated microspheres," *Physical Review A*, vol. 99, p. 023816, 2019.

[16] C. Montoya, E. Alejandro, W. Eom, D. Grass, N. Clarisse, A. Witherspoon, and A. A. Geraci, "Scanning force sensing at micrometer distances from a conductive surface with nanospheres in an optical lattice," *Applied optics*, vol. 61, no. 12, pp. 3486–3493, 2022.

[17] F. Ricci, M. T. Cuairan, A. W. Schell, E. Hebestreit, R. A. Rica, N. Meyer, and R. Quidant, "A chemical nanoreactor based on a levitated nanoparticle in vacuum," *ACS nano*, vol. 16, no. 6, pp. 8677–8683, 2022.

[18] T. Agrenius, C. Gonzalez-Ballestero, P. Maurer, and O. Romero-Isart, "Interaction between an optically levitated nanoparticle and its thermal image: internal thermometry via displacement sensing," *Physical Review Letters*, vol. 130, p. 093601, 2023.

[19] K. Levi, A. Giat, L. Golan, E. Talker, and L. Stern, "Remote chip-scale quantum sensing of magnetic fields," *arXiv preprint arXiv:2307.06130*, 2023.

[20] T. Liang, S. Zhu, P. He, Z. Chen, Y. Wang, C. Li, Z. Fu, X. Gao, X. Chen, N. Li, Q. Zhu, and H. Hu, "Yoctonewton force detection based on optically levitated oscillator," *Fundamental Research*, vol. 3, pp. 57–62, 2023.

[21] J. Gosling, A. Pontin, J. Iacoponi, P. Barker, and T. Monteiro, "Sensing directional noise baths in levitated optomechanics," *Physical Review Research*, vol. 6, no. 1, p. 013129, 2024.

[22] L. Martinetz, K. Hornberger, J. Millen, M. Kim, and B. A. Stickler, "Quantum electromechanics with levitated nanoparticles," *Nature Portfolio journals*, vol. 6, no. 101, 2020.

[23] M. Rademacher, J. Millen, and Y. L. Li, "Quantum sensing with nanoparticles for gravimetry: when bigger is better," *Advanced Optical Technologies*, vol. 9, no. 5, pp. 227–239, 2020.

[24] H. Rudolph, K. Hornberger, and B. A. Stickler, "Entangling levitated nanoparticles by coherent scattering," *Physical Review A*, vol. 101, p. 011804, 2020.

[25] G. Winstone, Z. Wang, S. Klomp, G. R. Felsted, A. Laeuger, C. Gupta, D. Grass, N. Aggarwal, J. Sprague, P. J. Pauzauskie, S. L. Larson, V. Kalogera, and A. A. Geraci, "Optical trapping of high-aspect-ratio NaYF hexagonal prisms for khz-mhz gravitational wave detectors," *Physical Review Letters*, vol. 129, no. 5, p. 053604, 2022.

[26] D. Carney, K. G. Leach, and D. C. Moore, "Searches for massive neutrinos with mechanical quantum sensors," *PRX Quantum*, vol. 4, p. 010315, 2023.

[27] M. Roda-Llordes, D. Candoli, P. T. Grochowski, A. Riera-Campeny, T. Agrenius, J. J. García-Ripoll, C. Gonzalez-Ballestero, and O. Romero-Isart, "Numerical simulation of large-scale nonlinear open quantum mechanics," *Physical Review Research*, vol. 6, p. 013262, 2024.

[28] E. Bonvin, L. Devaud, M. Rossi, A. Militaru, L. Dania, D. S. Bykov, O. Romero-Isart, T. E. Northup, L. Novotny, and M. Frimmer, "State expansion of a levitated nanoparticle in a dark harmonic potential," *Physical Review Letters*, vol. 132, p. 253602, 2024.

[29] B. F. A. d. Melo, "Tweezers and cavities: developing tools for an optomechanics laboratory," Master's thesis, Pontifícia Universidade Católica do Rio de Janeiro, 2019.

[30] I. B. C. Moreira, "Harnessing optomechanical interactions: from trapping organisms to entangling nanospheres," Master's thesis, Pontifícia Universidade Católica do Rio de Janeiro, 2019.

[31] F. A. d. Silva, "Optical tweezers and structured light: trapping microparticles in a dark focus," Master's thesis, Pontifícia Universidade Católica do Rio de Janeiro, 2023.

[32] O. S. Kremer, "Feedback control of optically levitated nanoparticles," Master's thesis, Pontifícia Universidade Católica do Rio de Janeiro, 2024.

[33] B. d. M. Calderoni, "Levitated optomechanics: from gaussian tweezers to structured modes," Master's thesis, Pontifícia Universidade Católica do Rio de Janeiro, 2024.

[34] M. D. Eisaman, J. Fan, M. A, and P. S. V, "Single-photon sources and detectors," *Review of Scientific Instruments*, vol. 82, p. 071101, 2011.

[35] S. D. Russo, A. Elefante, D. Dequal, D. K. Pallotti, L. S. Amato, F. Sgobba, and M. S. d. Cumis, "Advances in mid-infrared single-photon detection," *Photonics*, vol. 9, no. 470, 2022.

[36] R. H. Hadfied, J. Leach, F. Fleming, D. J. Paul, C. H. Tan, J. S. Ng, R. K. Henderson, and G. S. Buller, "Single-photon detection for long-range imaging and sensing," *Optica*, vol. 10, no. 9, pp. 1124–1141, 2023.

[37] I. E. Zadeh, J. W. N. Los, R. B. M. Gourgues, V. Steinmetz, G. Bulgarini, S. M. Dobrovolskiy, V. Zwiller, and S. N. Dorenbos, "Single-photon detectors combining high efficiency, high detection rates, and ultra-high timing resolution," *APL Photonics*, vol. 2, no. 11, p. 111301, 2017.

[38] B. N. Datta, *Numerical methods for linear control systems*. Elsevier, 2004.

[39] P. Wen, M. Wang, and G.-L. Long, "Ground-state cooling in cavity optomechanical systems," *Frontiers in Physics*, vol. 11, 2023.

[40] P. Gonzalez-Ballestero, Maurer, D. Windey, L. Novotny, R. Reimann, and O. Romero-Isart, "Theory for cavity cooling of levitated nanoparticles via coherent scattering: Master equation approach," *Physical Review A*, vol. 100, no. 1, p. 013805, 2019.

[41] U. Delić, M. Reisenbauer, K. Dare, D. Grass, V. Vuletić, N. Kiesel, and M. Aspelmeyer, "Cooling of a levitated nanoparticle to the motional quantum ground state," *Science*, vol. 367, no. 6480, pp. 892–895, 2020.

[42] T. Penny, A. Pontin, and P. Barker, "Performance and limits of feedback cooling methods for levitated oscillators: a direct comparison," *Physical Review A*, vol. 104, p. 023502, 2021.

[43] S. K. Manikandan and S. Qvarfort, "Optimal quantum parametric feedback cooling," *Physical Review A*, vol. 107, p. 023516, 2023.

[44] A. Ghosh, P. Kumar, C. Sommer, F. G. Jimenez, V. Sudhir, and C. Genes, "Theory of phase-adaptive parametric cooling," *Physical Review A*, vol. 107, no. 5, p. 053521, 2023.

[45] F. Tebbenjohanns, M. L. Mattana, M. Rossi, M. Frimmer, and L. Novotny, "Quantum control of a nanoparticle optically levitated in cryogenic free space," *Nature*, vol. 595, no. 7867, pp. 378–382, 2021.

[46] D. Goldwater, B. A. Stickler, L. Martinetz, T. E. Northup, K. Hornberger, and J. Millen, "Levitated electromechanics: all-electrical cooling of charged nano-and micro-particles," *Quantum Science and Technology*, vol. 4, no. 2, p. 024003, 2019.

[47] V. Liška, T. Zemánková, V. Svak, P. Jákl, J. Ježek, M. Bránecký, S. H. Simpson, P. Zemánek, and O. Brzobohatý, "Cold damping of levitated optically coupled nanoparticles," *Optica*, vol. 10, no. 9, pp. 1203–1209, 2023.

[48] L. Magrini, P. Rosenzweig, C. Bach, A. Deutschmann-Olek, S. G. Hofer, S. Hong, N. Kiesel, A. Kugi, and M. Aspelmeyer, "Real-time optimal quantum control of mechanical motion at room temperature," *Nature*, vol. 595, no. 7867, pp. 373–377, 2021.

[49] J. Vijayan, Z. Zhang, J. Piotrowski, D. Windey, F. van der Laan, M. Frimmer, and L. Novotny, "Scalable all-optical cold damping of levitated nanoparticles," *Nature Nanotechnology*, vol. 18, no. 1, pp. 49–54, 2023.

[50] M. Iwasaki, T. Yotsuya, T. Naruki, Y. Matsuda, M. Yoneda, and K. Aikawa, "Electric feedback cooling of single charged nanoparticles in an optical trap," *Physical Review A*, 2019.

[51] F. Tebbenjohanns, M. Frimmer, and L. Novotny, "Optimal position detection of a dipolar scatterer in a focused field," *Physical Review A*, vol. 100, no. 4, p. 043821, 2019.

[52] A. Rohrbach and E. H. K. Stelzer, "Three-dimensional position detection of optically trapped dielectric particles," *Journal of Applied Physics*, vol. 91, no. 8, pp. 5474–5488, 2002.

[53] G. Volpe, G. Kozyreff, and D. Petrov, "Backscattering position detection for photonic force microscopy," *Journal of Applied Physics*, p. 084701, 2007.

[54] M. Aspelmeyer, T. J. Kippenberg, and F. Marquardt, "Cavity optomechanics," *Reviews of Modern Physics*, vol. 86, no. 4, 2014.

[55] O. Kremer, D. Tandeitnik, R. Mufato, I. Califrer, B. Calderoni, F. Calliari, B. Melo, G. Temporão, and T. Guerreiro, "Perturbative nonlinear feedback forces for optical levitation experiments," *Physical Review A*, vol. 109, p. 023521, 2024.

[56] B. Suassuna, B. Melo, and T. Guerreiro, "Path integrals and nonlinear optical tweezers," *Physical Review A*, vol. 103, no. 1, p. 013110, 2021.

[57] J. Millen, T. S. Monteiro, R. Pettit, and A. N. Vamivakas, "Optomechanics with levitated particles," *Reports on Progress in Physics*, vol. 83, no. 2, p. 026401, 2020.

[58] C. Gonzalez-Ballestero, M. Aspelmeyer, L. Novotny, R. Quidant, and O. Romero-Isart, "Levitodynamics: Levitation and control of microscopic objects in vacuum," *Science*, vol. 374, no. 6564, p. eabg3027, 2021.

[59] J. Gieseler and J. Millen, "Levitated nanoparticles for microscopic thermodynamics—a review," *Entropy*, vol. 20, no. 5, p. 326, 2018.

[60] V. Svak, J. Flajšmanová, L. Chvátal, M. Šiler, A. Jonáš, J. Ježek, S. H. Simpson, P. Zemánek, and O. Brzobohatý, "Stochastic dynamics of optically bound matter levitated in vacuum," *Optica*, vol. 8, no. 2, 2021.

[61] J. Sheng, C. Yang, and H. Wu, "Nonequilibrium thermodynamics in cavity optomechanics," *Fundamental Research*, vol. 3, no. 1, pp. 75–86, 2023.

[62] O. Romero-Isart, A. C. Pflanzer, F. Blaser, R. Kaltenbaek, N. Kiesel, M. Aspelmeyer, and J. I. Cirac, "Large quantum superpositions and interference of massive nanometer-sized objects," *Physical review letters*, vol. 107, no. 2, p. 020405, 2011.

[63] G. Gasbarri, A. Belenchia, M. Carlesso, S. Donadi, A. Bassi, R. Kaltenbaek, M. Paternostro, and H. Ulbricht, "Testing the foundation of quantum physics in space via interferometric and non-interferometric experiments with mesoscopic nanoparticles," *Communication Physics*, vol. 4, no. 155, 2021.

[64] P. H. Jones, O. M. Maragò, and G. Volpe, *Optical tweezers: Principles and applications*. Cambridge University Press, 2015.

[65] J. Gieseler, J. R. Gomez-Solano, A. Magazzù, I. P. Castillo, L. P. García, M. Gironella-Torrent, X. Viader-Godoy, F. Ritort, G. Pesce, A. V. Arzola *et al.*, "Optical tweezers—from calibration to applications: a tutorial," *Advances in Optics and Photonics*, vol. 13, no. 1, pp. 74–241, 2021.

[66] E. Hebestreit, M. Frimmer, R. Reimann, C. Dellago, F. Ricci, and L. Novotny, "Calibration and energy measurement of optically levitated nanoparticle sensors," *Review of Scientific Instruments*, vol. 89, no. 3, 2018.

[67] L. A. Defaveri, S. M. D. Queirós, and W. A. Morgado, "Dependence of efficiency on the nonlinear nature of a nanomachine," *Physical Review E*, vol. 98, no. 6, p. 062106, 2018.

[68] L. A. C. A. Defaveri, W. A. M. Morgado, and S. M. D. Queirós, "Power output for a nonlinear brownian machine," *Physical Review E*, vol. 96, no. 052115, 2017.

[69] F. Albarelli, A. Ferraro, M. Paternostro, and M. G. Paris, "Nonlinearity as a resource for nonclassicality in anharmonic systems," *Physical Review A*, vol. 93, no. 3, p. 032112, 2016.

[70] L. Neumeier, M. A. Ciampini, O. Romero-Isart, M. Aspelmeyer, and N. Kiesel, "Fast quantum interference of a nanoparticle via optical potential control," *Proceedings of the National Academy of Sciences*, vol. 121, no. 4, p. e2306953121, 2024.

[71] Y. Yang, Y.-X. Ren, M. Chen, Y. Arita, and C. Rosales-Guzmán, "Optical trapping with structured light: a review," *Advanced Photonics*, vol. 3, no. 3, pp. 034 001–034 001, 2021.

[72] L. Rondin, J. Gieseler, F. Ricci, R. Quidant, C. Dellago, and L. Novotny, "Direct measurement of kramers turnover with a levitated nanoparticle," *Nature nanotechnology*, vol. 12, no. 12, pp. 1130–1133, 2017.

[73] Y. Zhang, J. Shen, C. Min, Y. Jin, Y. Jiang, J. Liu, S. Zhu, Y. Sheng, A. V. Zayats, and X. Yuan, "Nonlinearity-induced multiplexed optical trapping and manipulation with femtosecond vector beams," *Nano Letters*, vol. 18, no. 9, pp. 5538–5543, 2017.

[74] M. A. Ciampini, T. Wenzl, M. Konopik, E. Lutz, G. Thalhammer, M. Ritsch-Marte, M. Aspelmeyer, and N. Kiesel, "Non-equilibrium memories with levitated nanoparticles: experimental verification of

the generalised landauer's principle," in *Optical Trapping and Optical Micromanipulation XVII*, vol. 11463. SPIE, 2020, p. 114631N.

[75] B. P. da Silva, V. Pinillos, D. Tasca, L. Oxman, and A. Khoury, "Pattern revivals from fractional gouy phases in structured light," *Physical review letters*, vol. 124, no. 3, p. 033902, 2020.

[76] H. Moradi, V. Shahabadi, E. Madadi, E. Karimi, and F. Hajizadeh, "Efficient optical trapping with cylindrical vector beams," *Optics express*, vol. 27, no. 5, pp. 7266–7276, 2019.

[77] B. Melo, I. Brandão, R. Rodrigues, A. Khoury, T. Guerreiro *et al.*, "Optical trapping in a dark focus," *Physical Review Applied*, vol. 14, no. 3, p. 034069, 2020.

[78] F. Almeida, I. Sousa, O. Kremer, B. P. da Silva, D. S. Tasca, A. Z. Khoury, G. Temporão, and T. Guerreiro, "Trapping microparticles in a structured dark focus," *Phys. Rev. Lett.*, vol. 131, p. 163601, Oct 2023.

[79] C. C. Chow and M. A. Buice, "Path integral methods for stochastic differential equations," *The Journal of Mathematical Neuroscience (JMN)*, vol. 5, pp. 1–35, 2015.

[80] J. Gieseler, L. Novotny, and R. Quidant, "Thermal nonlinearities in a nanomechanical oscillator," *Nature physics*, vol. 9, no. 12, pp. 806–810, 2013.

[81] M. T. Cuairan, J. Gieseler, N. Meyer, and R. Quidant, "Precision calibration of the duffing oscillator with phase control," *Physical Review Letters*, vol. 128, no. 21, p. 213601, 2022.

[82] M. Innerbichler, A. Militaru, M. Frimmer, L. Novotny, and C. Dellago, "White-noise fluctuation theorem for langevin dynamics," *New Journal of Physics*, vol. 24, no. 11, p. 113028, 2022.

[83] F. Tebbenjohanns, M. Frimmer, A. Militaru, V. Jain, and L. Novotny, "Cold damping of an optically levitated nanoparticle to microkelvin temperatures," *Physical review letters*, vol. 122, no. 22, p. 223601, 2019.

[84] G. P. Conangla, F. Ricci, M. T. Cuairan, A. W. Schell, N. Meyer, and R. Quidant, "Optimal feedback cooling of a charged levitated nanoparticle with adaptive control," *Physical review letters*, vol. 122, no. 22, p. 223602, 2019.

[85] N. Bullier, A. Pontin, and P. Barker, "Quadratic optomechanical cooling of a cavity-levitated nanosphere," *Physical Review Research*, vol. 3, no. 3, p. L032022, 2021.

[86] S. Lloyd and J.-J. E. Slotine, "Quantum feedback with weak measurements," *Physical Review A*, vol. 62, no. 1, p. 012307, 2000.

[87] J. Bateman, S. Nimmrichter, K. Hornberger, and H. Ulbricht, "Near-field interferometry of a free-falling nanoparticle from a point-like source," *Nature communications*, vol. 5, no. 1, p. 4788, 2014.

[88] O. Kremer, I. Califrer, D. Tandeitnik, J. P. von der Weid, G. Temporão, and T. Guerreiro, "All electrical cooling of an optically levitated nanoparticle," *Physical Review A*, 2024.

[89] A. Ashkin, J. M. Dziedzic, J. E. Bjorkholm, and S. Chu, "Observation of a single-beam gradient force optical trap for dielectric particles," *Optics letters*, vol. 11, no. 5, pp. 288–290, 1986.

[90] W. Paul, "Electromagnetic traps for charged and neutral particles," *Reviews of modern physics*, vol. 62, no. 3, p. 531, 1990.

[91] L. Dania, D. S. Bykov, M. Knoll, P. Mestres, and T. E. Northup, "Optical and electrical feedback cooling of a silica nanoparticle levitated in a paul trap," *Physical Review Research*, vol. 3, no. 1, p. 013018, 2021.

[92] D. S. Bykov, M. Meusburger, L. Dania, and T. E. Northup, "Hybrid electro-optical trap for experiments with levitated particles in vacuum," *Review of Scientific Instruments*, vol. 93, no. 7, p. 073201, 2022.

[93] D. Hempston, J. Vovrosh, M. Toroš, G. Winstone, M. Rashid, and H. Ulbricht, "Force sensing with an optically levitated charged nanoparticle," *Applied Physics Letters*, vol. 111, no. 13, 2017.

[94] G. Ranjit, M. Cunningham, K. Casey, and A. A. Geraci, "Zeptonewton force sensing with nanospheres in an optical lattice," *Physical Review A*, vol. 93, no. 5, p. 053801, 2016.

[95] F. Ricci, M. T. Cuairan, G. P. Conangla, A. W. Schell, and R. Quidant, "Accurate mass measurement of a levitated nanomechanical resonator for precision force-sensing," *Nano letters*, vol. 19, no. 10, pp. 6711–6715, 2019.

[96] J. Ahn, Z. Xu, J. Bang, P. Ju, X. Gao, and T. Li, "Ultrasensitive torque detection with an optically levitated nanorotor," *Nature Nanotechnology*, vol. 15, no. 2, pp. 89–93, 2020.

[97] J. Piotrowski, D. Windey, J. Vijayan, C. Gonzalez-Ballestero, A. de los Ríos Sommer, N. Meyer, R. Quidant, O. Romero-Isart, R. Reimann, and L. Novotny, "Simultaneous ground-state cooling of two mechanical modes of a levitated nanoparticle," *Nature Physics*, vol. 19, pp. 1009–1013, 2023.

[98] J. Rieser, M. A. Ciampini, H. Rudolph, N. Kiesel, K. Hornberger, B. A. Stickler, M. Aspelmeyer, and U. Delić, "Tunable light-induced dipole-dipole interaction between optically levitated nanoparticles," *Science*, vol. 377, no. 6609, pp. 987–990, 2022.

[99] T. Penny, A. Pontin, and P. Barker, "Sympathetic cooling and squeezing of two colevitated nanoparticles," *Physical Review Research*, vol. 5, no. 1, p. 013070, 2023.

[100] I. Brandão, D. Tandeitnik, and T. Guerreiro, "Coherent scattering-mediated correlations between levitated nanospheres," *Quantum Science and Technology*, vol. 6, no. 4, p. 045013, 2021.

[101] J. Vijayan, J. Piotrowski, C. Gonzalez-Ballestero, K. Weber, O. Romero-Isart, and L. Novotny, "Cavity-mediated long-range interactions in levitated optomechanics," *Nature Physics*, vol. 20, pp. 859–864, 2024.

[102] A. Dechant, N. Kiesel, and E. Lutz, "All-optical nanomechanical heat engine," *Physical review letters*, vol. 114, no. 18, p. 183602, 2015.

[103] J. Millen and A. Xuereb, "Perspective on quantum thermodynamics," *New Journal of Physics*, vol. 18, no. 1, p. 011002, 2016.

[104] M. Debiossac, D. Grass, J. J. Alonso, E. Lutz, and N. Kiesel, "Thermodynamics of continuous non-markovian feedback control," *Nature communications*, vol. 11, no. 1, p. 1360, 2020.

[105] M. Debiossac, M. L. Rosinberg, E. Lutz, and N. Kiesel, "Non-markovian feedback control and acausality: an experimental study," *Physical Review Letters*, vol. 128, no. 20, p. 200601, 2022.

[106] R. Muffato, T. Georgescu, J. Homans, T. Guerreiro, Q. Wu, D. Chisholm, M. Carlesso, M. Paternostro, and H. Ulbricht, "Generation of classical non-gaussian distributions by squeezing a thermal state into non-linear

motion of levitated optomechanics," *arXiv preprint arXiv:2401.04066*, 2024.

[107] A. Arvanitaki and A. A. Geraci, "Detecting high-frequency gravitational waves with optically levitated sensors," *Physical review letters*, vol. 110, no. 7, p. 071105, 2013.

[108] G. Afek, F. Monteiro, J. Wang, B. Siegel, S. Ghosh, and D. C. Moore, "Limits on the abundance of millicharged particles bound to matter," *Physical Review D*, vol. 104, no. 1, p. 012004, 2021.

[109] F. Monteiro, G. Afek, D. Carney, G. Krnjaic, J. Wang, and D. C. Moore, "Search for composite dark matter with optically levitated sensors," *Physical Review Letters*, vol. 125, no. 18, p. 181102, 2020.

[110] D. C. Moore and A. A. Geraci, "Searching for new physics using optically levitated sensors," *Quantum Science and Technology*, vol. 6, no. 1, p. 014008, 2021.

[111] G. Afek, D. Carney, and D. C. Moore, "Coherent scattering of low mass dark matter from optically trapped sensors," *Physical review letters*, vol. 128, no. 10, p. 101301, 2022.

[112] G. P. Winstone, D. H. Grass, A. Wang, S. Klomp, A. Laeuger, C. Galla, C. Montoya, N. Aggarwal, J. Sprague, A. Poverman *et al.*, "High frequency gravitational wave detection with optically levitated nanoparticles: an update on lsd (levitated sensor detector)," in *Optical and Quantum Sensing and Precision Metrology II*, vol. 12016. SPIE, 2022, pp. 57–66.

[113] I. Pikovski, M. R. Vanner, M. Aspelmeyer, M. Kim, and Č. Brukner, "Probing planck-scale physics with quantum optics," *Nature Physics*, vol. 8, no. 5, pp. 393–397, 2012.

[114] T. Weiss, M. Roda-Llordes, E. Torrontegui, M. Aspelmeyer, and O. Romero-Isart, "Large quantum delocalization of a levitated nanoparticle using optimal control: Applications for force sensing and entangling via weak forces," *Physical Review Letters*, vol. 127, no. 2, p. 023601, 2021.

[115] P. T. Grochowski, H. Pichler, C. A. Regal, and O. Romero-Isart, "Quantum control of continuous systems via nonharmonic potential modulation," *arXiv preprint arXiv:2311.16819*, 2023.

[116] K. Aikawa and M. Kamba, "Revealing the velocity uncertainties of a levitated particle in the quantum ground state," *Physical Review Letters*, vol. 131, 2023.

[117] V. Jain, J. Gieseler, C. Moritz, C. Dellago, R. Quidant, and L. Novotny, "Direct measurement of photon recoil from a levitated nanoparticle," *Physical review letters*, vol. 116, no. 24, p. 243601, 2016.

[118] L. Hackermüller, K. Hornberger, B. Brezger, A. Zeilinger, and M. Arndt, "Decoherence of matter waves by thermal emission of radiation," *Nature*, vol. 427, no. 6976, pp. 711–714, 2004.

[119] J. Gieseler, B. Deutsch, R. Quidant, and L. Novotny, "Subkelvin parametric feedback cooling of a laser-trapped nanoparticle," *Physical review letters*, vol. 109, no. 10, p. 103603, 2012.

[120] M. Rosinberg, T. Munakata, and G. Tarjus, "Stochastic thermodynamics of langevin systems under time-delayed feedback control: Second-law-like inequalities," *Physical Review E*, vol. 91, no. 4, p. 042114, 2015.

[121] V. Belavkin, "Quantum filtering of markov signals with white quantum noise," in *Quantum communications and measurement*. Springer, 1995, pp. 381–391.

[122] V. P. Belavkin, "Measurement, filtering and control in quantum open dynamical systems," *Reports on Mathematical Physics*, vol. 43, no. 3, pp. A405–A425, 1999.

[123] H. M. Wiseman and G. J. Milburn, *Quantum measurement and control*. Cambridge University Press, 2009.

[124] B. Melo, M. T. Cuairan, G. F. Tomassi, N. Meyer, and R. Quidant, "Vacuum levitation and motion control on chip," *Nature Nanotechnology*, 2024.

[125] E. Bonvin, L. Devaud, M. Rossi, A. Militaru, L. Dania, D. S. Bykov, M. Teller, T. E. Northup, L. Novotny, and M. Frimmer, "Hybrid paul-optical trap with large optical access for levitated optomechanics," *arXiv preprint arXiv:2312.10131*, 2023.

[126] G. F. Franklin, J. D. Powell, and A. Emami-Naeini, *Feedback control of dynamic systems*. Pearson London, 2015, vol. 33.

[127] D. E. Kirk, *Optimal control theory: an introduction*. Courier Corporation, 2004.

[128] R. E. Kalman *et al.*, "A new approach to linear filtering and prediction problems," *Journal of basic Engineering*, vol. 82, no. 1, pp. 35–45, 1960.

[129] K. J. Åström, *Introduction to stochastic control theory*. Courier Corporation, 2012.

[130] M. Frimmer, K. Luszcz, S. Ferreiro, V. Jain, E. Hebestreit, and L. Novotny, "Controlling the net charge on a nanoparticle optically levitated in vacuum," *Physical Review A*, vol. 95, no. 6, p. 061801, 2017.

[131] J. Ahn, Z. Xu, J. Bang, Y.-H. Deng, T. M. Hoang, Q. Han, R.-M. Ma, and T. Li, "Optically levitated nanodumbbell torsion balance and ghz nanomechanical rotor," *Physical Review Letters*, vol. 121, p. 033603, 2018.

[132] J. A. Zielińska, F. van der Laan, A. Norrman, M. Rimlinger, R. Reimann, L. Novotny, and M. Frimmer, "Controlling optomechanical libration with the degree of polarization," *Physical Review Letters*, vol. 130, p. 203603, 2023.

[133] J. A. Zielińska, F. van der Laan, A. Norrman, R. Reimann, M. Frimmer, and L. Novotny, "Spinning a levitated mechanical oscillator far into the deep-strong coupling regime," *arXiv preprint arXiv:2310.03706*, 2023.

[134] Y. Xu, Y.-H. Liu, C. Liu, and J.-Q. Liao, "Simultaneous ground-state cooling of two levitated nanoparticles by coherent scattering," *Physical Review A*, vol. 109, p. 053521, 2024.

[135] I. Califrer and O. Kremer, 2024. [Online]. Available: https://github.com/QuantumAdventures/single-photons

[136] W. P. Bowen and G. J. Milburn, *Quantum Optomechanics*. CRC Press, 2016.

[137] C. W. Gardiner and M. J. Collett, "Input and output in damped quantum systems: quantum stochastic differential equations and the master equation," *Physical Review A*, vol. 31, no. 6, pp. 3761–3774, 1985.

[138] A. d. l. R. Sommer, N. Meyer, and R. Quidant, "Strong optomechanical coupling at room temperature by coherent scattering," *Nature Communications*, vol. 12, no. 276, 2021.

[139] B. E. Saleh and M. C. Teich, *Fundamentals of photonics*. John Wiley & Sons, 2019.

[140] K. Dare, J. J. Hansen, I. Coroli, A. Johnson, M. Aspelmeyer, and U. Delic, "Linear ultrastrong optomechanical interaction," *arXiv preprint arXiv:2305.16226*, 2023.

[141] K. Kustura, C. Gonzales-Ballestero, A. d. l. R. Sommer, N. Meyer, R. Quidant, and O. Romero-Isart, "Mechanical squeezing via unstable dynamics in a microcavity," *Physical Review Letters*, vol. 128, p. 143601, 2022.

[142] C. Weedbrook, S. Pirandola, R. García-Patrón, N. J. Cerf, T. C. Ralph, J. H. Shapiro, and S. Lloyd, "Gaussian quantum information," *Reviews of Modern Physics*, vol. 84, no. 2, pp. 621–669, 2012.

[143] S. C. Edwards and V. P. Belavkin, "Optimal quantum filtering and quantum feedback control," *arXiv preprint arXiv:quant-ph/0506018*, 2005.

[144] E. Lavretsky and K. A. Wise, *Robust and adaptive control with aerospace applications*. Springer, 2013.

[145] S. Zhao and B. Huang, "Trial-and-error or avoiding a guess? initialization of the kalman filter," *Automatica*, vol. 121, p. 109184, 2020.

[146] R. Schaumann, H. Xiao, and V. V. Mac, *Design of analog filters*, 2nd ed. Oxford University Press, Inc., 2009.

[147] P. Wilson, *Design recipes for FPGAs*. Newnes, 2015.

[148] G. F. Franklin, J. D. Powell, M. L. Workman *et al.*, *Digital control of dynamic systems*. Addison-Wesley Menlo Park, CA, 1998, vol. 3.

A
Perturbative nonlinear feedback forces for optical levitation experiments: Supplementary material

A.1
Electric field simulation

One of the experiment's central assumptions is that the electric force acting upon the trapped particle is proportional to the voltage applied to the electrodes and does not depend on its position. Moreover, due to symmetry around the optical axis, we expect the components of the electric force orthogonal to the optical axis to be negligible. To verify these assumptions, a simulation of the electric potential and electric field generated by the geometry of the optical setup was conducted using COMSOL Multiphysics software (version 5.4).

In Fig. A.1, the electrical potential between the electrodes is shown for a slice in the xz plane, where the internal contour of the optical setup is displayed for clarity. The left electrode, which contains the trapping lens, is set at 1 V relative to the right one, which holds the collection lens. The black dot denotes the average position of the trapped particle, 1.59 mm away from the flat base of the aspheric lens. Figures A.2(a) and A.2(b) show the electric field components in the vicinity of the particle. Considering an average amplitude of 100 nm for the COM motion, the simulation shows a percent change of roughly 0.01% for the z component of the electric field. Moreover, the x and y components are four to five orders of magnitude smaller than the z component, thus providing a firm foundation for our assumptions.

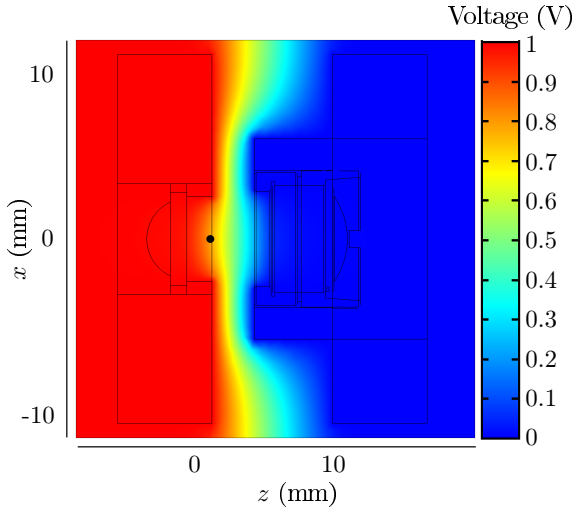

Figure A.1: Electric potential generated by the electrodes' geometry for a slice in the xz plane passing through the optical axis. The contour shows the internal structure of the optical setup with the black dot marking the average position of the trapped particle, about 1.59 mm away from the flat base of the trapping lens.

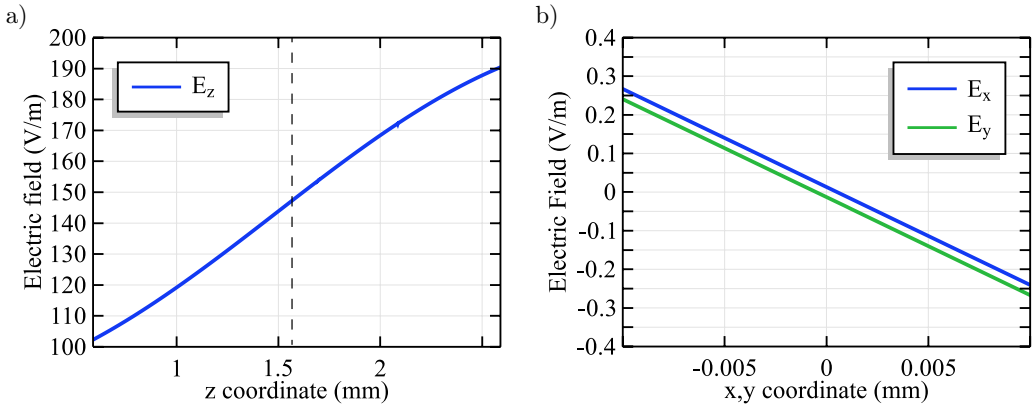

Figure A.2: (a)-(b) The z and x, y components of the electric field in the vicinity of the trapped particle. The dashed line denotes the average position of the particle.

A.2 Electronics

In order to apply the feedback signal, essential steps were undertaken regarding the implementation of an electronic setup aimed at preprocessing the detection signal. First, it was crucial to address a strong DC (direct current) component present in the signal obtained from the photodetector. To prevent saturation of the Red Pitaya RF (radio frequency) input used in the experiment, an analog band-pass filter was implemented for its capability to remove both DC and high-frequency components effectively. While it's common to opt for a

Butterworth filter based on the Sallen-Key topology [146], it is important to highlight that this choice introduces an undesirable phase effect.

As demonstrated by simulation results showed in Fig. A.3 (a), the addition of a Butterworth filter results in a shift of the PSD central frequency, which deviates from the theoretical prediction presented in [56]. To overcome this problem a passive RC filter is used along with a non-inverter amplifier. As evident from Fig. A.3 (b), the comparison of the Bode diagrams for both topologies illustrates that the passive filter will have minimal impact on the signal phase, while simultaneously maintaining a flat band over a wider frequency range.

The addition of a non-inverting amplifier after the band-pass filter enables the utilization of the full resolution of the ADC on the Red Pitaya board. Furthermore, a second amplifier is incorporated after the FPGA, facilitating the generation of voltage values approximately ten times higher than the board's limit. Upon characterization of both amplifiers, we found that the gains, A_1 and A_2, before and after the FPGA were measured as $11.00\,\mathrm{V/V}$ and $11.27\,\mathrm{V/V}$, respectively. These values will be necessary for the calibration of the overall feedback gain G_{fb}, detailed in appendix A.3.

In Fig. A.3 (c) we illustrate an example of input and output signals of the Red Pitaya. In order to implement the non-linear function, we employed fixed-point arithmetic—a method for representing fractional numbers within a specified range. This approach enables us to execute complex mathematical operations without suffering from information loss [147], as is often the case with binary representation. Furthermore, it offers straightforward means of extending the code to implement higher-order polynomial functions.

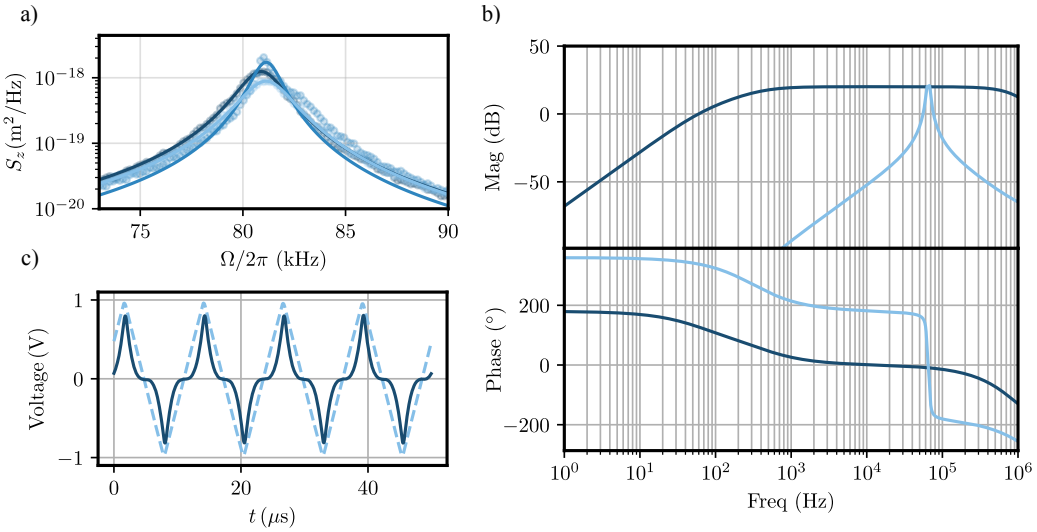

Figure A.3: Filter design. (a) PSD's obtained from simulations of a tweezed NP ($\Omega_z/2\pi = 81.5\,\mathrm{kHz}$ and $\gamma_m = 1.3 \times 10^4\,\mathrm{s}^{-1}$) under the influence of a cubic force. Three scenarios were considered: second-order Butterworth filter with 1 kHz bandwidth (—), 10 kHz bandwidth (—) and, lastly, with no filter (—). (b) Bode diagrams of a highly selective Butterworth filter (—) and of a passive RC filter (—), both circuits were simulated using LTspice XVII. (c) Results from the FPGA program. The dashed line represents the input, which is a triangular wave with a frequency of 81 kHz. The solid line corresponds to the output, which is proportional to the input raised to the third power.

A.3 Calibration of applied force

To validate the theoretical predictions outlined in [56], it was necessary to calibrate the overall feedback gain G_{fb}, defined as

$$G_{fb} = C_{NV} A_2 A_d A_1^3 C_{mV}^3, \tag{A-1}$$

where A_1 and A_2 represent the gains originating from the electronic amplifiers, A_d is the tunable digital gain defined within the FPGA, C_{mV} is the calibration factor which converts the measured voltage into corresponding displacement in meters and C_{NV} is the transduction coefficient that establishes the connection between applied voltage across the electrodes and the resulting force applied to the particle; see appendix A.2 for further details.

To calibrate the photodetector, 1000 traces of 0.1 seconds were collected. The PSD of the time traces is fitted by a Lorentizan distribution,

$$S_V(\omega) = \frac{D}{\gamma_m^2\omega^2 + (\omega^2 - \omega_0^2)^2}, \tag{A-2}$$

where $D = 2\gamma_m k_B T_{\text{eff}} C_{mV}^2/m$; this take in consideration that $S_V(\omega) = C_{mV}^2 S_z(\omega)$ [66]. This procedure led to a calibration factor of $C_{mV} = (1.504 \pm 0.073) \times 10^4\,\text{V/m}$. After calibration of the detector, we proceed to determine the transduction coefficient, denoted as C_{NV}. To obtain C_{NV}, we subjected the particle to a series of sinusoidal signals with varying amplitudes and measured the particle's response in the position PSD [95]. For a particle subjected to Eq. 2-3, the total PSD $S_z^T(\omega)$ in the presence of an electric drive $F_{el}(t) = F_0\cos(\omega_{dr}t)$ can be expressed as [95],

$$S_z^T(\omega) = S_z(\omega) + S_z^{el}(\omega) = \frac{2\gamma_m k_B T_{\text{eff}}}{m[(\omega^2 - \omega_0^2)^2 + \gamma_m^2\omega^2]} + \frac{F_0^2\tau_{el}\,\text{sinc}^2[(\omega - \omega_{dr})\tau_{el}]}{m^2[(\omega^2 - \omega_0^2)^2 + \gamma_m^2\omega^2]}, \tag{A-3}$$

with $2\tau_{el}$ being the duration of the measure. In Figure A.4a), we display one of the PSDs used for the electrode calibration. The resulting calibration curve is presented in Figure A.4b), which yields a transduction coefficient $C_{NV} = (3.06 \pm 0.13) \times 10^{-15}\,\text{N/m}$. All measurements described in the main text were performed with the same NP.

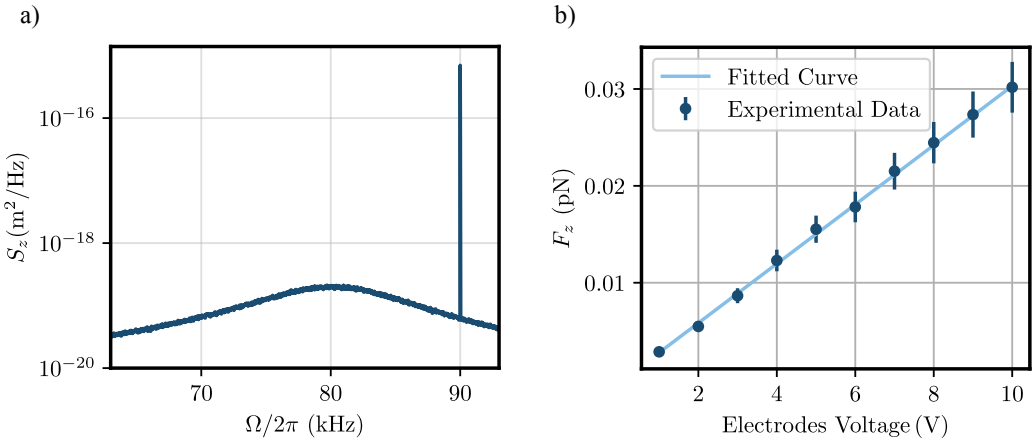

Figure A.4: Electrode calibration: (a) PSD obtained from a trapped NP at 10 mbar and $T_{\text{eff}} = 293\,\text{K}$ under the action of a sinusoidal drive (voltage amplitude $V_0 = 10\,\text{V}$ and frequency $\omega_{dr}/2\pi = 90\,\text{kHz}$). b) Calibration curve for electrodes used to map the applied voltage to the resulting force applied on the NP.

B
All electrical cooling of an optically levitated nanoparticle: Supplementary material

B.1
Digital control theory

In the study and analysis of physical systems, time is conventionally treated as a continuous variable. However, when employing signal processing and control methods, a transition to a discrete representation becomes necessary. This is specially crucial when implementing systems on microprocessors or FPGAs, where a set of instructions is executed based on a sampling frequency f_s [148]. The discrete-time formulation of a state-space model can be obtained through the integral approximation, which is based on the assumption that $\mathbf{x}$ and $\mathbf{u}$ remain constant during a sampling period $\delta t = 1/f_s$. The system evolution is then considered to unfold at fixed time-steps $t_n = n\delta t$, leading to the following recursive equations

$$\mathbf{x}_{n+1} = \mathcal{A}_d \mathbf{x}_n + \mathbf{B}_d \mathbf{u}_n + \bar{\mathbf{w}}_n, \tag{B-1a}$$

$$\mathbf{y}_{n+1} = \mathcal{C}_d \mathbf{x}_{n+1} + \bar{\mathbf{m}}_{n+1}, \tag{B-1b}$$

where $\mathbf{A}_d$, $\mathbf{B}_d$ and $\mathbf{C}_d$ can be expressed in terms of their continuous analogues,

$$\mathcal{A}_d = \sum_{k=0}^{\infty} \frac{\delta t^k}{k!} \mathcal{A}^k, \tag{B-2a}$$

$$\mathbf{B}_d = (\mathcal{A}_d - \mathcal{I})\mathcal{A}^{-1}\mathbf{B}, \tag{B-2b}$$

$$\mathcal{C}_d = \mathcal{C}. \tag{B-2c}$$

Also, $\mathbf{x}_n = \mathbf{x}(nT_s)$ and $\mathbf{u}_n = \mathbf{u}(nT_s)$. The discrete disturbance and noise terms, $\bar{\mathbf{w}}_n$ and $\bar{\mathbf{m}}_n$, represent discrete-time white-noise processes adhering to conditions akin to those established in Eqs. (3-2) and (3-11) in the main text. Considering $\bar{\mathbf{w}}_n = \frac{1}{m}\begin{bmatrix}\mathbf{0}_{3\times1} & \bar{\mathbf{F}}_{\mathrm{th,n}}\end{bmatrix}^T$, with $\bar{\mathbf{F}}_{\mathrm{th,n}} = \begin{bmatrix}\bar{F}_{\mathrm{th,x,n}} & \bar{F}_{\mathrm{th,y,n}} & \bar{F}_{\mathrm{th,z,n}}\end{bmatrix}^T$ and $\bar{\mathbf{m}}_n = \begin{bmatrix}\bar{\zeta}_{x,n} & \bar{\zeta}_{y,n} & \bar{\zeta}_{z,n}\end{bmatrix}^T$, the conditions are

$$\langle \bar{F}_{\mathrm{th,i,k}} \rangle = 0, \tag{B-3a}$$

$$\langle \bar{F}_{\mathrm{th,i,k}} F_{\mathrm{th,j,k'}} \rangle = 2m\gamma_m k_B T T_s \delta_{ij}\delta_{kk'}, \tag{B-3b}$$

and

$$\langle \bar{\zeta}_{i,k}(t) \rangle = 0, \tag{B-4a}$$

$$\langle \bar{\zeta}_{i,k} \bar{\zeta}_{j,k'} \rangle = \frac{\sigma_i}{T_s}\delta_{ij}\delta_{kk'}. \tag{B-4b}$$

Similar to its continuous version, the LQR for discrete-time systems returns an optimal control law, expressed as a linear combination on the states $\mathbf{x}_n$,

$$\mathbf{u}_n = -\mathbf{K}_d \mathbf{x}_n, \tag{B-5}$$

however, the expression for the controller's gain changes to

$$\mathbf{K}_d = (\mathbf{R}_d + \mathbf{B}_d^T \mathbf{S}_d \mathbf{B}_d)^{-1} \mathbf{B}_d^T \mathbf{S}_d \mathcal{A}_d, \tag{B-6}$$

where $\mathbf{S}_d$ is the solution of the discrete algebraic Ricatti equation

$$\begin{aligned} \mathbf{S}_d = {} & \mathcal{A}_d^T \mathbf{S}_d \mathcal{A}_d + \mathcal{Q}_d \\ & - \mathcal{A}_d^T \mathbf{S}_d \mathbf{B}_d (\mathbf{R}_d + \mathbf{B}_d^T \mathbf{S}_d \mathbf{B}_d)^{-1} \mathbf{B}_d^T \mathbf{S}_d \mathcal{A}_d, \end{aligned} \tag{B-7}$$

and $\mathcal{Q}_d$ and $\mathbf{R}_d$ are the matrices defining the cost function J_d for the digital control law, which reads

$$J_d = \frac{1}{2} \sum_{n=0}^{\infty} [\mathbf{x}_n^T \mathcal{Q}_d \mathbf{x}_n + \mathbf{u}_n^T \mathbf{R}_d \mathbf{u}_n]. \tag{B-8}$$

B.2 Electronic setup

The control law defined in Eq. (B-5) was implemented using two Red Pitayas, each equipped with a Xilinx Zynq 7010 FPGA and a 2 channel 14-bits ADC, allowing for a maximum sampling frequency of 125 MHz for two distinct inputs, x_a and x_b. The feedback loop incorporated a decimation block, increasing the sampling time T_s from 8.00 ns to 64.00 ns, enabling synchronous execution of more complex tasks.

In Fig. B.1 a simplified block diagram of the main components implemented within each FPGA is shown. The controller block is responsible for computing the output signal $u_{a,n}$ and $u_{b,n}$, being equivalent to the following expression

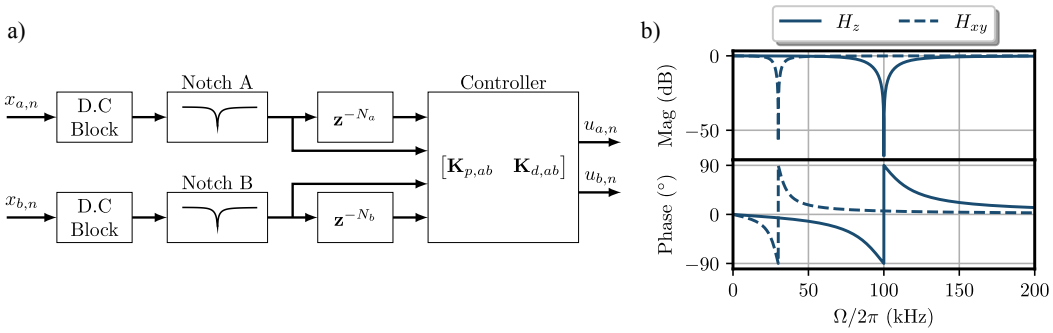

Figure B.1: Digital electronic implementation. a) Block diagram illustrating the FPGA implementation for stable control of the particle CoM motion. The digital filters are responsible for signal conditioning. A Block Random Access Memory allows the implementation of delay blocks, delaying the signal in multiples (N_a, N_b) of the sampling time. The delayed and non-delayed filtered signals are then transmitted to the controllers to compute the output signals. b) Bode plots for each notch filter H_z and H_{xy}, depicting their magnitude and phase behavior for the frequency range of interest.

$$\begin{bmatrix} u_{a,n} \\ u_{b,n} \end{bmatrix} = \begin{bmatrix} k^d_{p,aa} & k^d_{p,ab} & k^d_{d,aa} & k^d_{d,ab} \\ k^d_{p,ba} & k^d_{p,bb} & k^d_{d,ba} & k^d_{d,bb} \end{bmatrix} \begin{bmatrix} \tilde{x}_{a,n} \\ \tilde{x}_{b,n} \\ \tilde{x}_{a,n-N_a} \\ \tilde{x}_{b,n-N_b} \end{bmatrix}. \tag{B-9}$$

The signals $\tilde{x}_{a,n}$, $\tilde{x}_{b,n}$ result from passing the inputs through a D.C block and a notch filter, both implemented by using digital biquadratic filters. The constant $k^d_{p,ij}$ and $k^d_{d,ij}$ refer to the digital proportional and derivative gains. The signals $\tilde{x}_{a,n-N_a}$, $\tilde{x}_{b,n-N_b}$ are the delayed positions, serving as estimates of the particle's velocity. Here, N_a and N_b are integers representing the applied delay in units of T_s.

The notch filter transfer function is shown in Fig. B.1.b). For the FPGA processing the x and y signals, the transfer function used was H_{xy} to remove harmonic components near Ω_z. In the other FPGA, a filter H_z was applied to remove any components sufficiently close to Ω_x and to Ω_y. The filter's impact on the phase of each signal is approximately constant near each resonance frequency, being included in the overall intrinsic delay of the electronic setup, already described in Section 3.1.4. The computed control signals were sent to non-inverting analog amplifiers, providing a constant gain $A = 5.00\,\mathrm{V/V}$ with minimal phase impact for signals with harmonic components from D.C up to 150.00 kHz.

B.3 Model parameters

Implementation of LQR relies on the accurate extraction of the **A** and **B** matrices, essential for the correct computation of $\mathbf{A}_d$ and $\mathbf{B}_d$. This appendix clarifies how the parameters that allow the reconstruction of these matrices were extracted for the experiment.

B.3.1 Detector calibration

Assuming the trapped NP reaches thermal equilibrium with the residual gas in the vacuum chamber, its initial effective temperature along the three axes is approximately 293 K. Calibration of the detection system involves establishing the linear relationship between the PSD of the detector output for motion along the i-axis, denoted as $S_{V_iV_i}(\Omega)$, and the displacement PSD for the same axis, denoted as $S_{ii}(\Omega)$ [66],

$$S_{V_iV_i}(\Omega) = (C^i_{Vm})^2 S_{ii}(\Omega), \tag{B-10}$$

with C^i_{Vm} representing the calibration factor and $S_{V_iV_i}$ being defined by the Lorentzian function,

$$S_{V_iV_i}(\Omega) = (C^i_{Vm})^2 \frac{2\gamma_m k_B T}{m[(\Omega^2 - \Omega_i^2)^2 + \gamma_m^2 \Omega_i^2]} \tag{B-11}$$

Calibration was done by collecting 10,000 traces, each with a duration of 50 ms. The average PSDs were then fitted to Equation (B-11), enabling the extraction of C^i_{Vm}, Ω_i and γ_m. The coefficients were found to be

$$C^x_{Vm} = (6.87 \pm 0.72) \times 10^5 \,\mathrm{V/m}$$

$$C^y_{Vm} = (7.08 \pm 0.75) \times 10^5 \,\mathrm{V/m}$$

$$C^z_{Vm} = (1.07 \pm 0.11) \times 10^6 \,\mathrm{V/m}.$$

Given these calibration factors, and considering a completely decoupled detection scheme, the $\mathcal{C}$ matrix can be expressed as

$$\mathcal{C} = \begin{bmatrix} C^x_{Vm} & 0 & 0 & 0 & 0 & 0 \\ 0 & C^y_{Vm} & 0 & 0 & 0 & 0 \\ 0 & 0 & C^z_{Vm} & 0 & 0 & 0 \end{bmatrix} \tag{B-12}$$

B.3.2 Electrodes calibration

To compute the controller's gain matrix $\mathbf{K}_d$ described in Appendix B.1, it is necessary to measure the transduction coefficient C_{NV}^{ij} that provides the linear relation between the applied voltage across the electrodes j and the resulting force along the i-axis. From these, it is possible to reconstruct the terms of the $\mathbf{B}$ matrix, which due to the geometry of the actuators couples the x and y-axes.

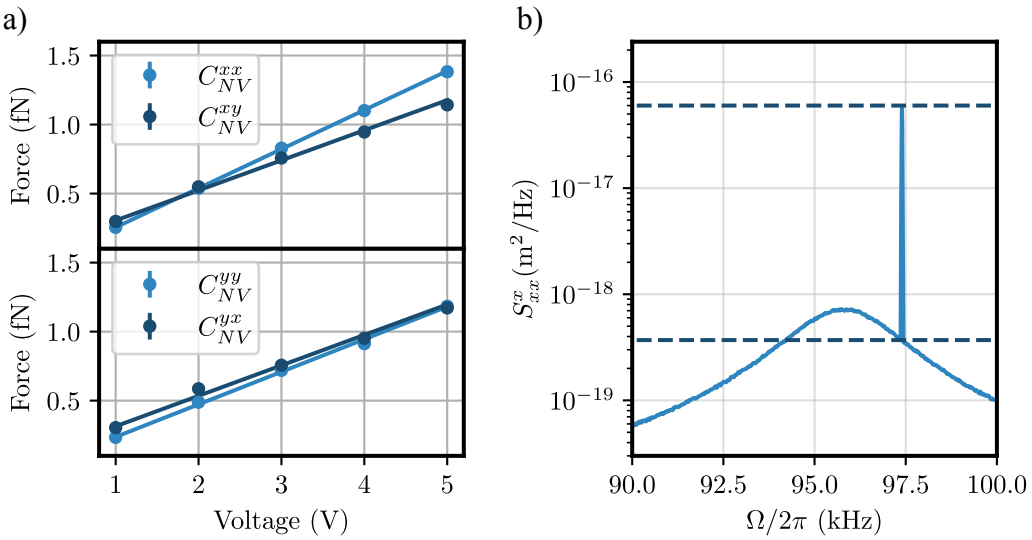

Figure B.2: Electrode calibration. a) Calibration curves are presented for each coefficient of the xy plane. Each point corresponds to the analysis of 7000 traces with an individual duration of 50 ms. The particle was driven with a sinusoidal signal at $\Omega_{dr}/2\pi = 97.50$ kHz. b) PSD of the particle's CoM motion under the action of a sinusoidal force. The dashed line delineates the peak region from which the amplitude of the force F_0 can be extracted.

Force calibration of the electrodes can be carried out by measuring the particle's response to sinusoidal voltage drives applied to an individual pair of electrodes at known frequencies near each resonance [95]. The driving voltage in the electrode j introduces a sinusoidal force $F_i^j \cos(\Omega_{dr} t)$ which can be observed within the PSD of the driven CoM motion of the i direction S_{ii}^j,

$$S_{ii}^j = S_{ii}(\Omega) + S_{ii}^{j,el}(\Omega), \tag{B-13}$$

where $S_{ii}(\Omega)$ follows Eq. (3-13) and $S_{ii}^{j,el}(\Omega)$ is

$$S_{ii}^{j,el}(\Omega) = \frac{F_i^{j2} \tau_{el}\, \mathrm{sinc}^2[(\Omega - \Omega_{dr})\tau_{el}]}{m^2[(\Omega^2 - \Omega_i^2)^2 + \gamma_m^2 \Omega^2]}, \tag{B-14}$$

with τ_{el} being the duration of the measure.

In Figure B.2a), the calibration curves for each coefficient is shown, yielding

$$C_{NV}^{xx} = (2.83 \pm 0.14) \times 10^{-16}\,\mathrm{N/V}$$

$$C_{NV}^{xy} = (2.18 \pm 0.13) \times 10^{-16}\,\mathrm{N/V}$$

$$C_{NV}^{yx} = (2.21 \pm 0.13) \times 10^{-16}\,\mathrm{N/V}$$

$$C_{NV}^{yy} = (2.36 \pm 0.12) \times 10^{-16}\,\mathrm{N/V}$$

An example of one of the PSDs used for calibration is presented in Fig. B.2b).

B.3.3 Gain matrix

After ensuring proper calibration of the detectors and actuators, computation of the LQR gains becomes feasible. Analysis of the PSDs of the x, y and z confirms the trapped NP's oscillation frequencies $\Omega_x/2\pi = 96.24\,\mathrm{kHz}$, $\Omega_y/2\pi = 101.49\,\mathrm{kHz}$ and $\Omega_z/2\pi = 31.52\,\mathrm{kHz}$. Given the average diameter of the NP as provided by the manufacturer, the its mass is calculated to be $m \approx 3.37\,\mathrm{fg}$. The weighting and cost-effort matrices used were

$$\mathbf{R}_d = m \begin{bmatrix} \mathrm{diag}(\mathbf{\Omega}^2) & \mathbf{0}_{3\times3} \\ \mathbf{0}_{3\times3} & I_3 \end{bmatrix}, \tag{B-15}$$

and

$$\mathcal{Q}_d = \frac{100}{m} \begin{bmatrix} \Omega_x^{-2} & 0 & 0 \\ 0 & \Omega_y^{-2} & 0 \\ 0 & 0 & \Omega_z^{-2} \end{bmatrix}. \tag{B-16}$$

These matrices were selected to ensure that the cost function J_d possesses appropriate energy units, considering the states measured in S.I units and $\mathbf{u}$ accounting for feedback forces. Such dimensional considerations are crucial for converting the controller's gain from the LQR theory to the digital gains configured in the FPGA. The $\mathbf{B}$ matrix is expressed as

$$\mathbf{B} = \begin{bmatrix} \mathbf{0}_{3\times3} \\ \mathbf{B}_{xyz} \end{bmatrix}, \text{ where } \mathbf{B}_{xyz} = \begin{bmatrix} \mathbf{B}_{xy} & 0 \\ \mathbf{0}_{1\times2} & b_z \end{bmatrix}. \tag{B-17}$$

The submatrix $\mathbf{B}_{xy}$, expressed in kg^{-1}, is determined by m and the proportion of the electrodes coefficients C_{NV}^{ij},

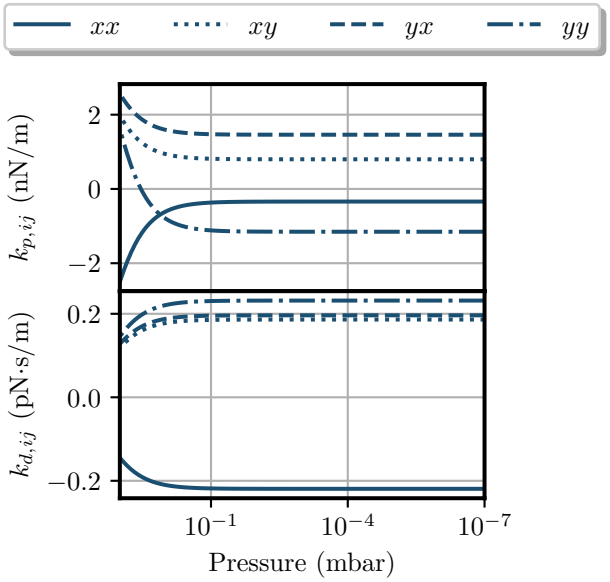

Figure B.3: Optimal gains dependence with pressure. The constant behavior for values bellow 1 mbar allows one to employ the same matrix $\mathbf{K}_d$ for the underdamped and undamped regimes.

$$\mathbf{B}_{xy} = \frac{1}{m}\begin{bmatrix} -1 & C_{NV}^{xy}/C_{NV}^{xx} \\ C_{NV}^{yx}/C_{NV}^{xx} & C_{NV}^{yy}/C_{NV}^{xx} \end{bmatrix}. \tag{B-18}$$

Without loss of generality, its terms were normalized by the biggest transduction coefficient, C_{NV}^{xx}. The negative sign accounts for the orientation of the electrodes axes, x' and y', as illustrated in Fig. 3.1.

The final parameter required to fully describe the dynamics given by Eq. (3-4), is γ_m. To assess the impact of varying it, we substitute the values for the resonance frequencies, $\mathbf{B}$, T_s, $\mathcal{Q}_d$, and $\mathbf{R}_d$ and compute $\mathbf{K}_d$ for different drag coefficients. The results of this evaluation are depicted in Fig. B.3. Notably, for pressures below 1 mbar, the influence of γ_m on the controller's gains is negligible. Therefore, under the premise that pressure solely affects the drag coefficient, $\mathbf{K}_d$ can be computed only once, even as pressure reduces.

After completing the system characterization, with γ_m considered as zero, $\mathbf{K}_d$ can be properly computed. The next step involves converting the theoretical gains into digital values configured within the FPGA. The following expressions govern this conversion

$$k_{p,ij}^d = \frac{k_{p,ij}}{AC_{NV}^{xx}C_{Vm}^j}, \tag{B-19a}$$

$$k_{d,ij}^d = -\frac{\Omega_j k_{d,ij}}{AC_{NV}^{xx}C_{Vm}^j}. \tag{B-19b}$$

Here, Ω_j emerges from estimating the velocity as proportional to the delayed position, leading, for example, to $\dot{x} = -\Omega_x x(t - \tau_x)$, for a delay τ_x. The factor C_{NV}^{xx} arises from the $\mathbf{B}_{xy}$ matrix normalization, while C_{Vm}^{j} is used to convert displacement in the j-axis to output voltages from its detector. In Table B.1, both theoretical and digital gains are presented.

Gain	LQR (Eq. B-5)	Digital Gains (Eq. B-19)
$k_{p,xx}$	$-3.40 \times 10^{-10}\,\mathrm{N/m}$	-0.35
$k_{p,xy}$	$7.99 \times 10^{-10}\,\mathrm{N/m}$	0.80
$k_{p,yx}$	$1.46 \times 10^{-9}\ \mathrm{N/m}$	1.50
$k_{p,yy}$	$-1.15 \times 10^{-9}\ \mathrm{N/m}$	-1.15
$k_{d,xx}$	$-2.19 \times 10^{-13}\,\mathrm{N \cdot s/m}$	136.45
$k_{d,xy}$	$1.86 \times 10^{-13}\,\mathrm{N \cdot s/m}$	-119.14
$k_{d,yx}$	$1.96 \times 10^{-13}\,\mathrm{N \cdot s/m}$	-122.22
$k_{d,yy}$	$2.32 \times 10^{-13}\,\mathrm{N \cdot s/m}$	-148.23

Table B.1: Controller's gains. Values returned by optimal control theory and implemented values within the FPGA are shown according to the system characterization and Eq. (B-19). The digital gains had to pass through a conversion to a fixed-point representation during the VHDL implementation, allowing arithmetical operations with minimal loss of numerical resolution [147].

C
Thermal polarization drifts

We have carried out a protocol for monitoring polarization drifts in our setup, which consisted in measuring the output power from a PBS after the vacuum chamber over extended periods. These measurements are illustrated in Fig. C.1, and they indicated that room temperature fluctuations may generate polarization drifts. Power variations with an amplitude of a few percent have been observed over a time scale of hours and seem to be caused by the air conditioning cycles in our lab.

These drifts have inspired us to build an insulating case for the fiber systems in our setup, given that backward detection is strongly reliant upon phase stability of interference happening inside a fiber system. This insulating box is depicted in Fig. C.2, and we have noticed that stabilization of the interferometer for backwards z-detection was significantly facilitated after introducing this structure.

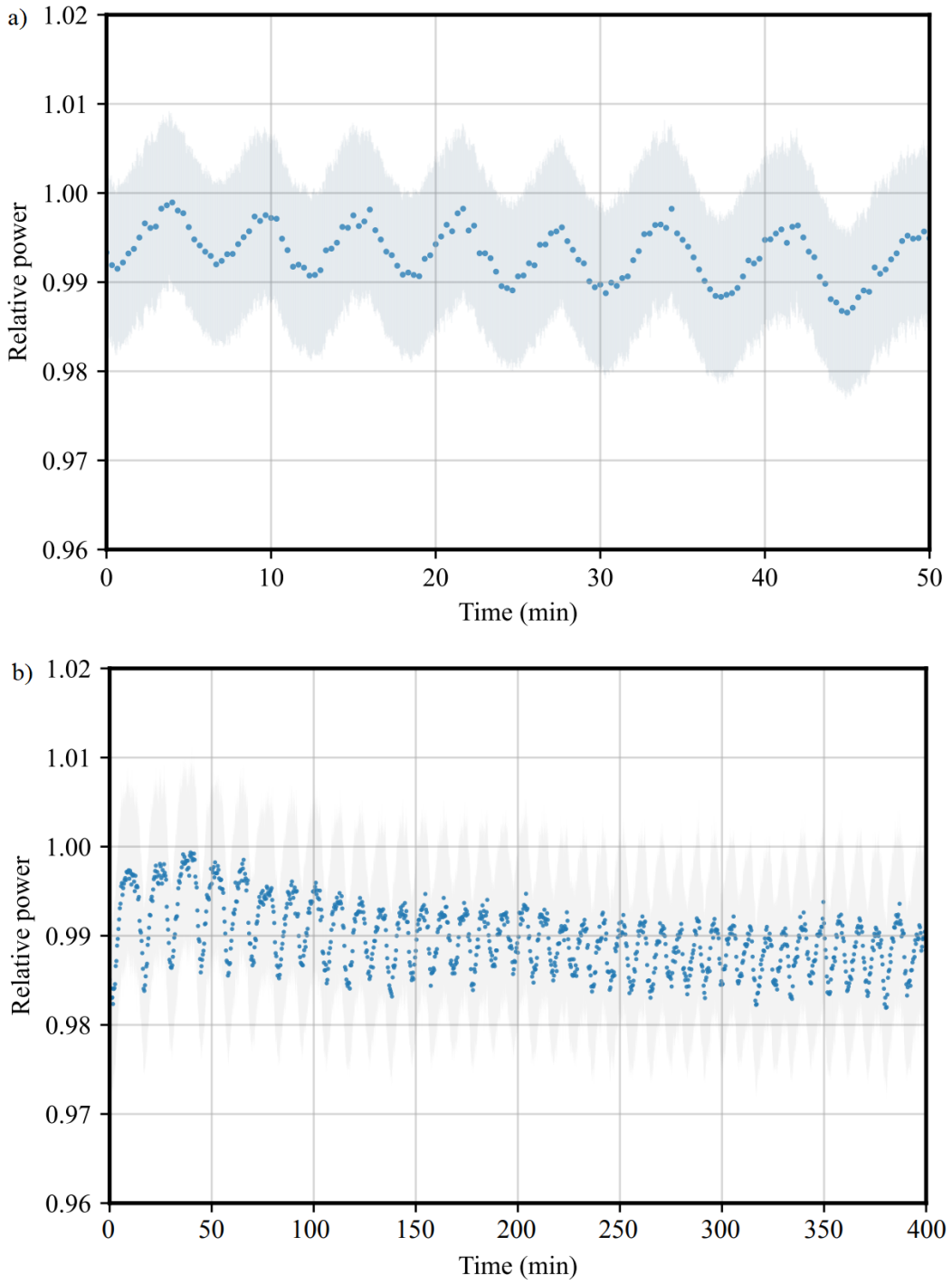

Figure C.1: Thermal polarization drifts. Panel a) shows a short measurement over the course of an hour, and cycles of about six minutes associated with the air conditioning system have been observed. Panel b) shows a longer measurement over many hours which was taken during the night, when room temperature is the most stable.

Figure C.2: Experimental insulating case. We have assembled two boxes for thermal and mechanical environment insulation. The external box, shown at the top, is made of polystyrene, while the internal box, shown at the bottom and made of rock wool, encases fiber optics exclusively.